UNIVERSITÀ DEGLI STUDI DI PADOVA

Dipartimento di Fisica e Astronomia “Galileo Galilei”

Master Degree in Physics

Final Dissertation

Nuclear Physics from Neutron Star-Black Hole mergers

Thesis supervisor:	***Candidate:***
Dr. Roberto Turolla	Lorenzo Morace

Thesis co-supervisor:

Dr. Alessandro Drago

Academic year: 2020/2021

Summary

INTRODUCTION

This thesis deals with the merging of compact objects (Neutron Stars and Black Holes) in a binary system from different perspectives. Neutron Stars, the endpoint of the evolution of stars with mass 10 $M_{sun} < M < 25$ M_{sun}, are the densest objects known in the present universe. With a mass of about 1.5 M_{sun} confined in a sphere of ~10 km radius, they offer unprecedented opportunities for the study of matter under conditions of extreme density and pressure, and can provide invaluable insights in the strong-field limit of General Relativity, Quantum Electrodynamics and Chromodynamics. Neutron stars being ideal laboratories notwithstanding, even more interesting are the interaction and the merging of this kind of objects when they are bound in a binary system. In fact, Binary Neutron Star (BNS) and Black Hole-Neutron Star (BHNS) mergers are a fertile ground for improving our knowledge about gravitational waves. In 2016 the first detection of gravitational waves, produced by the merging of a binary BH system, opened new horizons in this research field. Soon, the GW170817 event revealed the merging of a BNS, showing that the study of the GW signal allows to exclude some kinds of Equation of State for Neutron Stars, by considering the tidal deformability of the stars during the inspiral. GW170817 was unique among the GW events recorded up to now because of an electromagnetic counterpart was observed, a kilonova. The combined analysis of the gravitational wave and the electromagnetic signals let us investigate in a better way what we obtain as result of the merger, and what kind of transformations could affect the material emitted when two binary Neutron Star or a Neutron Star and a Black Hole interact. In particular, it has allowed to understand better how and under which conditions the formation of nuclei heavier than iron occurs. Besides, the study of the merging of Binary Compact Objects supports the possibility that a Quark Star, a compact remnant made of free quarks, may be indeed present. Behind these discoveries, there are however a number of unsolved issues. For example, we do not know the origin of the Gamma Ray Burst signal launched after the merging, although it is likely that the jet results from the formation of a black hole after the merging.

This thesis is organized as follows. In the first chapter, we outline the properties of gravitational waves, how they are produced and detected, underlining the future of GWs detection, and discuss neutron star-black hole mergers in the framework of GWs. In the second chapter we introduce Quark and Hybrid stars and compare them with neutron stars. In the third chapter, we study binary neutron star systems and the electromagnetic signal expected from the merging, with particular focus on the GW170817 event. In the fourth and last chapter, black hole-neutron star mergers are considered, again in connection with the ensuing electromagnetic signals.

CHAPTER 1

GRAVITATIONAL WAVES, THEIR ROLE IN DISCRIMINATING AMONG BINARY SYSTEMS AND THEIR LINK TO THE DEFORMABILITY OF NEUTRON STARS

In order to face the topic of merger between compact objects, such as neutron stars and black holes, some knowledge about gravitational waves is required. Thus, we can deal with the derivation of the Gravitational Waves. [1]

1.1 What are gravitational waves?

Gravitational waves can be thought as ripples in space-time caused by the motion with great acceleration of massive objects inside it. They were theorized by Einstein in 1916 and detected for the first time in 2016.In our context they are generated by the accelerated spiral motion of two neutron stars or by a neutron star and a black hole.

In order to explain those, we must write down the Einstein's equation, that is:

(1.1.1) $R_{\mu\nu} - \frac{1}{2} g_{\mu\nu} R = -kT_{\mu\nu}$.

where $R_{\mu\nu}$ is the Ricci tensor, R is the Ricci Scalar, $T_{\mu\nu}$ is the Energy-Momentum tensor, k is a constant and $g_{\mu\nu}$ is the metric tensor. Then, we have to consider the metric tensor $g_{\mu\nu}$ as expressed as the sum of the Minkowski tensor $\eta_{\mu\nu} = (+1,-1,-1,-1)$ and a perturbation element $h_{\mu\nu}$ with $|h_{\mu\nu}| << 1$, $g_{\mu\nu} = \eta_{\mu\nu} + h_{\mu\nu}$. At this point we must write down the Christoffel symbol

(1.1.2) $\Gamma^{\sigma}_{\mu\nu} = \frac{1}{2} g^{\rho\sigma} (\partial_\nu g_{\rho\mu} + \partial_\mu g_{\rho\nu} - \partial_\rho g_{\mu\nu})$

This symbol can be approximated, considering our expression of $g_{\mu\nu}$ as

(1.1.3) $\Gamma^{\sigma}_{\mu\nu} \approx \frac{1}{2} \eta^{\rho\sigma} (\partial_\nu h_{\rho\mu} + \partial_\mu h_{\rho\nu} - \partial_\rho h_{\mu\nu}) = \frac{1}{2} (\partial_\nu h^{\sigma}_{\mu} + \partial_\mu h^{\sigma}_{\nu} - \partial^{\sigma} h_{\mu\nu})$

Using the Christoffel symbol, we can write down the Riemann tensor:

(1.1.4) $R^{\sigma}_{\mu\nu\rho} = \partial_\nu \Gamma^{\sigma}_{\mu\rho} - \partial_\rho \Gamma^{\sigma}_{\mu\nu} + \Gamma^{\tau}_{\mu\rho}\Gamma^{\sigma}_{\tau\nu} - \Gamma^{\tau}_{\mu\nu}\Gamma^{\sigma}_{\tau\rho}$

Now, since we consider just perturbation of the first order, we can neglect the last two terms on the right-hand side. Thus, we get:

(1.1.5) $R^{\sigma}_{\mu\nu\rho} = \frac{1}{2}(\partial_\nu \partial_\mu h^{\sigma}_{\rho} + \partial_\rho \partial^\sigma h_{\mu\nu} - \partial_\nu \partial^\sigma h_{\mu\rho} - \partial_\rho \partial_\mu h^{\sigma}_{\nu})$

By contracting the first and the last indices of this expression, we get the Ricci tensor, which is:

(1.1.6) $R_{\mu\nu} = \frac{1}{2}(\partial_\nu \partial_\mu h + \Box h_{\mu\nu} - \partial_\nu \partial_\rho h^{\rho}_{\mu} - \partial_\rho \partial_\mu h^{\rho}_{\nu})$

where $\Box = \partial_\sigma \partial^\sigma$ is the d'Alembertian operator. After that, we can get the Ricci scalar by contracting the Ricci Tensor:

(1.1.7) $R = R^{\mu}{}_{\mu} = \eta^{\mu\nu} R_{\mu\nu} = \Box h - \partial_\rho \partial_\mu h^{\rho\mu}$

Now we can rewrite the Einstein's equation by substituting the expression of Ricci tensor and Ricci scalar. In this way, we obtain this equation:

(1.1.8) $\partial_\nu \partial_\mu h + \Box h_{\mu\nu} - \partial_\nu \partial_\rho h^{\rho}_{\mu} - \partial_\rho \partial_\mu h^{\rho}_{\nu} - \eta_{\mu\nu} (\Box h - \partial_\rho \partial_\sigma h^{\rho\sigma}) = -2k\, T_{\mu\nu}.$

This equation can be simplified by defining the "trace reverse" of $h_{\mu\nu}$, which is given by:

(1.1.9) $\widetilde{h_{\mu\nu}} = h_{\mu\nu} - \frac{1}{2} \eta_{\mu\nu} h$

By contracting the indices, we find $\tilde{h} = -h$. Using the trace reverse, the Einstein's equation becomes:

(1.1.10) $\Box \widetilde{h_{\mu\nu}} + \eta_{\mu\nu} \partial_\rho \partial_\sigma \widetilde{h^{\rho\sigma}} - \partial_\nu \partial_\rho \widetilde{h^{\rho}_{\mu}} - \partial_\mu \partial_\rho \widetilde{h^{\rho}_{\nu}} = -2kT_{\mu\nu}.$

This equation can be simplified by imposing the gauge transformation:

(1.1.11) $h_{\mu\nu}$ (new) = $h_{\mu\nu}$ (old) $- \partial_\mu \xi_\nu - \partial_\nu \xi_\mu$

where ξ is a vector such that we can write the infinitesimal transformation $x'^{\mu} = x^{\mu} + \xi^{\mu}(x)$. Now, by defining $\widetilde{h_{\mu\nu}}$ (new) = $h_{\mu\nu}$ (new) $- \frac{1}{2} \eta_{\mu\nu}\, h$(new), using the equation of relation between the new and the old form of the tensor $h_{\mu\nu}$, we obtain

(1.1.12) $\partial_\rho \widetilde{h^{\mu\rho}}$ (new) = $\partial_\rho \widetilde{h^{\mu\rho}}$ (old) $- \Box \xi^{\mu}$

Now, by using the Lorentz gauge condition $\partial_\rho h^{\mu\rho}$ (new)= 0, the Einstein's equation becomes

(1.1.13) $\Box \widetilde{h_{\mu\nu}} = -2kT_{\mu\nu}$

In the vacuum the Energy-Momentum tensor is zero in each component. Therefore, the equation becomes:

(1.1.14) $\Box \widetilde{h_{\mu\nu}} = 0$

whose solution is:

(1.1.15) $\widetilde{h_{\mu\nu}} = A^{\mu\nu} \exp(i\, k_\rho x^\rho)$

which is the equation of a plane wave, our gravitational wave, where $A^{\mu\nu}$ are constant components of a symmetric tensor and k_ρ are the constant real components of a vector. In this case the Lorentz condition is written as $A^{\mu\nu} k_\nu = 0$.

1.2 GWs detection and perspective for the future

If we consider a concrete example of a plane gravitational wave propagating in the z-direction, the k- vector can be written as $k^\mu = (k,0,0,k)$ where $k=\omega/c$. In this case the Lorentz gauge condition gives $A^{\mu 3} = A^{\mu 0}$. Therefore, we obtain a symmetric tensor with the first column identical to the fourth. Then, by using the condition $\Box \xi^\mu = 0$, we can rearrange the coefficients to obtain an $A^{\mu\nu}$ – tensor with all the coefficients null except A^{11}, A^{22}, A^{12}, A^{21}, with $A^{11} = -A^{22}$. In order to analyze just the orthogonal polarization, we can suppose that our GW has no A^{12} and A^{21} components. In this case our metric tensor will be

(1.2.1) $ds^2 = c^2 dt^2 - dx^2 [1 + A^{11} \cos(\omega(t-z))] - dy^2 [1 - A^{11} \cos(\omega(t-z))] - dz^2$

where we simply expressed

(1.2.2) $ds^2 = g_{\mu\nu} dx^\mu dx^\nu = (\eta_{\mu\nu} + h_{\mu\nu}) dx^\mu dx^\nu$

In order to detect this GW, we must use the same interferometer of Michelson-Morley experiment. In this experiment we have a laser generator (with typical wavelength of the laser $\lambda \approx 10^{-4}$ cm) is launched against a beamsplitter which has an angle of inclination of $\pi/4$. The beamsplitter splits the laser light into two beams directed down the arms of the interferometer, then they meet a mirror at the end of the interferometer, which reflects them. Before reaching the beamsplitter, after being reflected, (and this is an improvement of the Michelson Morley interferometer) the laser light meets a partially reflecting mirror which makes the light bounces many times between the mirror at the end of the interferometer and it, in order to make the light path longer. After that, the light comes back to the beamsplitter and then reaches the detector. The arm of the interferometer has the same length if there is no GW (roughly 1 km). When a GW arrives, there is a difference in the length of the two arms of the order of 10^{-16} cm depending on the amplitude of the wave. If $\Delta L \neq 0$, the detector measures a constructive interference if $\Delta L = n\lambda$, with n as an integer number. If instead $\Delta L = (n + \frac{1}{2})\lambda$, we have a destructive interference. If there is no GW, we have always a destructive interference. Therefore, if we obtain a constructive interference, we have the proof that a GW is passed. This (Figure 1) will show the experiment set up very clearly.

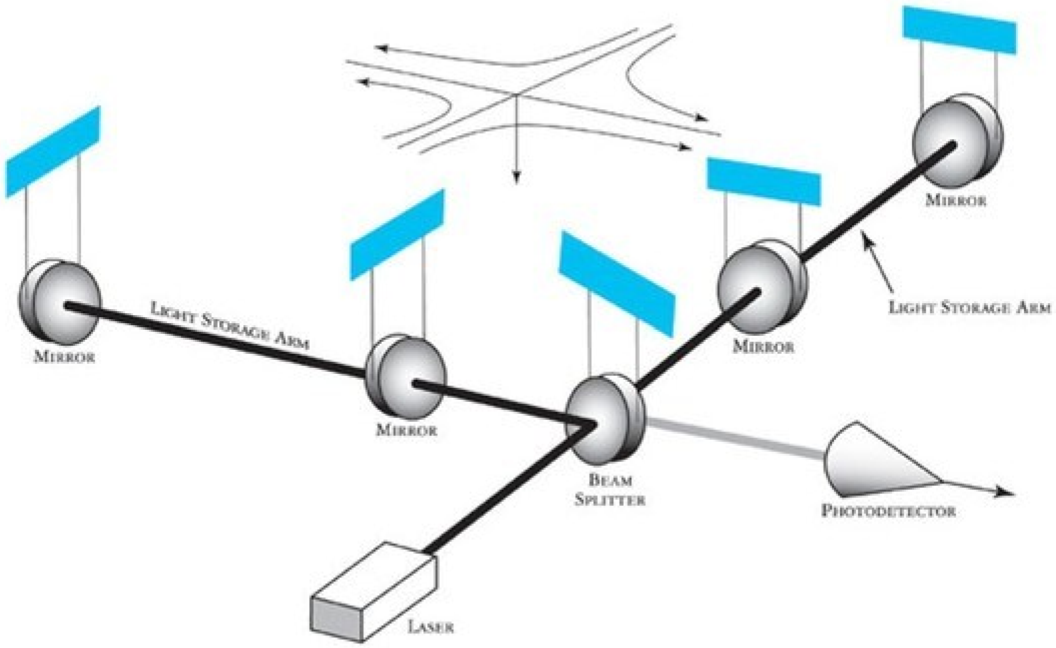

Figure 1: we can see the experimental set-up which is made of the laser emitter, a photodetector, a beamsplitter and 4 mirrors. The black lines represent the path of the laser light.

Now we are going to study the sensitivity of three, probably the most important, GWs experimental apparatuses for GWs detection: advanced Virgo, advanced Ligo and Kagra [2]. The sensitivity is obtained for Binary systems of Neutron Star, Binary systems made of a Black Neutron Star and for binary systems made of two Black Holes. In order to treat the sensitivity of our apparatus of detection, we have to consider V, the orientation-averaged spacetime volume covered per unit detector time. Then, we have to add a factor (1+ z) to our volume, where z is the redshift, because, considering the distance of the GWs source from us, the expansion of the universe cannot be neglected. The valid range of detection can be obtained from the volume V by using this formula:

(1.2.3) $\frac{4\pi}{3} R^3 = V$

For short-duration signals (<1s) or bursts it is possible to get the sensitive luminosity distance from the source. This distance can be calculated from this formula:

$$(1.2.4) \qquad D \approx \left(\frac{GE_{GW}}{2\pi^2 c^3 \, S(f_0) f_0^2 \rho_{DET}^2}\right)^{1/2}$$

where f_0 is the central frequency of the burst, $S(f_0)$ is the noise-power spectral density of the detector, ρ_{DET} is the single-detector threshold, E_{GW} is the energy related to the emission of the Gravitational Waves. Of course, this quantity must be corrected through the quantity (1+z) to obtain the range R. It is interesting to see in detail the detection equations considering the work by Patrick J. Sutton [3]. In calculating this formula, a flat cosmology was assumed, with Hubble parameter H_0= 67.9 km s^{-1} Mpc^{-1}, and density parameters, for non-relativistic matter and dark energy respectively, Ω_m=0.3065 and Ω_Λ=0.6935 [4].

The first thing to do is to write down the relation between the energy released by the Gravitational Waves and the LIGO-VIRGO standard measure for burst amplitude on the detector h_{rss} that can be defined as:

(1.2.5) $h_{rss} = \int_{-\infty}^{+\infty} dt\ [\ h_+^2\ (t) + h_x^2\ (t)] = 2 \int_0^{\infty} df\ [\ |\ \widetilde{h_+}\ (f)\ |^2 + |\ \widetilde{h_X}\ (f)\ |^2]$

The flux, the energy per unit area and unit time, of the Gravitational Waves is:

(1.2.6) $F_{GW} = \frac{c^3}{16\pi G} < \dot{h}_+{}^2\ (t) + \dot{h}_x{}^2\ (t)>$

The angle brackets indicate an average over several periods. If the Burst has a duration lower than T, it is possible to compute the average by integrating over the duration in this way:

(1.2.7) $F_{GW} = \frac{c^3}{16\pi G} \frac{1}{T} \int_{-T/2}^{T/2} dt\ [\dot{h}_+{}^2\ (t) + \dot{h}_x{}^2\ (t)] =$

$\frac{c^3}{16\pi G} \frac{1}{T} \int_{-T/2}^{T/2} dt\ [\ \int_{-\infty}^{+\infty} df'\ e^{i2\pi f't}\, i2\pi f'\ \widetilde{h_+^*}(f')\ \int_{-\infty}^{+\infty} df\ e^{-i2\pi ft}\, (-i2\pi f)\, \widetilde{h_+}(f)\ +$ (same thing with +→x)]

After doing the Fourier transformation, we consider that $h_{+,x} \rightarrow 0$, when $-T/2 \leq t \leq T/2$. Therefore, we can extend the integration for $-\infty \leq t \leq +\infty$. Thus, the time integral can be solved as a delta function $\delta(f' - f)$. What we obtain is:

(1.2.8) $F_{GW} = \pi c^3 \frac{1}{4GT} \int_{-\infty}^{\infty} df\ f^2\ [\ |\ \widetilde{h_+}\ (f)\ |^2 + |\ \widetilde{h_x}\ (f)\ |^2]$

Now, if we consider as valid the approximation of isotropic emission of the Gravitational Waves, and we consider a source at distance r, we get:

(1.2.9) $E_{GW} = 4\pi r^2\ T\ F_{GW}$

If we now suppose that our signal has a narrow band centered in f_0, we obtain:

(1.2.10) $E_{GW} = \frac{\pi^2 c^3}{G}\ r^2\ f_0^2\ h_{rss}^2$

Instead, if we assume that the GWs motion is Axisymmetric, we have this linearly polarized pattern of the emission:

(1.2.11) $h_+(t) = \sin^2(\iota)\, h(t)$

$h_x(t)=0$

where ι represents the angle between the symmetry axis and the line of sight of the observer and we choose a polarization basis aligned with this symmetry axis. In this case the emitted energy is:

(1.2.12) $E_{GW}=\frac{\pi c^3}{4G}\, r^2 \int_{-1}^{+1} d\cos(\iota) \int_0^{2\pi} d\lambda \int_{-\infty}^{+\infty} df\, f^2 \left(\sin^4(\iota)\, |\tilde{h}\,(f)\,|^2\right) = \frac{8}{15}\,\frac{\pi^2 c^3}{G} r^2 f_0^2\, h_{rss}^2$

In this equation, λ is the azimuthal angle in the frame of the GWs source. In this case the result is 8/15 times of that we get under the assumption of isotropic emission.

If we instead consider rotating system for the GWs emission, we obtain a result which is 2/5 times of the isotropic emission. In fact, we get:

(1.2.13) $E_{GW}=\frac{\pi c^3}{4G} r^2 \int_{-1}^{+1} d\cos(\iota) \int_0^{2\pi} d\lambda \int_{-\infty}^{+\infty} df\, f^2 \left[\frac{(1+\cos^2\iota)^2}{4} + \cos^2\iota\right] |\tilde{h}\,(f)\,|^2 = \frac{2}{5}\, \frac{\pi^2 c^3}{G}\, r^2 f_0^2\, h_{rss}^2$

After obtaining E_{GW}, we can write down the signal-to-noise ratio ρ for a matched filter as:

(1.2.14) $\rho^2= 2\int_{-\infty}^{+\infty} df\, |F_+ \widetilde{h_+} + F_x \widetilde{h_x}|^2 \frac{1}{S(f)}$

Where $S(f)$, as already seen, is the one-sided noise power spectrum and $F_{+,x}$ (θ, φ, ψ) are the antenna responses to the position in the sky (θ, φ) and the polarization ψ of the Gravitational Wave. If we assume a narrowband signal, we have [3]:

(1.2.15) $$\rho^2 = \frac{\Theta^2}{\alpha}\, \frac{G}{\pi^2 c^3}\, \frac{E_{GW}}{S(f_0) r^2 f_0^2}$$

In this equation Θ^2 is related to the quadratic sum of $F_{+,x}$ (θ, φ, ψ): $\Theta^2= F_+^2 + F_x^2$ for isotropic emission, $\Theta^2= F_+^2[(1+ \cos^2(\iota))/2] + F_x^2 \cos^2(\iota)$ for elliptical polarized emissions, and $\Theta^2= F_+^2\, 2\sin^4(\iota)$ for linearly polarized emissions. Then, we have $\alpha=1$ for isotropic emissions, $\alpha=8/15$ for linearly polarized emissions, $\alpha=2/5$ for circularly polarized emissions.

Now we are going to see the relation between the noise strain and the frequency in order to get the sensitivities for the three apparatus of GWs detection quoted before, respect to different sessions of observation.

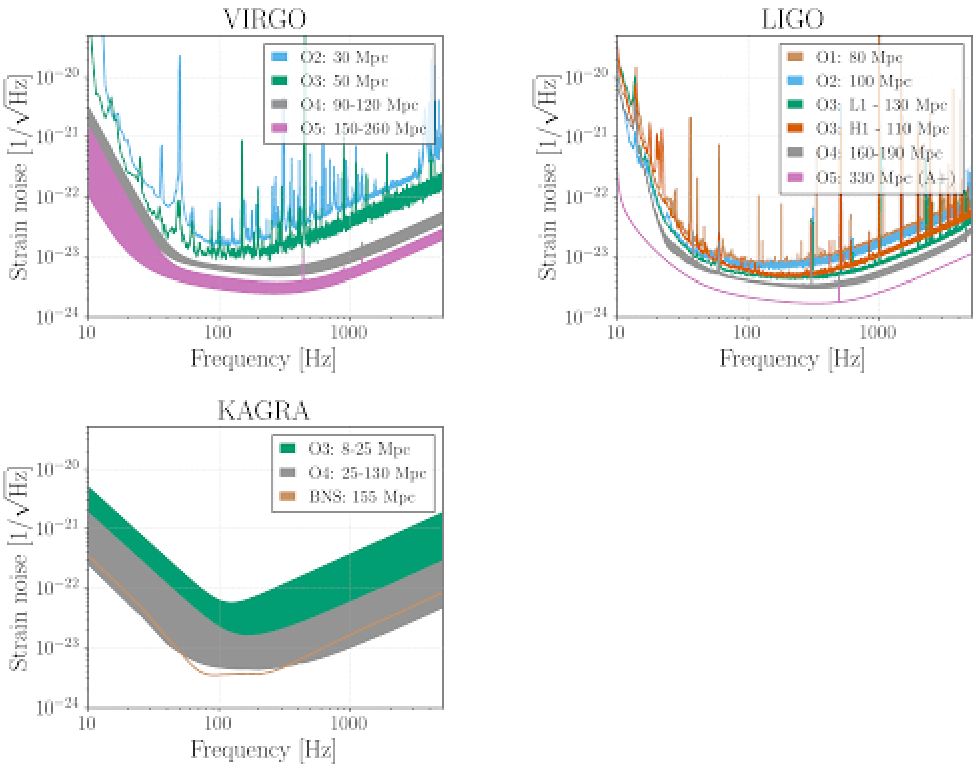

Figure 2: In this figure we see the relation between the Strain Noise on the y-axis and the frequency for Virgo, Ligo and Kagra for a NS binary system-detection. (O1, O2, O3, O4, O5 are the sessions of observation). [2]

Another very important result to show is a table related to the ranges of GWs detection in the same sessions of observation but even for Black Hole-Neutron Star (BHNS) mergers, Black Hole-Black Hole (BBH) mergers and for Bursts signal.

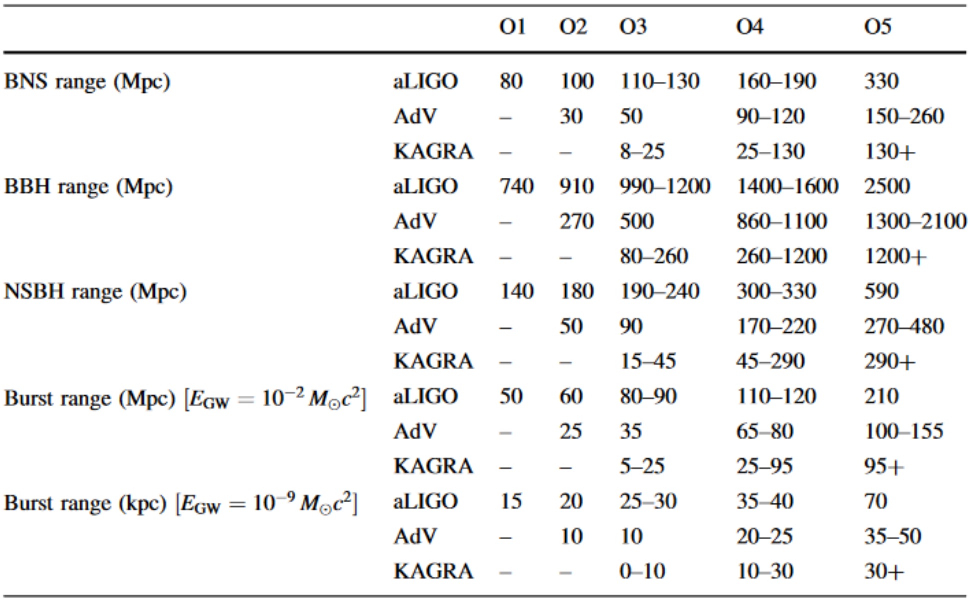

		O1	O2	O3	O4	O5
BNS range (Mpc)	aLIGO	80	100	110–130	160–190	330
	AdV	–	30	50	90–120	150–260
	KAGRA	–	–	8–25	25–130	130+
BBH range (Mpc)	aLIGO	740	910	990–1200	1400–1600	2500
	AdV	–	270	500	860–1100	1300–2100
	KAGRA	–	–	80–260	260–1200	1200+
NSBH range (Mpc)	aLIGO	140	180	190–240	300–330	590
	AdV	–	50	90	170–220	270–480
	KAGRA	–	–	15–45	45–290	290+
Burst range (Mpc) $[E_{\mathrm{GW}} = 10^{-2}\, M_\odot c^2]$	aLIGO	50	60	80–90	110–120	210
	AdV	–	25	35	65–80	100–155
	KAGRA	–	–	5–25	25–95	95+
Burst range (kpc) $[E_{\mathrm{GW}} = 10^{-9}\, M_\odot c^2]$	aLIGO	15	20	25–30	35–40	70
	AdV	–	10	10	20–25	35–50
	KAGRA	–	–	0–10	10–30	30+

Table 1: In this table we can see the range of sensitivity for advanced Ligo, advanced Virgo and Kagra for BNS (Binary Neutron Stars), BHNS (Black Hole-Neutron Star), BHBH

(Black Hole-Black Hole) systems and for bursts signals basing on the E_{GW}. We can see that for BHBH binary systems the range is higher than BHNS and BNS systems because the total mass which emits GWs is bigger, and the signal could be detected from further distances. [2]

It is also interesting to see how the sensitivity ranges of the three GWs detection apparatuses changed during the year and how they will be in the future.

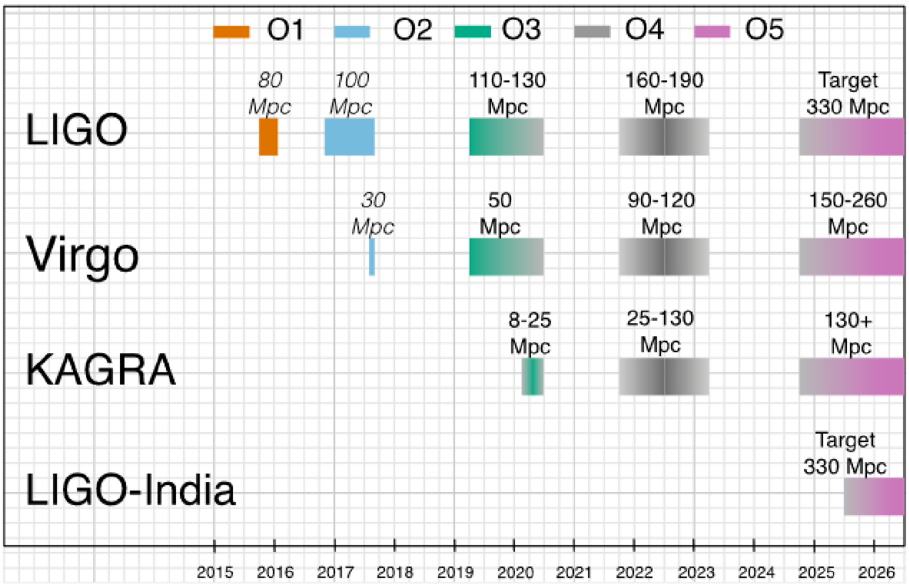

Figure 3: In this image we see 4 apparatuses for GWs detection: Ligo, Virgo, Kagra and Ligo-India that will be probably active in the future. On the horizontal axis are indicated the year in which the observations were made or will be made. From this image we can see that the sensitivity range is improving and Ligo is able to detect events from a distance which is longer than the other three apparatuses. [2]

1.2.1 Einstein Telescope, LIGO and DECIGO

Till now we have spoken of LIGO, VIRGO and KAGRA, but there are other approaches to Gravitational waves. One of this is the ET (Einstein Telescope) [5], [6]. The ET is a proposed underground infrastructure to host a gravitational- wave observatory. Compared to LIGO and VIRGO, the ET will achieve a greatly improved sensitivity by increasing the length of the arms of the interferometer: 3 Km for VIRGO, 10 Km for the ET. Beyond that, new technologies were used, such as a cryogenic system to cool some of the main optics to 10-20 K, new quantum technologies to reduce the fluctuations of the light and a set of noise-mitigation measures to drop the environmental influence on the data. The ET will be able to explore the universe history till the first cosmological epochs, providing information about the correctness of the theory of inflation or possible modifications of the General Relativity on cosmological scales. Besides this, the ET will be very useful also for the study of the mergers of compact objects. In fact, we will be able to observe the Neutron-Star inspiral phase and the onset of tidal fluctuations with a high signal-to-noise ratio giving us the possibility to analyze the interior structure of the Neutron Stars and to put under the possibility of confutation the theories of the exotic matter inside them. The ET great sensitivity to the kilohertz frequencies will allow us to probe details of the merger and the post-merger phase. The ET will operate with a new innovative generation of electromagnetic observatories covering the band from radio to gamma rays, such as the Square Kilometer Array and the Vera Rubin Observatory. The construction of the Apparatus is scheduled for 2026, but the first observations should begin in 2035. This is an image about the ET:

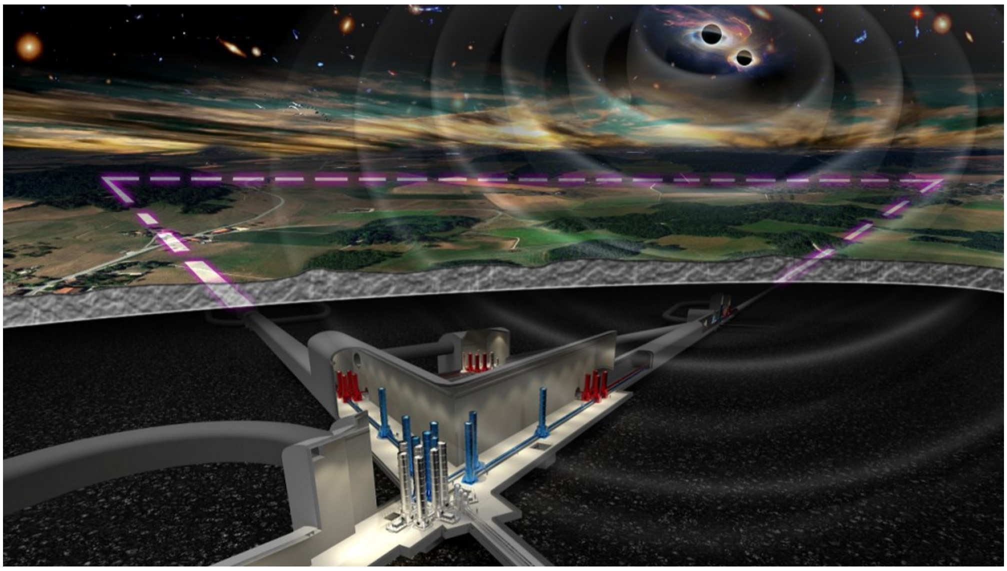

Figure 4: In this figure we see how the Einstein Telescope will be [5].

Another future experimental apparatus for GWs detection is LISA (laser interferometer space antenna) project by ESA (European Space Agency) [7]. This located in the space interferometer, developed by NASA and ESA, will be able to detect GWs low frequencies (from 0.1mHz to 1 Hz) and the launch is scheduled for 2034. The portion of the gravitational wave spectrum lying between the Lisa band and that probed by ground-based interferometers has great potential. The LISA mission uses three identical spacecraft whose positions mark the vertices of an equilateral triangle five million kilometers on a side, in orbit around the Sun. LISA could be considered as a giant Michelson interferometer in space, with a third arm which gives independent information on the two waves polarization. The spacecraft separation (the length of each arm of the interferometer, which is of 5 million kilometers) sets the range of the GWs frequencies that LISA can observe. LISA can detect gravitational wave induced strains of amplitude $h=\Delta l/l<10^{-23}$ in one year of observation, with a signal-to-noise ratio equal to five. The center of LISA apparatus traces an orbit with an elliptic plane, with the plane of the triangle with 60° inclined to the elliptic. LISA's orbit is 1 AU (astronomic unite) from the Sun. The LISA concept relies on unusual flight technologies like "drag free" flight and precision measurement techniques that are proved as good in laboratory. LISA has the great advantage respect to the GWs detection on Earth to detect four orders of magnitude better the GWs produced by BBH systems, and the thing does not change substantially for BHNS merger. The better quality of LISA detection is very useful not only to increase our knowledge about Neutron Stars and Black Holes properties, but also to prove or disprove the String Theory. In fact, in this theory the graviton, the quantum particle responsible of gravity, is thought to be massless and in this case the gravitational waves speed would not depend on the wavelength of the wave, as it should be in presence of massive graviton, but it should be equal to the speed of light. If the graviton was massive, analyzing the GWs signal related to the chirp mass of the merger, would be natural to find distorsions in the signal. If a gravitational wave is detected simultaneously in three independent detectors of ground-based array, and the direction of the source is determined in other ways, it is possible for the first time to know if the gravitational waves are made of only two polarization states or not. In fact, General Relativity predicts that there are only two modes irrespective of the source, whereas tensor-scalar theories predict a third polarization mode. LISA will be sensitive to varying mixtures of the polarization modes in the waves from a sufficiently long-lasting source, and in this way, LISA will be able to test the polarization content of the waves as well as it will be able to establish the direction of the source. This is an imagine about what LISA will be:

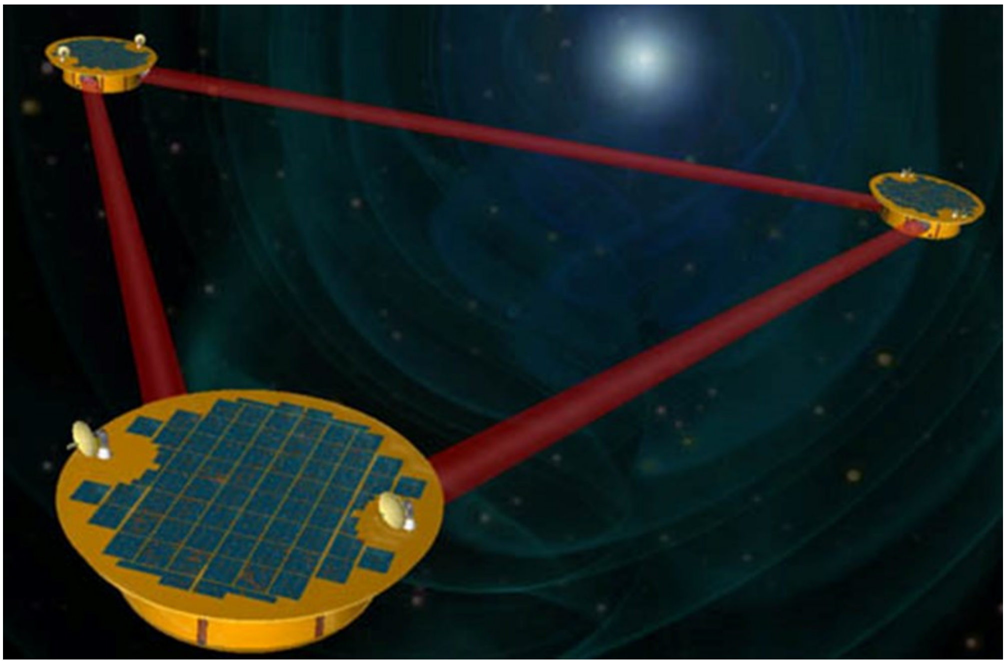

Figure 5:In this figure, we see how LISA will be once launched.

Another GWs detector is DECIGO, developed by JAXA (Japanese Aerospace eXploration Agency) which is a gravitational wave antenna located in Japan. The DECIGO pre-conceptual design consists of a drag-free spacecraft, whose relative displacements are measured by a differential Fabry-Perot (FP) Michelson Interferometer. The length of the arm is of 1000 Km and was chosen to realize a finesse of 10 with a 1 m diameter mirror and a 0.5 μm laser light. The mirror has a mass of 100 Kg and the laser has a power of 10 W. Its launch is scheduled for 2027. This is an imagine about what DECIGO will be:

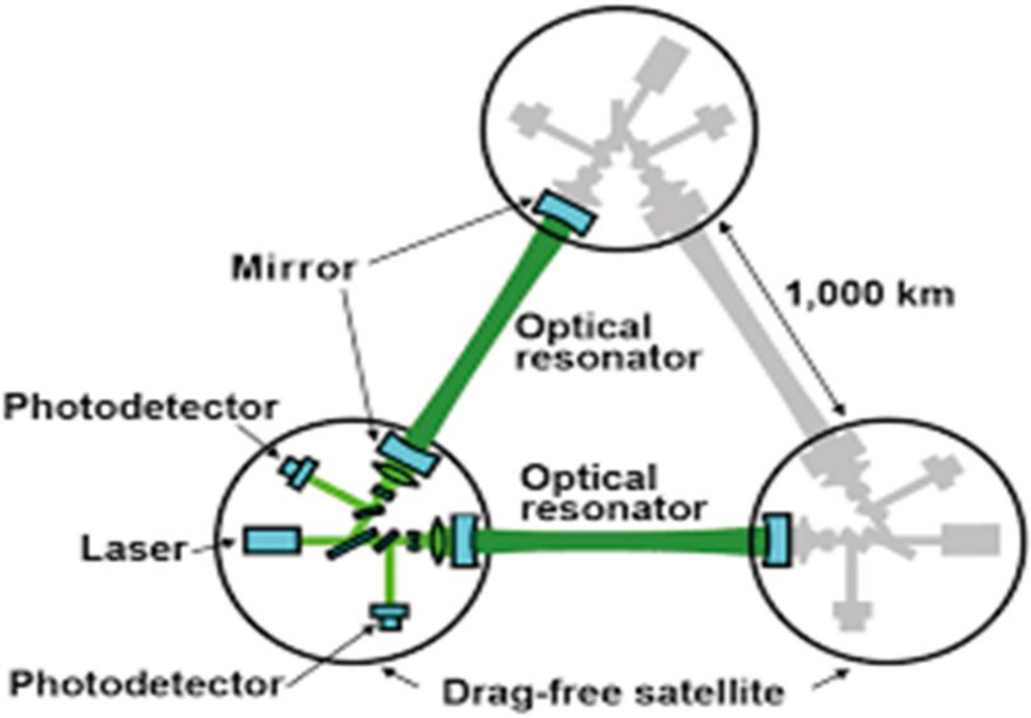

Figure 6: In this figure, we see how DECIGO will be. [7]

1.3 NSBH mergers: perspective for the future

1.3.1 NSBH events

Now we are going to treat four case of BHNS merger signals related to O3. While we have substantially no possible events about BHNS mergers signals related to O2, for O3 we have four possible events of this kind: S190910d [8] [9], S190923y [10] [11] , S190930t [12] [13] , S191205ah [14].

(a) S190910d event

This event has a very high probability of being related to a NSBH merger (98%), which is the highest compared to those of the three following events, and for this reason this event is the most interesting one. For this event, Fermi-GBM, where GBM means Gamma ray-burst monitor, detected no signal. The GBM search was run from -30 to +30 seconds around the merger time, the most sensitive for Gamma Ray signals. Even if no signal was found, the event is important because it allows us to put upper limits on the Gamma rays emission. In fact, assuming a luminosity distance of 606 Mpc from the GW detection, we have an intrinsic luminosity limit over the1 keV-10 MeV energy range (in units of 10^{48} erg/s). In order to detect the Gamma ray signal, the HAWC Collaboration, where the HAWC is a Gamma Ray water Cherenkov array located in Mexico, performed a search for a short timescale emission by using 6 sliding time windows (dt=0.3 s, 1 s, 3 s, 10 s, 30 s and 100 s), shifted forward in time by the 20% of their width.(This approach was considered also for the following three events).The sensitivity of its analysis depended a lot on the zenith angle, ranging from 0° to 45°, but for each of these angles there was not any Gamma Ray detection. For a 1 second Gamma ray signal, the upper limit of the flux is roughly $1.8x10^{-7}$ erg/cm^2/s, for an 8 second Gamma ray signal, the upper limit is instead $5.4x10^{-8}$ erg/cm^2/s.

In collaboration with Ligo and Virgo, the IceCube Neutrino Observatory, which is a cubic-kilometer neutrino detector operating at the South Pole, tried to find muon neutrinos in a range of time of 1000 seconds centered at the instant of merger, but nothing was observed.

(b) S190923y event

The probability of having a NSBH system for this event is of 68%, but there is a non-negligible probability for the signal to have terrestrial origin (32%), that is a noise signal. The situation for this event is analogous to that of the S190910d event. In fact, even in this case, using the same 6 sliding time windows used for S190910d, no event of gamma Ray Burst signal was detected. Even for this event the sensitivity of the approach of analysis made by HAWC Collaboration depended strongly on the azimuthal angle. The detection sensitivity to a 1 second burst, in the range of energy of 80-800 GeV, goes from $1.2x10^{-6}$ erg/cm^2 to $1.1x10^{-4}$ erg/cm^2 depending on the zenith angle, while for a 100 second burst, in the same range of energy, goes from $6.4x10^{-6}$ erg/cm^2 to $5.0x10^{-4}$ erg/cm^2. For a 1 second Gamma ray signal, the upper limit of the flux is roughly $3.4x10^{-7}$ erg/cm^2/s, for an 8 second Gamma ray signal, the upper limit is instead $6.7x10^{-8}$ erg/cm^2/s. IceCube Neutrino Observatory even in this case found no muon neutrino signal from the BNS (Binary Neutron Stars) merger.

(c) S190930t event

The probability of having a NSBH for this event is 74%. For this event, the Ligo-Livingston detector at the time of the trigger exhibits non-stationarity which is consistent with transient noise. They are still investigating the impact of this noise feature. For a 1 second Gamma ray signal, the upper limit of the flux is roughly $3x10^{-7}$ erg/cm^2/s, for an 8 second Gamma ray signal, the upper limit is instead $6.2x10^{-8}$ erg/cm^2/s. We have just the upper limit, because even for this event, no Gamma ray signal was detected. The same thing about neutrinos is valid for the IceCube Neutrino Observatory detection.

(d) S191205ah event

For this event, the probability of having a NSBH merger is roughly the 93%. Even in this case there is no Gamma Ray detection and the upper limit for the peak flux related to a 1 second Gamma ray signal is $1.6x10^{-7}$ erg/cm^2/s, while for an 8 second Gamma ray signal is $5.7x10^{-7}$ erg/cm^2/s. IceCube Neutrino Observatory found no detection also for this event.

1.3.2 NSBH environment

About NSBH mergers, we have to say that, from a theorical point of view, they have received a lower attention than BNS and BBH mergers. It is interesting to consider the studies, made by Hoang, Naoz and Kremer [15], about single-single GWs captures coming from BHNS mergers, based on five kinds of environment where there is a BHNS system: Galactic Field, Galactic Nuclei, Globular Cluster, Young Stellar Clusters and Mergers in Triples [15]. Single-single means that we have just two celestial bodies which interacts and there is no other companion of one of these objects in the interaction. We can now consider the five different environment and the possibility of having BHNS mergers in those. It is very useful for the future to study this topic, because, understanding what the possibility of finding NSBH mergers in different environments is, we can know where to look for, if we want to get more information about NSBH mergers.

a) NSBH mergers in the Field

The NSBH merger is studied a lot in this environment, which is that of isolation of the celestial bodies. Kruckow [15] in 2018 found an upper limit for NSBH merger rate which is 53 Gpc^{-3} yr^{-1}.

b) NSBH mergers in Globular Clusters

Neutron Stars have been well-observed in Globular Clusters since 1970s, also have BHs. For this reason, the possibility of NSBH merger cannot be neglected a priori. Clausen found a NSBH merger rate of roughly 0.01-0.17 Gpc^{-3} yr^{-1}that is, as we can see, much lower than that of the Field. More recently, in 2020, Ye considered dynamically formed NSBHs in Globular Cluster using a CMC code [15], which is a code for Clusters simulations, and obtained a rate of 0.009- 0.06 Gpc^{-3} yr^{-1}. But we have to say that these two studies were made with binary-single and binary-binary interactions.

c) Mergers in Galactic Nuclei

Arca Sedda [15] in 2020 studied binary-single in Galactic Nuclei and found a rate of roughly $9x10^{-3}$ -$1.5x10^{-2}$ Gpc^{-3} yr^{-1}. O'Leary focused on mergers of BBHs in Galactic Nuclei resulting from single-single GWs captures, by considering compact objects densities obtained by Fokker-Planck simulations. Using this kind of simulations, O'Leary in 2009 managed to estimate a rate for BHNS mergers, which is 10^{-11} yr^{-1} gal^{-1} (gal means galaxy) for a Galactic Nucleus around a Supermassive Black Hole of $4x10^{6}$ M_{o}. This rate is 1% of that of a BBH merger. Tsang [15] in 2013, under the same assumption of O'Leary [15] about the mass of Supermassive Black Hole in the center of the Galactic Nucleus, estimated a rate for BHNS mergers but using density profiles of an isothermal sphere, instead of those of Fokker-Planck simulations and found a merger rate of roughly $7x10^{-11}$-$9x10^{-10}$ yr^{-1} gal^{-1}. We must say that there are lots of uncertainties about the conversion from yr^{-1} $gal^{-1}$to Gpc^{-3} yr^{-1}. The fastest and the most immediate way is to multiply gal^{-1} by a galaxy number density in the universe to find the volumetric rate and then multiply what we have got by the observable volume related to our detection apparatus. The uncertainties arise from the fact that there may be different Galactic Nuclei with the same mass of the Supermassive Black Hole in the center with different central density profiles. The ratio between the volumetric rate and the detection rate, which we can call ξ, is not fixed, because of the variance of stellar densities in the Galactic Nuclei cusp. In this environment, with a Supermassive Black Hole, we can consider it as an element of perturbation in a BHNS merger. It is possible to consider the Eccentric Kozai-Lidov mechanism (EKL). Via this mechanism, in a binary system under the perturbative effect of a third body, the argument of pericenter or periapsis, which is $\omega= \arccos(n*e/|n|*|e|)$ where n is a vector pointing towards an ascending node and e is the eccentricity vector, oscillate about a constant value [16]. This figure will explain better what ω is:

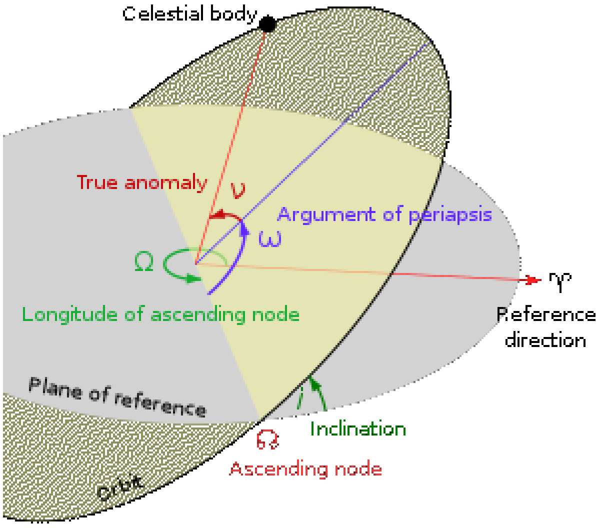

Figure 7: In this picture we see how the argument of periapsis for the EKL.

In 2019 Stephan [15] studied stellar binary evolution in Galactic Nuclei under the EKL mechanism induced by the Supermassive Black Hole and hypothesized that LIGO could detect BHNS mergers with a rate of 0.06-0.1 Gpc^{-3} yr^{-1}. If we compare the detection rate under the EKL mechanism and the one under single-single GWs capture made by O'Leary and Tsang, we see that if ξ is small, mergers induced by EKL mechanism are dominant over mergers from GWs capture. Conversely, if ξ is big, we have the opposite, or at least these two kinds of mergers are comparable.

d) Mergers in Young Stellar Clusters

Rastello [15] in 2020 studied the formation of BBHs in Young Stellar Clusters and found that Young Stellar Clusters have a NSBH merger rate higher than in the other cases: it is roughly 28 Gpc^{-3} yr^{-1}.

e) Mergers in Triples

A big number of studies has proven that roughly the 15% of massive Stars, which become Neutron Stars or Black Holes, have at least two stellar companions. Fragione and Loeb [15] in 2019 studied NSBH mergers in triples and found a rate of roughly 1.9x10^{-4} – 22 Gpc^{-3} yr^{-1}. As you see, the range is quite wide, because there are uncertainties about the metallicity of the massive Stars.

1.3.3 Single-single GWs capture

Now, we are going to see how single-single GWs capture can be obtained [15]. We consider the assumption of hyperbolic encounters between the two compact objects. Thus, we can write down the fraction of gravitational energy emitted by the interaction between a Neutron Star and a Black Hole:

$$(1.3.1)\quad \Delta E_{GW} = -\frac{85\pi G^{7/2}\,\eta^2 M_{TOT}^{9/2}}{12\sqrt{2}c^5 r_p^{7/2}}$$

Where c is the speed of light, G is the gravitational constant, $M_{TOT} = m_{BH} + m_{NS}$, with m_{NS} mass of the Neutron Star and m_{BH} mass of the Black Hole.

$$(1.3.2)\quad \eta = \frac{m_{BH}\, m_{NS}}{(m_{BH} + m_{NS})^2}$$

$$(1.3.3)\quad r_p = \left[\frac{1}{b^2} + \frac{G^2 M_{TOT}^2}{b^4 v_{REL}^4} + \frac{G\, M_{TOT}}{b^2 v_{REL}^2}\right]^{-1/2}$$

r_p is the distance of the closest approach of the encounter. In the (1.3.3) formula, b is the impact parameter and v_{REL} is the relative velocity between the Neutron Star and the Black Hole.

Now, if $|\Delta E_{GW}| > (M_{TOT}\,\eta\, v_{REL}^2)/2$, when the energy emitted by gravitational waves is bigger than the kinetic energy of the encounter, a bound BHNS system is present. By considering this inequality, we can write down the maximum impact parameter to have a bound BHNS system.

$$(1.3.4)\quad b_{MAX} = \left(\frac{340\pi\eta}{3}\right)^{1/3}\left(\frac{GM_{TOT}}{c^2}\right)\left(\frac{v_{REL}}{c}\right)^{-9/7}$$

We can also obtain a minimum impact parameter, which is:

$$(1.3.5)\quad b_{MIN} = \left(\frac{4GM_{TOT}}{c^2}\right)\left(\frac{v_{REL}}{c}\right)^{-1}$$

For $b < b_{MIN}$, we have a direct collision and not a bound state. Thus, we can define the bound state cross section, which is:

$$(1.3.6)\quad \sigma\,(m_{BH}, m_{NS}, v_{REL}) = \pi\,(b_{MAX}^2 - b_{MIN}^2)$$

Actually, the situation is little more complex, because for now we have neglected the contribute due to the tidal deformability of the Neutron Star which affects σ. To understand whether the tidal contribute can be neglected or not, in our parabolic encounter approximation, we have to consider the tidal energy dissipated during the parabolic encounter, which is the following:

(1.3.7) $\Delta E_T = (\frac{GM_{NS}^2}{R_{NS}}) (\frac{m_{BH}}{m_{NS}})^2 \sum_{l=2,3,..} (\frac{R_{NS}}{R_{MIN}})^{2l+2} T^l$

Where R_{NS} is the radius of the Neutron Star, R_{MIN} is the radius of the periastron and T^l is a dimensionless number related to any spherical harmonic l. In this situation we neglect the contribution associated to l>2. (The tidal deformability is better treated in paragraph number 1.5) We also assumed the Neutron Star as a polytropic body with polytropic index n=0.5. Knowing b, we can get $R_{MIN}(b)$ as the minimum value for the periastron in relation with the impact parameter. This relation is the following:

(1.3.8) $R_{MIN}(b) = \frac{b^2 v_{REL}^2}{2GM_{TOT}}$

Putting into this equation the value of b_{MIN} obtained by (1.3.5), we can write down this equation:

(1.3.9) $R_{MIN}(b_{MIN}) = \frac{8GM_{TOT}}{c^2}$

For $R_{MIN} < R_{MIN}(b_{MIN})$, there is a direct collision, so we do not consider these values for R_{MIN}. We can know plot the relation between $\Delta E_T / \Delta E_{GW}$ and R_{MIN} with $m_{NS} = 1.4\ M_o$ and $m_{BH} = 5\ M_o$.

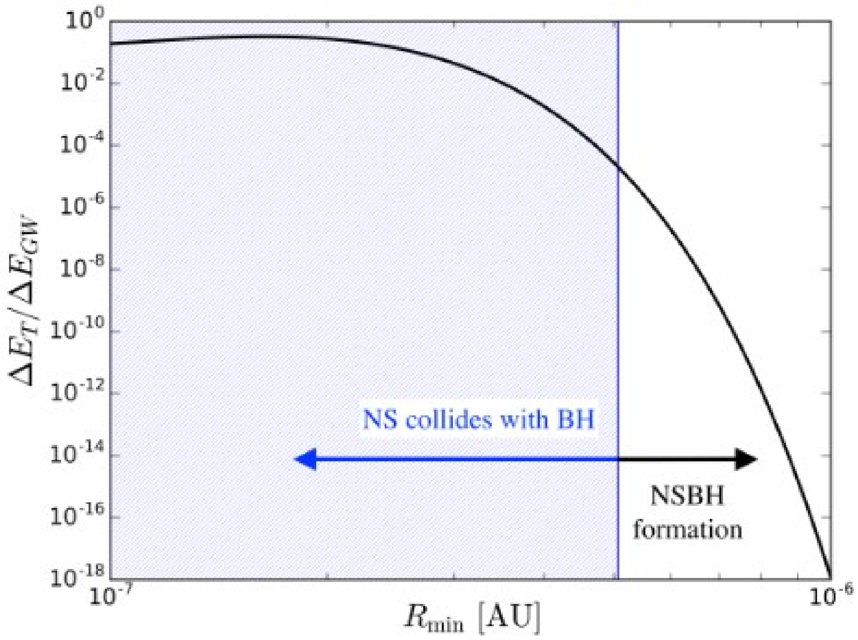

Figure 8:In this image, we see the relation between the $\Delta E_T / \Delta E_{GW}$ ratio and the minimum value for the periastron. The blue vertical line marks the boundary between NSBH formation and the NSBH collision. [15]

As we can see from this graph, we can neglect ΔE_T, because the ratio $\Delta E_T / \Delta E_{GW}$ is at most equal to 10^{-4}.

1.3.4 Event rates for BHNS in single-single GWs capture in different environments

We can now calculate the rate of NSBH binary formation for a single cluster, which is:

(1.3.10) $\Gamma_{cl} = \int dr\, 4\pi r^2\, n_{BH}(r)\, n_{NS}(r)\ x \int dm_{BH}\, f_{BH}(m_{BH}) \int dm_{NS}\, f_{NS}(m_{NS})\ x \int dv_{REL}\, \psi_{mBH,mNS}(r, v_{REL}) \sigma v_{REL}$

Where $n_{BH}(r)$ and $n_{NS}(r)$ represent the number density of a Black Hole and of a Neutron Star, respectively. $f_{BH}(m_{BH})$ and $f_{NS}(m_{NS})$ are the mass probability distribution for a Black Hole and a Neutron Star, respectively. $\psi_{mBH,mNS}(r, v_{REL})$ indicates the distribution of the relative velocity between a Black Hole and a Neutron Star at distance r. For Globular Clusters, it is possible to approximate the Black Holes and the Neutron Stars population by using a Maxwellian distribution. We can then calculate the relative velocity between Neutron Stars and Black Holes in a cluster, and we obtain:

(1.3.11) $< v_{REL} > = [\frac{8}{\pi} (v^2_{d,\,BH} + v^2_{d,\,NS})]^{1/2}$

Where $v_{d,\,BH}$, $v_{d,\,NS}$ are the dispersion velocity of Neutron Stars and Black Holes, respectively. We can put this value of v_{REL} in the equation (1.3.10). Thus, neglecting any dependence of v_{REL} on r, we can write down the last integral of the equation (1.3.10) and we have:

(1.3.12) $\int_{GC} d\, v_{REL}\, \psi_{mBH,mNS}(r, v_{REL}) \sigma v_{REL} \approx \sigma < v_{REL} >$

If we have instead a Galactic Nucleus, where our BHNS system is present, we can write the same integral as:

(1.3.13) $\int_{GN} d\, v_{REL}\, \psi_{mBH,mNS}(r, v_{REL}) \sigma v_{REL} \approx \sigma v_c(r)$

Where $v_c(r)$ is the circular velocity around the center of the Galactic Nucleus. $v_c(r) = (G\, m_{SMBH}/r)^{1/2}$. Hence, in this last case, there is a low dependence of the integral on v_{REL}. And in this last case σ is evaluated when $v_{REL} = v_c(r)$. We can know obtain the BHNS merger volumetric rate from Γ_{cl}, both in the case of Globular Clusters and Galactic Nuclei, as:

(1.3.14) $\Gamma_{BHNS} = n_{cl}\, \Gamma_{cl}$

Where n_{cl} is the density of clusters.

a) Single-single GWs capture from Globular Clusters (Hoang's work)

About Globular Clusters, we need to distinguish old Globular Clusters from young ones, respectively Clusters with 10 Gyr of age and 1 Gyr. To obtain a solution from the integral (1.4.10), we must calculate numerically $n_{BH}(r)$, $n_{NS}(r)$, $f_{BH}(m_{BH})$ and $f_{NS}(m_{NS})$ from the simulation data, where at t=1 Gyr we have 527 Black Holes and 825 Neutron Stars, and at t=10 Gyr we have

38 Black Holes and 778 Neutron Stars. We can use $< v_{REL} >$ to put in our integral. We find eventually a total merger rate for BHNS merger for a single Globular Cluster of roughly $4x10^{-15}$ yr^{-1} for the t=1 Gyr Globular Cluster, and $2x10^{-14}$ yr^{-1} for t=10 Gyr Globular Cluster. The reason for this discrepancy between old and young Globular Clusters is due to the fact that, if the Cluster is young, we have Black Holes with a high mass (5-40 M_o), and Black Holes form a subsystem in the center of the Cluster, and they produce a great amount of energy through binary dynamical processes. The Spitzer mass-segregation instability process prevents the migration of lower stars masses to the Cluster's center and makes the massive Black Holes go towards the Cluster's center, decoupling the Black Holes in the interior regions from the other celestial bodies in the external regions. In this way, there are no Neutron Stars in the center of the Cluster, where Black Holes are dominant, and we have Black Holes and Neutron Stars able to merge just in the external regions of the Cluster, where we have low densities, and hence it is difficult that a merger could occur. Nonetheless, this segregation does not last forever, because, as proven by Morscher [15], the Black Holes in the center formed binaries through three-body interactions, and single and binaries Black Holes are ejected towards the outer regions of the Cluster. Then, with the reduction of the number Black Holes inside the center of the Cluster, more Neutron Stars can penetrate the inner regions. All this makes the probability of BHNS mergers higher. Nevertheless, even though we consider old Globular Clusters, the volumetric BHNS merger rate is anyway very low. For example, considering n_{cl}=2.9 Mpc^{-3} as density of Globular Clusters in the universe, we obtain a volumetric BHNS merger rate $\Gamma_{BHNS} \approx 10^{-5}$ Gpc^{-3} yr^{-1} for 1 Gyr age Clusters, and $\Gamma_{BHNS} \approx 7x10^{-5}$ Gpc^{-3} yr^{-1} for 10 Gyr age Clusters. As we can see, the volumetric merger rate related to single-single GWs capture is much lower than that related to binary-single or binary-binary GWs capture.

b) Single-single GWs capture from Galactic Nuclei (Hoang's work)

About Single-single GWs capture for Galactic Nuclei, 4 different theoretical models were considered in which were considered or not the presence of compact objects in outer or inner regions of the Galactic Nuclei depending on the model. As shown before, the relative velocity of the encounters at distance r from the center was put equal to the circular velocity at value r. Adopting n_{cl}=0.02-0.1 Mpc^{-3}, we obtain $\Gamma_{BHNS} \approx$ 0.001-0.06 Gpc^{-3} yr^{-1} which is a little bit higher than in the case of binary-binary or binary-single GWs capture. As seen before, this volumetric rate can be enhanced by a factor ξ, which is not well known.

We can now compare the BHNS merger rate per Globular Cluster or per Galactic Nucleus in relation with the distance r, in single-single GWs capture.

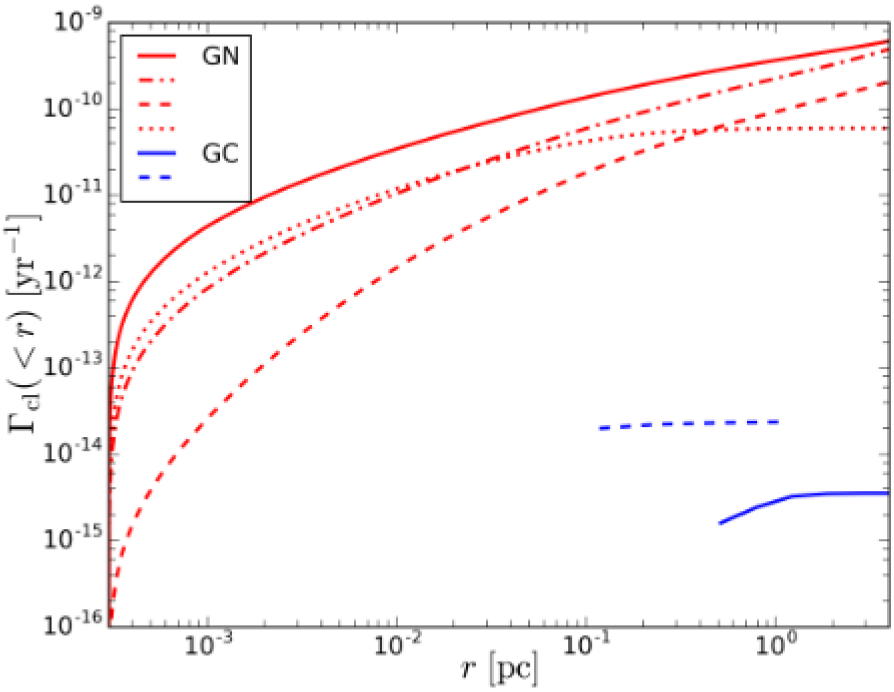

Figure 9: In this figure, we see plotted the relation between the BHNS merger rate in single-single GWs capture and the distance. The 4 different lines are referred to 4 different models for Galactic Nuclei, while the two blue lines are referred to the Globular Cluster: the blue continuous line corresponds to the 1 Gyr case, while the blue dashed line to the 10 Gyr case. [15]

c) Single-single GWs capture from Young Stellar Clusters (Hoang' s work)

To obtain the BHNS merger rate in Young Stellar Clusters through the single-single GWs capture channel, we have to calculate $n_{BH}(r)$ and $n_{NS}(r)$ of the (1.4.10) equation. These radial distributions are found by fixing the initial cluster mass, at t=0, $M_{cl}(0)=7.5\times10^4\ M_o$, and metallicity $Z= 0.01\ Z_o$, where Z_o is the metallicity of the Sun, by putting $m_{BH}=20\ M_o$ and $m_{NS}=1.4\ M_o$, considering the velocity of dispersion equal to 3 Km/s. Then an evolution in different instants of time (100 Myr, 1000 Myr, 5000 Myr, 7500 Myr and 10 Gyr). What we get is that the BHNS merger rate decreases with time. This is the opposite to what happens for Globular Clusters. For t=100 Myr, we have $\Gamma_{cl} \approx 10^{-13}\ yr^{-1}$, for t>5 Gyr, we have $\Gamma_{cl} \approx 10^{-16}\ yr^{-1}$. The reason why there is such drop is due to the dispersion of celestial bodies with the evolution of the Young Stellar Cluster, and this fact reduces the probability of BHNS merger events. At this point we must calculate the volumetric BHNS merger rate, but the equation is not the same as the one for Globular Clusters and Galactic Nuclei (1.4.14). The correct equation in this case is the following:

$$(1.3.15)\qquad \Gamma_{NSBH,\,YSC} \approx \Gamma_{cl,\,YSC}\ t_{eff}\ \rho_{SF}\ f_{SF} / M_{cl}(0)$$

Where $\Gamma_{NSBH,\,YSC}$ is the volumetric BHNS merger rate, $\Gamma_{cl,\,YSC}$ indicates the BHNS merger rate per Young Stellar Cluster, $\rho_{SF}= 1.5\times10^{-2}\ M_o\ Mpc^{-3}$ is the density of star formation at z=0, where z is the redshift, $f_{SF} = 0.8$ is the fraction of star formation which takes place in the Young Stellar Cluster, and a fixed lifetime t_{eff}=100 Myr , which is not the real lifetime, but, considering the time of the highest probabilities for BHNS merger processes, it is not a bad approximation to put the lifetime of the Young Stellar Cluster equal to t_{eff}=100 Myr. Thus, we find $\Gamma_{NSBH,\,YSC} \approx 2 \times 10^{-3}\ Gpc^{-3}\ yr^{-1}$.

We can now show all the results in the following plot:

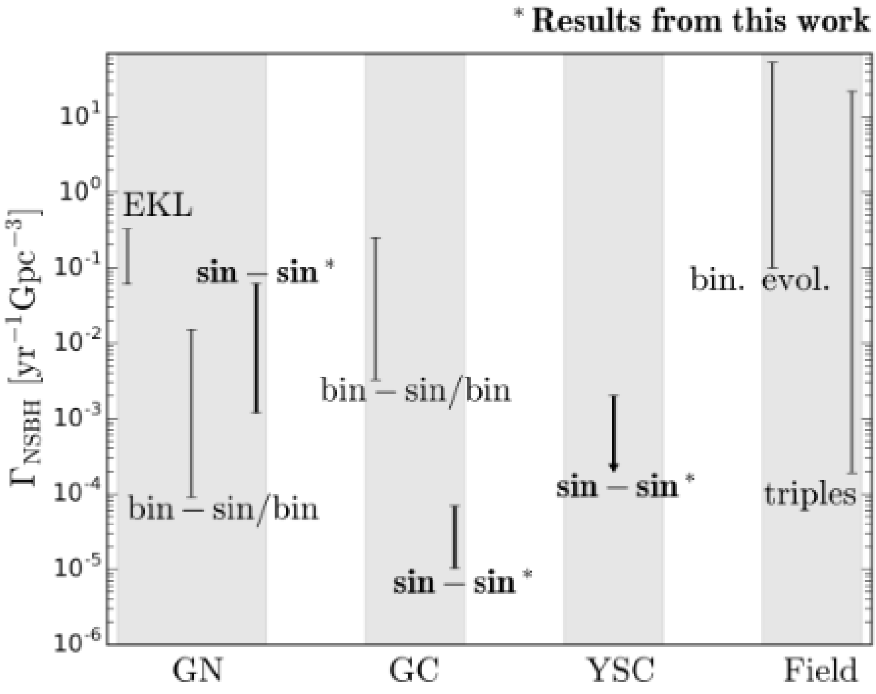

Figure 10:In this figure we see the volumetric rate for BHNS merger relation with the Galactic Nuclei, the Globular Clusters, the Young Stellar Clusters and the Field for different GWs capture mechanisms (single-single, single-binary, binary-binary, EKL, triples). [15]

We can see that the best chance to observe BHNS merger volumetric rate from single-single GWs capture is from Galactic Nuclei, even if we pay the price of our lack of knowledge about the ξ factor. In fact, non-taking into consideration ξ in this work could underestimate the BHNS merger volumetric rate. If we consider ξ of the order of tens, BHNS merger volumetric rate from single-single GWs for Galactic Nuclei is comparable with that of EKL. In the future, if LIGO detects some amount of BHNS mergers, it will be possible to know if this rate is underestimated and how big is the discrepancy between theoretical prevision and experimental results, by looking at the eccentricity distributions of this mergers. Advanced LIGO is able to distinguish binary mergers with eccentricity from those without this. The work by Hoang is very important, because, beyond as dealing in details with the study of the galactic structures, letting us discover some properties we do not know about them, such as the stellar density in Galactic Nuclei cusp, it makes our work of BHNS mergers observation easier, because we can know where they are with higher probability, and with more BHNS merger detections, we will have more samples to study and hence more information about the Nuclear and Subnuclear Physics at our disposal.

1.4 How to discriminate among BNS, BHNS, GAP AND BBH systems

The study of gravitational waves is very useful to understand what kind of binary system we are dealing with. We will concentrate on J. Lattimer's study [17] about how to make this discrimination even though it is probabilistic. There are three possible binary systems: Neutron Star- Black Hole, Neutron Star- Neutron Star, Black Hole-Black Hole. So, we can calculate p_{BNS}, the probability to deal with a binary-neutron stars system, p_{BHNS}, the probability to have a coalescence of one neutron star and one black hole, p_{BBH}, the probability of having a binary-black holes system and p_{GAP}, the probability of indetermination, because in this model have been considered as associated to neutron stars all the masses less than $3M_o$, and to black holes all the ones higher than $5M_o$. If the mass of one or of both components was between $3M_o$ and $5M_o$, the situation would have returned in the mass gap case. Nevertheless, considering that it is very unlikely to have neutron stars with mass higher than $3M_o$, an object like this is allegedly a black hole. In order to obtain these probabilities, we have to start from the chirp mass. The chirp mass can be expressed as $\mathcal{M}= (M_1\ M_2\ )^{3/5}/\ (M_1 + M_2\ )^{1/5}$. In general relativity the chirp mass is a fundamental parameter which determines the evolution of the amplitude and frequency of a gravitational wave produced by a binary system during the inspiral phase. At the lowest order of a Post-Newtonian expansion, which is obtained by a perturbation of the Newtonian law of gravity when the speed of the two bodies is very little compared to the speed of light, we can express the chirp mass in this way, as was done by Tiwari [18] :

$$(1.4.1)\ \mathcal{M}= \frac{c^3}{G}\left[\frac{5}{96}\ \pi^{-8/3}\ f^{-11/3}\ df/dt\right]^{3/5}$$

where c is the speed of light, G the gravitation constant, f the frequency of spiraling and df/dt is its derivative respect to time.

By using this equation, we can obtain the expression of df/dt which is:

$$(1.4.2)\ df/dt= \frac{96}{5}\ \pi^{8/3}\left(\frac{G\mathcal{M}}{c^3}\right)^{5/3} f^{11/3}$$

By solving it we get:

$$(1.4.3)\ \frac{96}{5}\ \pi^{8/3}\left(\frac{G\mathcal{M}}{c^3}\right)^{5/3} t +\frac{3}{8}\ f^{-8/3} + C=0$$

where C is an integration constant.

Then, by imposing x=t and y= (3/8) $f^{-8/3}$, the chirp mass can be computed by the line inclination obtained on a plane with (x , y)-coordinate system. After measuring the frequencies and their derivatives, it is possible to obtain $\mathcal{M}$. Nonetheless, $\mathcal{M}$ is not the only parameter we need in order to obtain the probabilities for each kind of binary system (BNS, BHNS, BHBH). We also need to know $q=M_1 /M_2 \geq 1$. In order to calculate q, we have to consider the first order of the post-Newtonian expansion [19]. The way to get q is to calculate the reduced mass $\mu = M_1M_2/(M_1 + M_2)$. After knowing this, considering that we already know the chirp mass, we can calculate q. The way to obtain the reduced mass is to consider the relation between the reduced mass and the logarithmic derivative of the number of cycles, related to the inspiral motion of the binary system, respect to the frequency of the GWs. The relation is the following [20]:

$$\frac{dN_{CYCLES}}{dlnf} = \frac{5}{96\pi}\left[\frac{1}{\mu M^{2/3}(\pi f)^{5/3}}\right]\left\{1 + \left[\frac{743}{336} + \frac{11\mu}{4M}\right]x - [4\pi + (S.O.)x^{1.5} + (S.S.)x^{2} + o(x^{2.5})]\right\} \tag{1.4.4}$$

where N_{CYCLES} is the number of cycles of the inspiraling Gravitational Waves emitted by the binary system, f is the frequency of the GWs, M is the total mass of the binary system, μ is of course the reduced mass, $x = (\pi M f)^{2/3} \approx M/D$ is the Post-Newtonian expansion parameter (where c=G=1). In this equation, beyond the PN- correction, we have the $P^{1.5}N$-correction, where the 4π is connected to the interaction between the GWs and the binary's monopolar gravitation field, and S.O. is the contribution due to the spin-orbit coupling, the interaction between the spin of the binary bodies and the angular momentum. The $P^{2}N$-correction is instead the spin-spin coupling, related to the spin interaction of the two bodies with themselves.

It is now possible to write down a gaussian distribution probability function with the average values ($\mathcal{M}_0$, q_0) and relative errors ($\sigma_{\mathcal{M}}$, σ_q). Nonetheless, in order to avoid overruns in non-physical regions, it is better to replace q with $q_* = \ln(q-1)$ with $q_* \in [-\infty, \infty]$.The formula is:

$$\frac{dp^2}{d\mathcal{M}d\,q_*} = A\ exp\left[-\frac{(\mathcal{M}-\mathcal{M}_0)^2}{2\sigma_{\mathcal{M}}^2} - \frac{(q_* - q_{*0})^2}{2\sigma_q^2}\right] \tag{1.4.5}$$

where

$A = 1/[2\pi(\sigma_{\mathcal{M}}\sigma_q)^{1/2}]$.
In this model $\mathcal{M}$ and q_* were assumed as uncorrelated. We can expect that $\sigma_{\mathcal{M}}$ is smaller than σ_q, so it was neglected. Now for given values $\mathcal{M}_0$ and q_{*0} was calculated the integral of the gaussian distribution probability function written above, over all possible values $\mathcal{M}$ and q_* related to BNS, gap, BHNS,BBH giving the relative probabilities. This is the plot (figure 10) obtained by putting $\sigma_{\mathcal{M}} = 0.01\ \mathcal{M}$ and $\sigma_q = [1.0, 2.5]$, with $\mathcal{M}$ on the x-axis and q_* on the y-axis.

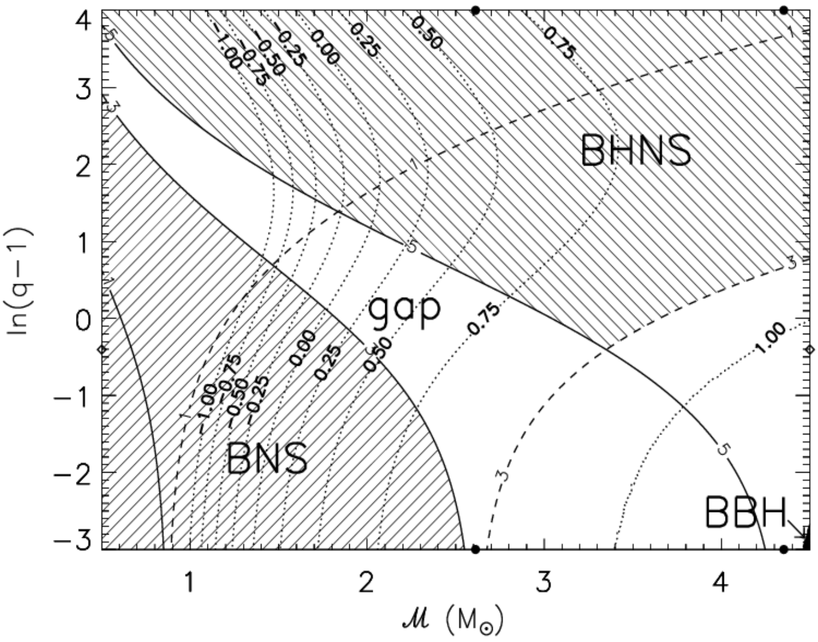

Figure 11:In this plot we have In(q -1) on the y-axis and Ɱ on the x-axis. We see different regions (BHNS, BNS, gap, BBH) depending on these two values. The dotted lines indicate different values of the spin parameter χ between -1 and 1. [17]

1.5 Tidal Deformability in NS binary systems and in Neutron Star-Black Hole systems

Flanagan and Hinderer [21] analyzed tidal deformability in a binary neutron stars system writing down a model who connected tidal deformability, which influenced the gravitational wave signal, to EOS equation of state of the neutron star in order to obtain information about the structure of the star. LIGO showed that tidal effects change evolution just at the end of the inspiral motion, letting us treat tidal deformability as perturbation of the point-particle Post-Newtonian waveform. Only when the late inspiral approaches, tidal deformability becomes very strong, and it is not possible anymore to use a perturbation model and numerical solutions become the only way to face the question. However, Flanagan and Hinderer showed the presence of a small but clean signal related to deformability when the inspiral was below 400 Hz. This signal can be described by using a parameter called λ which depends on EOS only via neutron star radius R and a dimensionless quantity k_2 called Love number. The expression of deformability is:

(1.5.1) $$\lambda = \frac{2}{3G} k_2 R^5$$

Flanagan and Hinderer at first considered the Love number in the approximation of polytropic equation of state where the pressure P depends only on the energy density ρ in this way $P=K\rho^{1+1/n}$ with K as constant and n polytropic index which is equal to 3/2 in the non-relativistic limit and equal to 3 in the relativistic one. In the polytropic approximation they overestimate the Love number by a factor of 2-3. In order to calculate the Love number and the tidal deformability, they considered a static, spherically symmetric star in a static external quadrupole tidal field ϵ_{ij}. The induced quadrupole momentum was Q_{ij} and $Q_{ij} = -\lambda \epsilon_{ij}$. Now we can write an expression related to the metric tensor time component which is the combination of a standard part of Schwarzschild metric, a part of external tidal field which goes as r^2 and a part of tidal distorsion which decreases as r^{-3}. The expression, where G=c=1, is the following:

$$(1.5.2) \quad \frac{-(1+g_{tt})}{2} = -\frac{m}{r} - \frac{3Q_{ij}}{2r^3} n^i n^j + \ldots + \frac{\varepsilon_{ij}}{2} r^2 n^i n^j$$

where $n^i = x^i / r$.

In order to obtain the equation above is necessary a linear perturbation expanded in spherical harmonics by considering the azimuthal number m=0 because the deformation is axisymmetric respect to the line connecting the centers of the stars, and l=2 if the model is valid for the early stages of the inspiral. Considering these approximations, we can finally write down the metric tensor:

$$(1.5.3) \quad ds^2 = -e^{2\varphi(r)}[1 + H(r)Y_{20}(\theta,\varphi)]dt^2 + e^{2\Lambda(r)}[1 - H(r)Y_{20}(\theta,\varphi)]dr^2 + r^2[1 - K(r)Y_{20}(\theta,\varphi)](d\theta^2 + \sin\theta^2 \, d\varphi^2)$$

Where K'(r)= H' (r) + 2 H(r) φ' (r) and H(r) is the solution of the following differential equation

$$(1.5.4) \quad [-\frac{1}{r}(\frac{6}{r} e^{2\Lambda(r)}) - 2\dot{\varphi}(r)^2 + 2\ddot{\varphi}(r) + \frac{3}{r}\dot{\Lambda}(r) + \frac{7}{r}\dot{\varphi}(r) - 2\dot{\varphi}(r)\dot{\Lambda}(r) + \frac{f}{r}(\dot{\varphi}(r) + \dot{\Lambda}(r))] H(r) + (\frac{2}{r} + \dot{\varphi}(r) + \dot{\Lambda}(r)) \dot{H}(r) + \ddot{H}(r) = 0$$

where $f = \frac{dP}{d\rho_e}$

The method that Hinderer and Flanagan used to obtain the tidal perturbation was by an augmentation of the TOV equations system in this way:

$$(1.5.5) \quad e^{2\Lambda(r)} = \left(1 - \frac{2m}{r}\right)^{-1}$$

$$(1.5.6) \quad \frac{d\varphi}{dr} = -\frac{dP}{dr}\frac{1}{P + \rho_e}$$

$$(1.5.7) \quad \frac{dP}{dr} = -(P + \rho_e)(m + 4\pi r^3 P)\frac{1}{r(r-2m)}$$

$$(1.5.8) \quad \frac{dm}{dr} = 4\pi r^2 \rho_e$$

As we can see the third of these equations, which is obtained by solving the Einstein’s equation $R_{\mu\nu} - \frac{1}{2} g_{\mu\nu} R = kT_{\mu\nu}$ as you can do like in the Schwarzschild case with the difference now of a non-vanishing $T_{\mu\nu}$ in the situation of ideal gas where $P=P(\rho_e)$ and without viscosity, is the relativistic generalization of the equation of hydrostatic equilibrium which is: $dP/dr = -m(r)\,\rho_e(r)/r^2$.

Now, in order to solve our system of ODEs, it is better if we put $\beta(r) = dH(r)/dr$ and we rewrite the second order differential equation of H(r) in terms of β(r) and putting in this equation the 4 equations above. Thus, we get:

$$\frac{d\beta}{dr} = 2\left(1-\frac{2m(r)}{r}\right)^{-1} H(r)\left\{-2\pi[5\rho_e + 9P + f(\rho_e + P)] + \frac{3}{r^2} + 2\left(1-\frac{2m(r)}{r}\right)^{-1}\left(4\pi rP + \frac{m(r)}{r^2}\right)^2\right\} + \frac{2\beta(r)}{r}\left(1-\frac{2m(r)}{r}\right)^{-1}\left\{-1 + \frac{m(r)}{r} + 2\pi r^2(\rho_e - P)\right\} \tag{1.5.9}$$

In this equation we take $H(r)=dr^2$ and $\beta(r)=2dr$ as $r \to 0$, where d is a constant that can be chosen as we like because the Love number does not depend on it. The way of calculating the solution is to make the solution in the vacuum, where $T_{\mu\nu} = 0$, and the solution in the matter coincide at r=R. In evaluating the external solution, we consider $\epsilon Y_{20}(\theta, \varphi) = \epsilon_{ij} n^i n^j$. After defining $y=\beta R/H(R)$ and $C=m/R$ as the compactness of the star, k_2 is expressed in the following equation:

$$k_2 = \frac{8}{5} C^5(1-2C)^2[2+2C(y-1)-y]\{2C[6-3y+3C(5y-8)] + 4C^3[13-11y+C(3y-2)+2C^2(1+y)]3(1-2C)^2[2-y+2C(y-1)]In(1-2C)\}^{-1} \tag{1.5.10}$$

So far, we have analyzed the tidal deformability for NS in BNS. Now we are going to study that in the case of BHNS system. For this purpose, Lackey [22] developed an inspiral merger waveform model, the LEA model, for BHNS mergers. In this model the GWs strain for a BHNS system is computed as

$$h_{NSBH}(f, \theta, \Lambda_{NS}) = h_{BBH}(f, \theta)\, A(f, \theta, \Lambda_{NS}) \exp[i\,\Delta\psi(f, \theta, \Lambda_{NS})] \tag{1.5.11}$$

where $h_{BBH}(f, \theta)$ comes from a BBH waveform model. In this equation, f is the frequency of the GWs, $\theta = \{m_{BH}, \chi_{BH}, m_{NS}\}$ where χ_{BH} is the spin of the Black Hole. A(.) is the amplitude factor which changes the amplitude of the GWs strain related to the model for BBH to match its parameters to those of the BHNS model. The factor A, in the inspiral phase, is equal to the unity, but when the tidal deformation acts, A changes depending on the tidal deformability Λ_{NS}. $\Delta\psi$ instead corrects the waveform phasing. In the beginning, when the tidal deformability is negligible, $\Delta\psi$ contains just the PN-corrections to the phase. When instead tidal deformability cannot be neglect $\Delta\psi$ becomes more complex. For this model, some assumptions were made: $\chi_{NS}=0$ (absence of spin for the Neutron Star), 1.2 $M_o \leq m_{NS} \leq 1.45\ M_o$, mass-ratios $q=m_{BH}/m_{NS}$ $2< q <5$, and BH-spins $-0.5\leq \chi_{BH} \leq +0.75$. In the first Lackey's model $h_{BBH}(f, \theta)$ was taken from the SEOBNRv1 model, which is an effective one-body for BBH systems with aligned spins.

The Effective-One-Body model to study BBH systems was introduced by Buonanno and Damour [23] in 1998. In the EOB (Effective-One-Body) the BBH systems, with the first Black Hole with mass m_1 and the second one with mass m_2, can be thought, in the early inspiral phase and when the two black holes differ greatly in mass, as a system with one body, from which the name of the model, with mass $M= m_1 + m_2$ and $S_{KERR}= S_1 + S_2$, where S_1 and S_2 are the spin momenta of the two Black Holes and an effective particle of mass $\mu= m_1 m_2 / (m_1 + m_2)$ and spin $S_*=(m_2/m_1)S_1+ (m_1/m_2)S_2 + \Delta^{(1)}{}_{\sigma^*} + \Delta^{(2)}{}_{\sigma^*}$, where the last two terms are related to the Post-Newtonian spin-orbit terms [23]. The Hamiltonian for the EOB approximation is:

$$(1.5.12)\ H_{EOB}= M \left[1 + 2v \left(\left(\frac{H_{EFF}}{\mu} - 1\right)\right]^{1/2} - M$$

Where $v=\mu/M$ is the deformation parameter and H_{EFF} describes the dynamic of an effective spinning particle of mass μ and spin S_* moving in a Kerr metric spacetime with mass M and spin S_{KERR}. In this Hamiltonian (H_{EFF}) are contained terms of Spin-Orbit and Spin-Spin interactions.

The free parameters of the SEOBNRv1 were calibrated to numerical-relativity simulations of non-spinning BH-BH systems of five different mass ratios, and to BH-BH systems with equal mass and without precession and with $\chi_{BH}=+0.44$. This model, with this calibration, is able to produce inspiral-merger- waveforms for spinning, but non-precessing Black Holes with any mass ratios, and $-1<\chi_{BH}<0.7$.

In calculate the probability of having certain values of Λ_{NS}, we consider another model for BBH from which we obtain the GWs strain for BHNS, the SEOBNRv2 (the SEOBNRv1 is the model adopted in the beginning for the first LEA simulations). The SEOBNRv2 in fact reduces the computational costs, beyond as being more accurate especially in the inspiral phase than SEOBNRv1. The SEOBNRv2, introduced by Taracchini [23], is an extension of the SEOBNRv1. It is a model where Black Holes spins are aligned with the orbital angular momentum L, and where for the GWs signal we consider as dominant $l=|m|=2$ modes. In this case the dimensionless spin component $\chi_i = S_i * L/m_i^2$ cover almost the full range ($-1< \chi_i <0.99$), while for the SEOBNRv1 does not overcome $\chi_i=0.7$. S_i are the spin vectors, L is the orbital angular momentum unit vector, m_i are the Black Holes masses. After defining the symmetric mass-ratio $\eta= m_1 m_2/ (m_1 + m_2)^2$, we can define [24]:

$$(1.5.13)\ \chi=\frac{\chi_{KERR}}{1-2\eta} = \frac{\chi_1+\chi_2}{2}+\frac{1}{2}(\chi_1 - \chi_2)\left[\frac{m_1-m_2}{m_1+m_2}\right]\frac{1}{1-2\eta}$$

Where $\chi_{KERR}= (S_1 + S_2) * L/ M^2$ is the dimensionless spin for the deformed Kerr geometry used in the EOB construction. For the calibration in the SEOBNRv2 were used 8 non-spinning numerical relativity waveforms with q= 1, 1.5, 2, 3, 4, 5, 6, 8 ($q= m_1/ m_2 \geq 1$), plus 19 spinning numerical relativity waveforms.

Coming back to the BHNS merger, for the calculation of the probability of having certain values of Λ_{NS}, we have to consider $\Theta = \{m_{NS}, m_{BH}, \chi_{BH}, \Lambda_{NS}\}$ and we consider the Bayes theorem for which [22]

(1.5.14) $p(\Theta| d_N, H) = p(d_N | \Theta, H)\, p(\Theta, H)/ p(d_N|H)$

where $p(\Theta, H)$ is the prior probability of having the set of values Θ for given H which denotes all the knowledge we have of the system with the exception of Θ. d_N represents instead a set of data for this model, obtained by generating artificial GWs signal using the LEA+ model (the LEA is related to SEOBNRv1 for h_{BBH}, while LEA+ to SEOBNRv2) put in zero noise. $p(d_N | \Theta, H)$ can be written in this way:

(1.5.15) $p(d_N | \Theta, H) = N \exp[-\frac{1}{2} < d_N - h \mid d_N - h>]$

where h is a filter template for Θ and N represents the normalization constant which contains distance, orientation and sky location parameters. $< d_N - h \mid d_N - h>$ can be written as

(1.5.16) $< d_N - h \mid d_N - h> = 4 \,\mathrm{Re}\, [\int_0^\infty$ [(T-Fourier (d_N-h)) (T-Fourier (d_N-h)) $^*/ S_N(|f|)$] df

where T-Fourier means Fourier transform, and $S_N(|f|)$ is the amplitude spectrum of detector noise.

Now we can finally calculate the probability of each parameter of interest (we are interested in Λ_{NS}) by integrating $p(\Theta| d_N, H)$. Thus, we get:

(1.5.17) $p(\alpha| d_N, H) = \int d\Theta_\alpha\, p(\Theta| d_N, H)$

where α indicates the precise parameter whose we want to know the probability, and $d\Theta_\alpha$ indicates the integration over all the parameters except the parameter α ($\Theta_\alpha = \Theta - \alpha$).

We can now use what we have found to show the probability distribution for different values of Λ_{NS}.

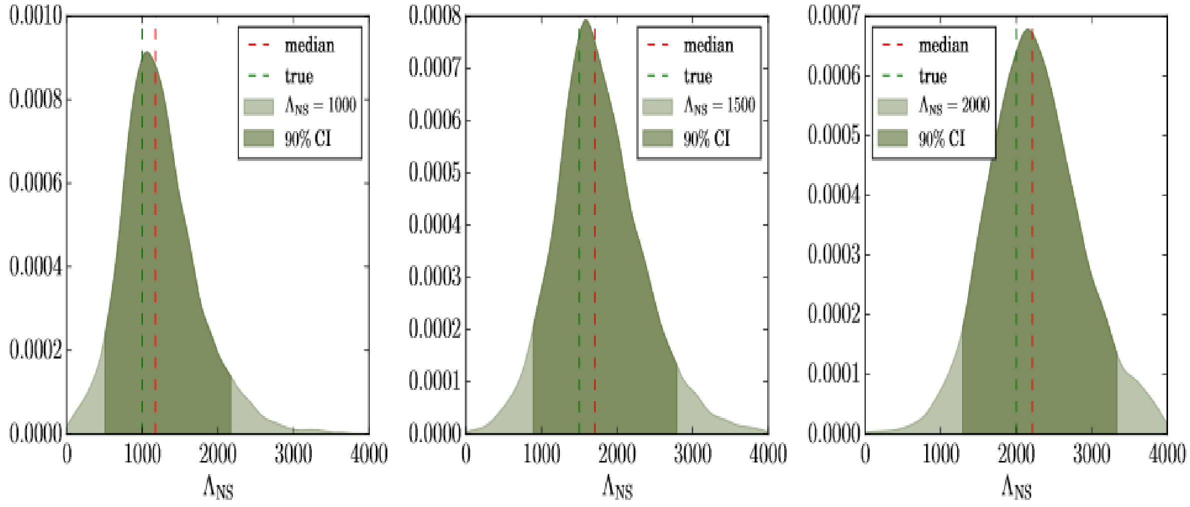

Figure 12: In this figure we see the probability distribution on the y-axis and the tidal deformability of the star on the x-axis. For this calculation, we put $m_{NS} = 1.35\ M_o$, $m_{BH} = 5.4\ M_o$, hence q=4. We also considered $\chi_{BH}=+0.5$ and $\rho=50$, where ρ is the signal-to-noise ratio (SNR). The red-dashed line indicates the median value for Λ_{NS}, while the green-dashed line indicates the true value. As we can see, the confidence level area grows with the tidal deformability. This means that for higher tidal deformability the measurement error decreases. $\rho=50$ was chosen because for small value of ρ, statistical error dominates over systematic error, while for higher values of ρ,like $\rho = 50$, the situation is the opposite and the analysis is more efficient. [22]

CHAPTER 2

NEUTRON, HYBRID AND QUARK STARS AND THEIR STRUCTURE RELATION

2.1 A brief introduction

We know that neutron stars are the result of the collapse of a star with a mass bigger than 8 M_o. [25] The mass of the iron core of the star is bigger than the Chandrasekhar mass and the gravity is big enough to produce the inverse β-decay-process, where protons and electrons combine each other producing neutrons and neutrinos. We also know that this process produces a flux of neutrinos towards the surface of the Proto Neutron Stars (PNS). Some neutrinos leave immediately the Star, the ones which are present on the surface, reducing the gravitational energy, the others, the ones produced in the inner region of the Star, remain trapped in the first seconds after the formation of the PNS.

After the formation of the PNS, we cannot have immediately a crust surrounding the Star, because the temperature is too high (roughly 1 MeV=10^{10} K). After a cooling phase there is the formation of the crust of the Star, and we get a Neutron Star.

This kind of Star can be divided into four layers. The first one is called “atmosphere”, it is just a few centimeters thick, and it is made of atoms of hydrogen and helium. The second layer is the external crust is made of atomic nuclei within degenerate and relativistic electrons. The third layer is the internal crust where there are neutrons in a superfluid state, because the density inside this region overcomes the Neutron drip density, which is roughly $\rho_{DRIP} \approx 4.3\text{x}10^{11}$ g cm^{-3} [26] .After that, we have a lattice of nuclei and free electrons and neutrons. The fourth layer is the nucleus of the Star. This region is mysterious because there are many hypotheses about what we can find inside that. One possibility is the existence of superdense hadronic matter. Another possibility is the existence of exotic matter made of deconfined quarks (up, down, and strange) together with the hadronic matter around that. In this case we would speak of Hybrid Stars. This strange matter of quarks, called SQM, is in the Hybrid Stars the result of the very high pressure due to the collapse of the core of the Star.

Nonetheless, about the SQM, Witten, as we will see, advanced the possibility of having this kind of matter even at zero pressure, as the most stable state in nature. In this case we could have Quark Stars.

2.2 Hybrid Stars

Now we will concentrate on the Hybrid Stars. This kind of Stars are the result of a very high pressure and density. In fact, when pressure due to gravity becomes very high, it is no more possible the existence of neutrons in the inner region of the star and it is more convenient to the star matter to reach a new configuration of stability with SQM. Then, the SQM layer can become bigger till it reaches the surface of the Star. This kind of matter must satisfy this relation:

(2.2.1) $(E/A)_{SQM} < (E/A)_{Fe\ 56}$

Where E is the binding energy, A is the mass number. We consider the ratio between these two quantities for this strange matter and for ^{56}Fe which is the most stable nucleus in nature. In the interior of a Hybrid Star there is such a high density that neutrons are broken, and we can have deconfined up and down quarks. The high density is a necessary requirement to have $(E/A)_{u,\,d}$.

This structure of a Hybrid Star is actually more complex than that of a simple division between a strange-quark-matter inner region and a hadronic-matter outer region. In fact, between those two regions, there is an intermedium region where hadronic and strange matter coexist. This division is always present for massive Neutron Stars. For lower masses, we do not have the pure deconfined quark region, but just the outer hadronic region and the region of coexistence. If the mass of the star is even lower, we have only the hadronic region and the star is purely a Neutron Star. In order to study the transition from hadronic to deconfined-quark matter, we consider the

Gibbs conditions [27], where chemical potentials, temperatures and pressures are equal for hadronic and strange quark matter:

(2.2.2) $\mu_H = \mu_Q = \mu$

$T_H = T_Q = T$

$p_H = p_Q = p$

In the analysis of the transition, it is necessary to deal with the charge conservation, for both the electric and the baryonic charge, Z and B respectively. Now, we can define c=Z/B as the concentration of the conserved charges constant. This quantity is valid as long as there is pure hadronic or strange quark matter. In the phase of transition, we have to distinguish between $c_H = Z_H / B_H$, the concentration of conserved charges for hadronic matter, and $c_Q = Z_Q / B_Q$, the same quantity for strange quark matter. In this case, we can anyway consider these relations of conservation:

(2.2.3) $Z_H + Z_Q = Z$

$B_H + B_Q = B$.

Now, if we consider the Gibbs condition (2.2.2), there will be a unique solution for chemical potentials, if we have a single-component substance. While this is no more valid in the opposite case. In this case the chemical potentials both for hadronic and strange-quark matter satisfy the Gibbs conditions with different values depending on the portion of the hadronic or the strange-quark matter. This fact produces the absence of a constant-pressure region in a gravitating body in hydrostatic equilibrium. For this reason, it is interesting to see how the density profile changes with the radius of the star both in the case of single and multicomponent substance in the phase transition from hadronic to strange-quark matter.

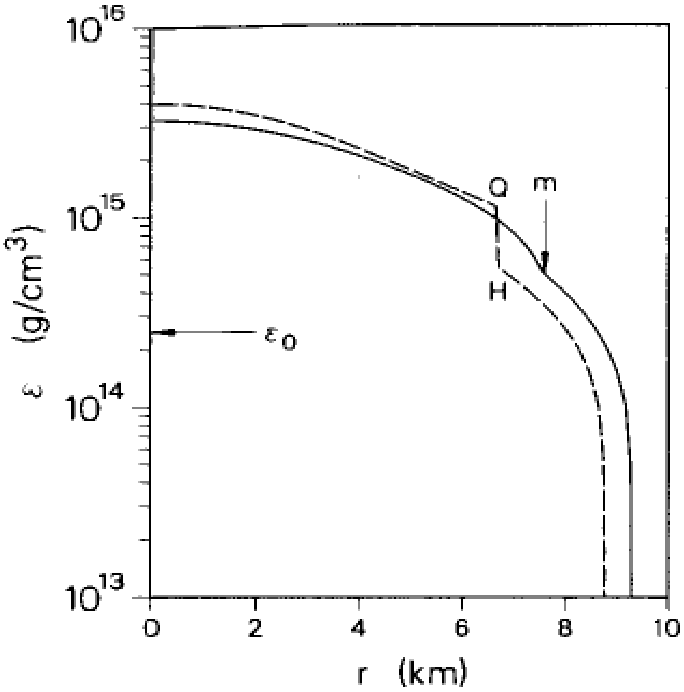

Figure 13: In this image we can see the profile of the density of the Star respect to its radius. The dashed line represents the relation if we have the single component situation, the continuous line represents the relation for the multicomponent situation. The discontinuity between the point H and Q indicates the phase transition, while the part of the graph below the point H indicates the presence of the hadronic matter and the part of the graph above Q indicates the presence of the strange-quark matter. [27]

The discontinuity between H and Q in figure 13 can be also seen in the following graph which represents the relation between the pressure and the density for the case of single-component substance.

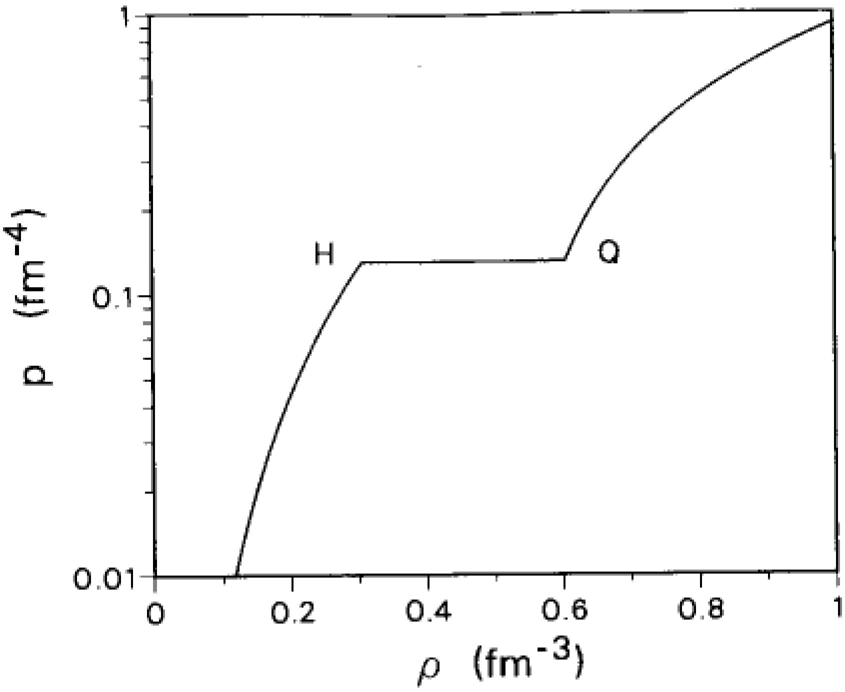

Figure 14:In this figure we see the relation between the pressure and the density for a single-component substance during the phase transition from hadronic and strange-quark matter. The behavior is similar to that of the phase transition of the water. [27]

We already know that the ordinary matter is made of up and down quarks, but also the strange quarks are possible. Charm, Bottom and Top quarks cannot be produced because too high energy is required and for higher densities than those necessary to produce a deconfined-quark-core, we have a collapse to Black Hole. To produce strange quarks, which are heavier than up and down quarks, hyperons must be produced. Hyperons are hadrons made of s-quark, besides u, d-quarks. If the pressure increases beyond a certain level, hyperons are quite stable (in the opposite case they decay to ordinary nucleons). For this level of pressure, the baryonic chemical potential μ_B gets very small, but it becomes even smaller if deconfined s-quarks are produced by the conversion from the d-quarks via weak-interaction process, while the conversion from baryons to deconfined quarks happens via strong-interaction process. We can see better the situation through the following image:

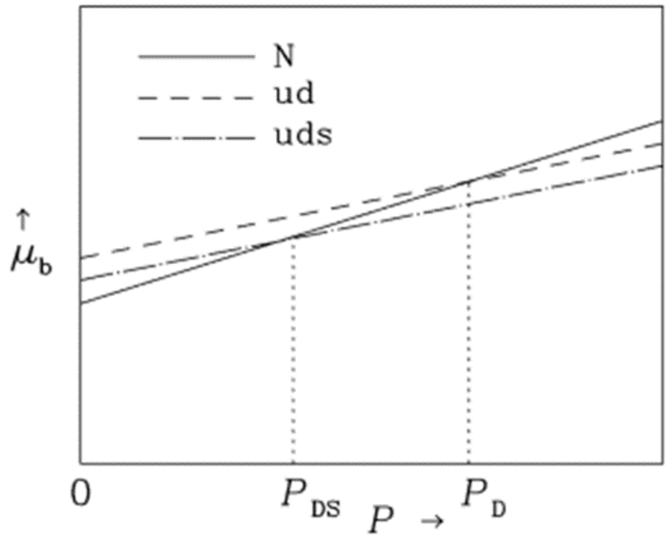

Figure 15: In this figure we see the relation between the pressure and the chemical potential for the baryonic matter (continuous line), the u, d-quark matter (dashed line without dots), the u, d, s-quark matter (dashed line with dots). P_D is the minimum pressure for the conversion of the hadronic matter to the SQM without s-quarks and P_{DS} is the minimum pressure for the conversion to the SQM with s-quarks. [28]

2.3 The Witten's hypothesis about the Quark Stars and theoretical models for SQM at zero pressure

We have already seen how a big increase of the pressure and the density inside a Neutron Star could turn hadronic matter into SQM, but Witten considered the possibility of production of stable uds matter even at P=0. In fact, for heavy droplets of uds matter, whose baryon numbers is far bigger than 10 (A>>10), in order to avoid a drop of stability due to the contribution of the surface, the energy per baryon is lower than that of ^{56}Fe. Moreover, the ordinary nuclei are metastable with respect to the transition to SQM. This is not in conflict with the experimental data because the lifetime of the ^{56}Fe, and in general of the metastable nuclei, is very long and, in order to get SQM, is necessary a simultaneous conversion of A≈10^2 of d-quarks into s-quarks. A process like this would require time of the order of 10^{100} years, while the age of the universe is 1.4x10^{10} year. Even if Witten is the most famous supporter of the possibility of the conversion of hadronic matter to SQM, he was not the first physicist to have considered that. In fact, in 1971 Bodmer [28] took in consideration the possibility that the atomic nuclei were a metastable state of a more general state of baryon number A. He assumed that for a quite big A there is a "collapsed nucleus" C_A with smaller radius and higher density than a "normal nucleus" N_A. He supposed that the radius of C_A was 1/3 of that of N_A and its density roughly 30 times higher. This bounder nucleus would be the true ground state of the matter. Bodmer considered three models of C_A: two of them are related to abnormal state of nuclear and hyperonic matter with huge binding energy, the third one is related to uds matter with a small positive electric charge. These three models are not in conflict with experimental data because the nuclei N_A have a lifetime much longer than the age of universe. The first two models considered a kind of matter which is similar to the “abnormal matter” theorized by Lee and Wick in 1974. In this “abnormal state” of nuclear matter nucleons become almost massless. Eight years after the Bodmer’s formulation of his model, the possibility of the existence of stable “nuclei” made of deconfined quarks was studied through the Bag Model by Chin and Kerman [28] in 1979. This model cannot be considered valid because the uds matter would not be absolutely stable, but they would decay to nuclei matter. After this one, other theoretical models were studied but without any success till 1984, when Witten [28] theorized his model for SQM at zero external pressure due to gravity. Witten proposed the idea based on the existence of “quark nuggets” made of equal number of up, down and strange quarks. These nuggets would have been formed during the phase of hadronization in the early universe 10^{-5} s after the Big Bang. The most stable “quark nuggets” could be the constituents of Dark Matter. By using the MIT Bag Model, Witten proved that these nuggets are the most stable state of matter at zero pressure. In the simplest form of the MIT Bag model, quarks are assumed to be massless, non-interacting and confined inside a sort of bag of QCD vacuum (where quarks can move freely). The confinement of the quarks is represented by the quantity B which is the difference between the energy density between the hadronic and the SQM vacua. Out of the “bag” quarks cannot be present in this model otherwise their mass would be infinite. The total energy density of the quarks inside the bag is the sum of B, the kinetic component and, in a more general situation, the interaction energy density obtained by QCD perturbations. Now, what is the MIT Bag model in details? We consider the simplest case first, where there is no interaction between quarks and we also consider the condition of electric charge neutrality. In this situation $n_u = n_d = n_s$ and $n_e = 0$, where n_u, n_d, n_s and n_e are the number density of u-quarks, d-quarks, s-quarks and electrons respectively. Under these conditions, the baryon number density $n_b = n_u$. The energy density can be expressed as

(2.3.1) $\epsilon = \epsilon_{KIN} + B$

Where ϵ is the total energy density and ϵ_{KIN} is the kinetic energy density. Considering the ultrarelativistic nature of this Fermi gas of deconfined quarks with a flavor-color symmetry of our system with 18 degrees of freedom ($3_{FLAVOR} \times 3_{COLOR} \times 2_{SPIN} = 18$), we can write down

(2.3.2) $\epsilon_{KIN} = b\, n_b^{4/3}$

With $b = \frac{9}{4} \pi^{2/3} \hbar c = 952.37$ MeV fm

At this point we can define the pressure as

(2.3.3) $P = n_b^2 \frac{d}{dn_b}\left(\frac{\varepsilon}{n_b}\right) = \frac{1}{3} b\, n_b^{4/3} - B$

As we can see the pressure is the sum of two components: the positive one, related to the kinetic energy of quarks and the negative one, related to the vacuum contribution. The interesting feature of this equation is the implication of a self-bound state of quarks at zero pressure. When the pressure is equal to zero, the baryon number density is:

(2.3.4) $n_{b,s} = \left(\frac{3B}{b}\right)^{3/4} = 0.28665\ (B_{60})^{3/4}\ \mathrm{fm}^{-3}$

Where $B_{60} = \frac{B}{60}$ MeV fm^{-3}

The lower index s indicate that we are considering the baryonic density on the surface of an object which is made of u-d-s quarks.

Then, we can calculate the energy per baryonic number unit when we have no pressure, which is:

(2.3.5) $E = 4\ \left(\frac{b}{3}\right)^{3/4} B^{1/4} = 837.26\ (B_{60})^{1/4}$ MeV

And the mass density too, which is:

(2.3.6) $\rho_S = 4B/c^2 = 4.2785 \times 10^{14}\ B_{60}$ g cm^{-3}

It is interesting to consider the situation of absence of strange quarks. In this situation, we would have $n'_S = 0 = n'_e$ and $n'_d = 2n'_u = 2\ n'_b$

In this case the following equations are valid:

(2.3.7) $b'/b = 1.1733$, $E'/E = 1.1273$ at $P=0$ and $\rho'_S = \rho_S$

As we can see the uds deconfined matter is more stable of the ud one because it minimizes the energy per baryonic number unit. This means that if we have u-d deconfined matter, there will be a decay process via this reaction: u+d-> u+s, which will turn down quarks into strange quarks. This is exactly the opposite of what happens for baryonic matter where are the hyperons, made of bound quarks, to turn into nucleons. This fact is a consequence of the Pauli exclusion principle, because of which we cannot have two or more fermions (quarks are fermions) with the same quantum numbers. Thus, if there is a quite big number of quarks concentrated together, it is convenient, because of this principle, in order to minimize their energy, the production of a new type of quark: the strange quark.

The only thing which misses is the determination of the value of B. Here we do not have a unique value but a range of value which depends on the energy at rest of the strange quark. If we consider the validity of the hypothesis of strange matter and, at the same time, the fact that neutrons cannot decay to u-d quark matter, we can express for B_{60} the following inequality: $0.982 < B_{60} < 1.53$ which corresponds to a value of B between roughly 60 and roughly 90 MeV fm^{-3}. We can see better the relation between

B and the energy at rest of the strange quark ($m_S c^2$) both in the case of non-interacting deconfined quarks ($\alpha_S = 0$) and in the case of interacting deconfined quarks ($\alpha_S > 0$) through these graphs:

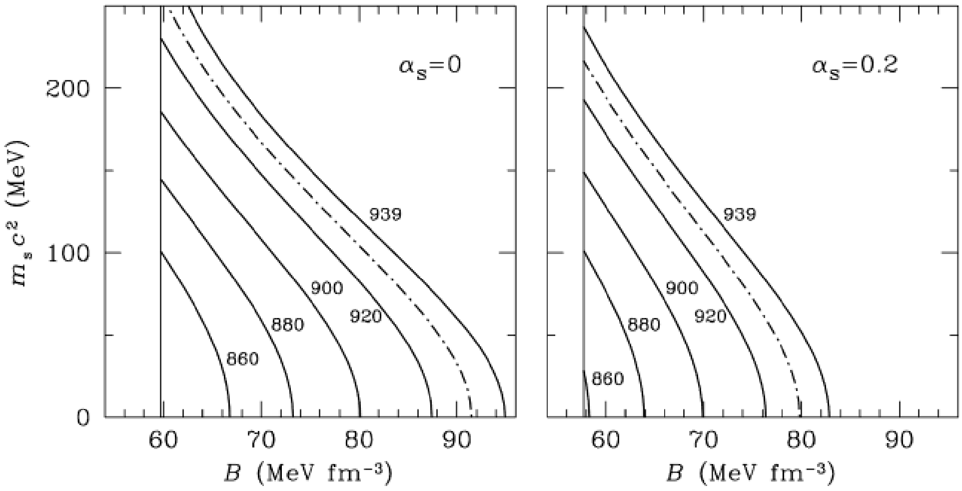

Figure 16: In this figure we can see the relation between the B-value and the energy of s-quarks at rest. In the left panel, we see this relation under the hypothesis of non-interacting deconfined quarks, with the α_S, the coupling constant for strong interactions, equal to zero. In the right panel, we see the same relation under strong interaction with a low value of the coupling constant which increases if the quark energy decreases. [28]

Now, we are going to prove that the Witten's hypothesis is meaningful. In order to do that, we have to analyze the degenerate and ultrarelativistic gas made of these quarks, for which we have to calculate their pression, their energy density and baryonic density in natural units:

(2.3.8) $p = -B + [1/(4\pi^2)] \sum_f \mu_f^4$

(2.3.9) $\epsilon = B + [3/(4\pi^2)] \sum_f \mu_f^4$

(2.3.10) $n = [1/(3\pi^2)] \sum_f \mu_f^3$

Where μ_f is the chemical potential of the quark of flavor f, and B is the constant pressure which maintains the hadrons gathered in a sort of "bag". To simplify our analysis, we assume the neutrality of the star, by neglecting the presence of neutrinos and, in a more general way, charged leptons. Under this assumption

(2.3.11) $q = [1/(3\pi^2)] \sum_f Q_f \mu_f^3 = 0$

Considering this condition, we can write down this relation for the chemical potentials of the quarks:

(2.3.12) $\mu_d = 2^{1/3} \mu_u = \mu_2$

Considering the result of (2.2.4), we obtain

(2.3.13) $n= \mu_2{}^3/\pi^2$

For the reason why we are considering light quarks, we can put p=0 and we have $\epsilon_{SUP}=4B$ and B will be:

(2.3.14) $B= [1/(4\pi^2)] \sum_f \mu_f{}^4$

By using this equation, we will obtain:

(2.3.15) $\mu_2 = [(4\pi^2)/(1+2^{4/3})]^{1/4} B^{1/4}$

Now, we can calculate $(E/A)_{u,\,d}$:

(2.3.16) $(E/A)_{u,\,d} = (4B\pi^2)/\mu_2{}^3 = (2\pi)^{1/2}(1+2^{4/3})^{3/4} B^{1/4} \approx 934$ MeV

Where we considered $B^{1/4}=145$ MeV.

This value of $B^{1/4}$ is the minimum value for which the binding energy of the up and down free quarks is bigger than the one of the ^{56}Fe. For lowest values up and down free quarks are more stable than ordinary matter. In the analysis of the SQM, we consider the chemical potential of up, down, strange quarks all in equilibrium: $\mu_3 = \mu_u = \mu_d = \mu_s$, with

(2.3.17) $n= \mu_3{}^3/\pi^2$

Considering (2.2.8), we can calculate μ_3:

(2.3.18) $\mu_3 = (4\pi^2/3)^{1/4} B^{1/4}$

In the same way as before, we now obtain $(E/A)_{SQM}$:

(2.3.19) $(E/A)_{SQM} = (4B\pi^2)/\mu_3{}^3 \approx 829$ MeV

In order to see better what we have done, let us look this picture:

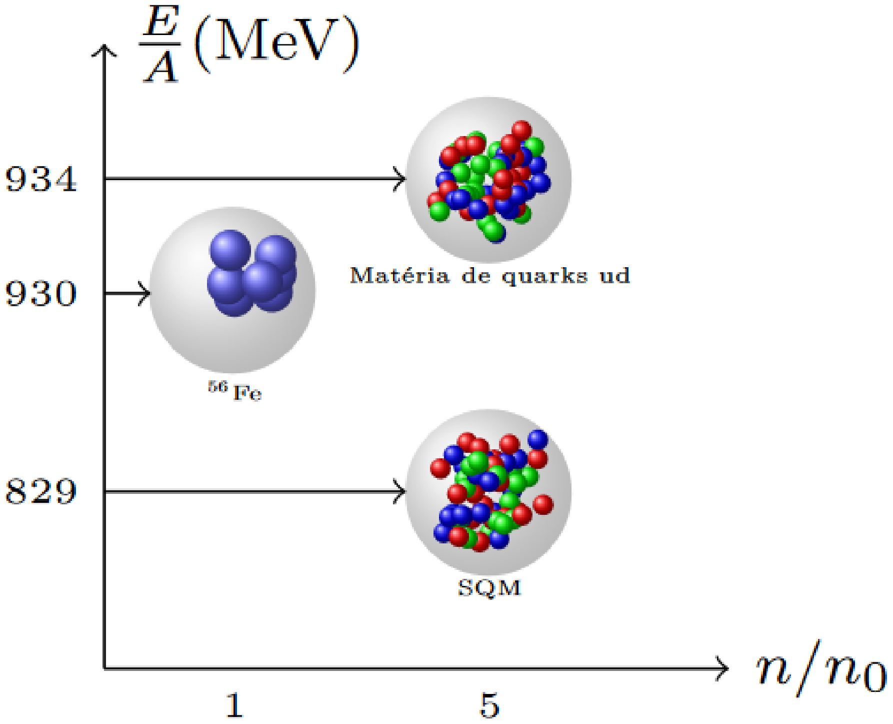

Figure 17: In this picture we see the ratio between the binding energy and the mass number for quark matter,^{56} *Fe, and Strange Quark Matter respect to the baryonic number density divided by* $n_0 = 0.16$ fm^{-3}. *[25]*

After proving the validity of the Witten's hypothesis, it is interesting to see how the baryonic chemical potential change with the pressure in a Quark Star, which exists because of the Witten's hypothesis, considering the three cases of the baryonic, the u-d, and the u-d-s matter, as just done previously for Hybrid Stars (figure 15). Let us see the comparison between the two graphs:

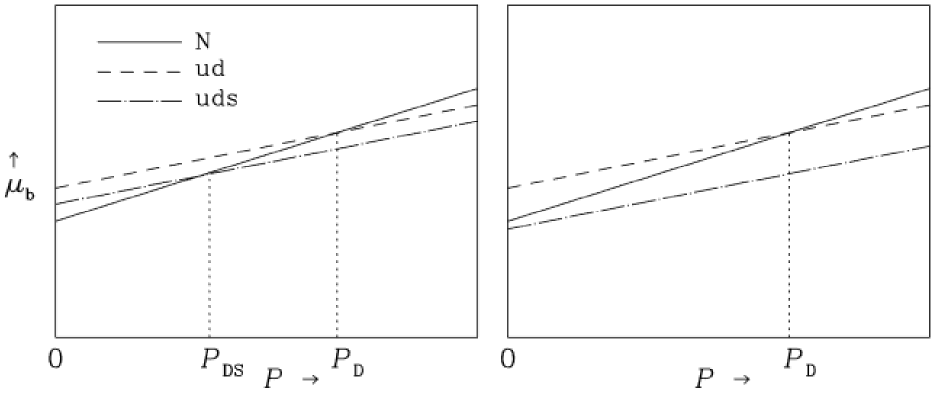

Figure 18: As we can see the left graph is that of figure 15, related to Hybrid Stars, the right one is that referred to the Quark Stars under the Witten's Hypothesis. [28]

2.4 *Structural Difference among Bare Strange Stars, Strange Stars with crust and Neutron Stars*

Now we are going to see the main differences between bare Strange Stars, or pure Quark Stars and Strange Stars with crust, or Hybrid Stars. Bare Stars are built only of SQM. The surface density of this kind of Stars is equal to SQM density at zero pressure. For sake of comparison, this density is 14 times higher than those of Neutron Stars. For this type of stars, we have a very peculiar Mass-Radius relation. For masses higher than 1 M o, the radius changes very slightly wit mass. Nonetheless, for lower masses the Radius decreases with the Mass. If M< 0.3M o, we have $R \propto M^{1/3}$. The MIT Bag Model is able to explain this fact. In fact, if the Stars is light enough (under 0.3Mo) the gravitational attraction is negligible respect to the pressure produced by the SQM. What we get is a very stiff Star whose density is almost constant. The following graph shows the Mass-Radius relation both for bare Strange Stars and Strange Stars with crust that we will see.

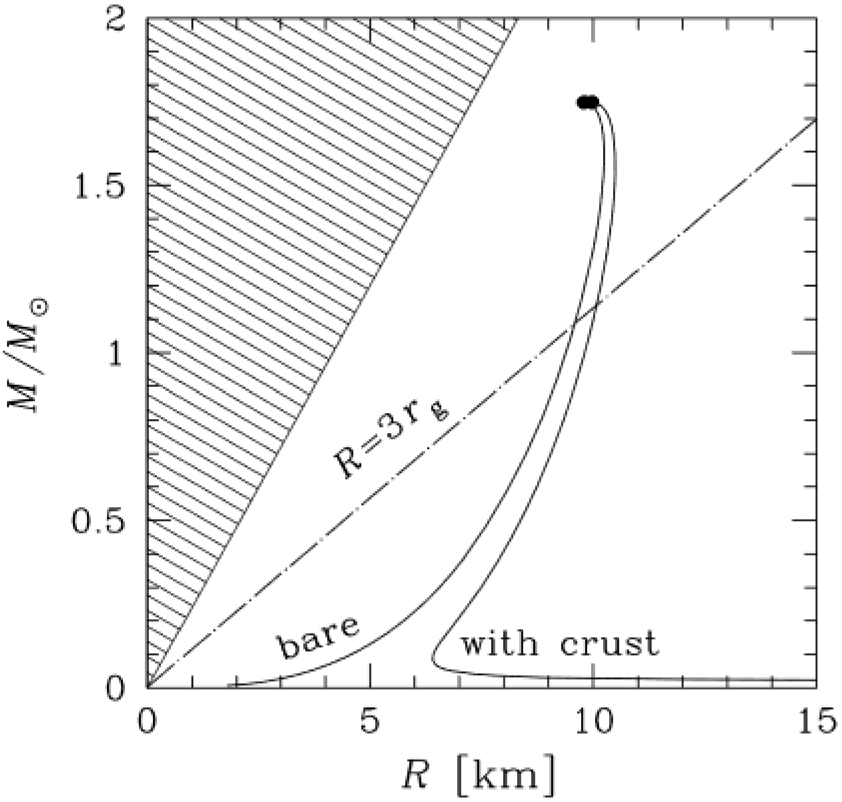

Figure 19: In this figure we see the relation between the mass of a Quark Star divided by the solar mass on the y-axis and the radius on the x-axis, both with and without the crust around the Star. Of course, this is valid if we assume the MIT Bag Model is true. In this case the following assumptions have been made: $m_S c^2 = 200$ MeV, $\alpha_S = 0.2$, $B = 60$ MeV fm^{-3}. The dash- and dot- line indicates the radius of the most stable circular orbit. [28]

Beyond the radius, also another quantity of these Stars must be considered in relation with the mass: the redshift on the surface, z_{SURF}. It is interesting to see how this quantity changes with the mass of the Star. These Stars are more compact than Neutron Stars. Hence, the redshift is higher for a Quark

Star than for a Neutron Star of the same mass. For M=1.4 M o, the surface redshift is roughly 20% higher than a Neutron Star of the same mass, for M= M o it is roughly of 30%, if M= 0.5 M o, it is even of 100%. As we can see, the surface redshift difference between a Quark and a Neutron Star grows if the mass decreases. The following graph can show the situation better.

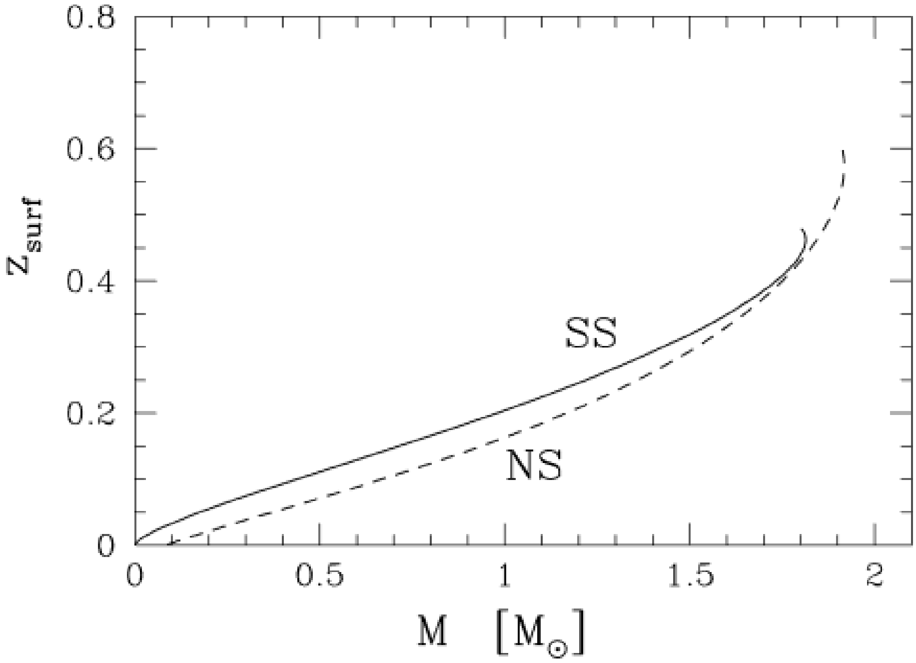

Figure 20: In this figure we can see how changes the redshift with the mass, both for Neutron Stars (dashed line) and Quark Stars (continuous line). The SS means Strange Stars whose behavior is indicated by the continuous line. The NS means Neutron Stars whose behavior is indicate by the dashed line. [28]

Now we are going to deal with the Strange Stars with the crust. These Stars ones, unlike the Bare ones, have a crust made of nuclei absorbed in a sea of electrons. The crust could be formed by accretion, from a binary system, of which this Star is a part, or from the interstellar medium, or otherwise it could be the residual of the transformation of a Neutron Stars to a Strange one. The core could coexist with the crust if we consider the condition of the absence of neutrons in the crust because the neutrons must be turned all into SQM. Furthermore, in order to prevent the nuclei from being absorbed by the SQM the presence of a Coulomb barrier is necessary, i.e. there must be a strong electric field between the nuclei and the SQM. Going into more detail, we can express the electrostatic potential in the nearby of the crust in the approximation of a flatness, because in this case the curvature is negligible. We can call V(z) our potential with z as vertical axis with z<0 which indicates the interior of the Star. The boundary conditions are V(z) -> V_q for z-> -∞ , where V_q is the potential of the quarks on the "surface" of the core, and V(z) -> V_{CR} for z-> +∞ , where V_{CR} indicates the potential on the nuclei crust (in the case of a pure Quark Star, V(z) -> 0 for z-> +∞) . Alcock [28] in 1986 estimated a potential difference $\Delta V = V_q - V_{CR} \geq 10$ MeV /| e |, where e is the electric charge of the electrons.

About the mass of the crust, there is a relation between this mass and the mass of the Star. For $M>M_{o}$, the maximum mass of the crust is roughly $10^{-5}\,M_{o}$. If $M> M_{o}$, the radius of a Hybrid Star is bigger than that of a pure Quark Star. If $M=1.4\,M_{o}$, the crust of the Star cannot be larger than roughly 300 m, when the radius is roundly 10 Km. Under this condition, the mass and the thickness of the crust decrease when the mass of the Star increases, because the growth of the mass means a growth of the density which turns hadronic matter into SQM. The core of the Star is self-bound via the QCD forces, while the crust is not self-bound but bound to the core by the gravitational pull.

Now, what about the minimum mass of a Hybrid Star? If $\rho_{B}=\rho_{ND}$, where ρ_{B} is the density of the bottom of the crust and ρ_{ND} is the density of the neutron-drip, which is the maximum density for nuclei with all the neutrons they are able to pack inside ($\rho_{ND} = 4\times10^{11}$ g cm^{-3}), $M_{MIN} \cong 0.02\,M_{o}$. To make a comparison the minimum mass of a Neutron Star is 1 M_{o}. If $\rho_{B}< \rho_{ND}$, the mass is even smaller. If the mass is very small, the configuration is very unstable.

An interesting topic is the fact that, if we have a small tension on the surface of the crust, there is the possibility of the formation of an exotic crust made of strangelets of quarks inside in a gas of electrons.

2.5 Relation between Love Number and mass for Neutron and Quark Star

Now we have to consider different types of EOS for neutron stars. These EOS are different because they are based on different composition of the stars .7 EOS are related to classical neutron stars, 8 to neutron stars with pions, hyperons and quarks, 3 related to quark stars.

We can see now two graphs (figure 21) about the Love number relation with compactness (the first graph) and with mass expressed in terms of solar masses (the second graph) for each of these 18 EOS equations.

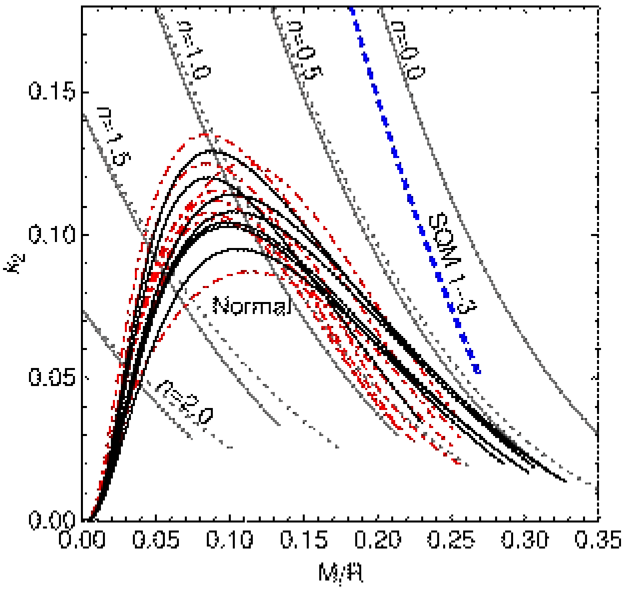

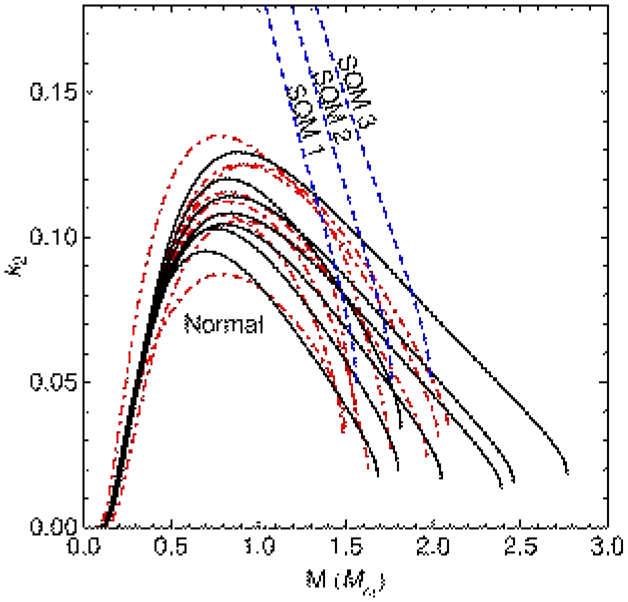

Figure 21: In the graph above we have plotted the relation between the Love Number and the compactness (M/R) for different Eos, in the graph below, we have the relation between the Love number and the mass of the Star expressed in solar masses [21].

.

In the first panel the grey solid lines refer to the polytropic equation of pressure ($P=K\rho^{1+1/n}$, where ρ is the rest mass density), the grey dotted lines are instead related to the polytropic equation of pressure ($P=K\,\rho_e{}^{1+1/n}$). Both curves are different for each index n. The black curves refer to the relation between the Love number and compactness for the 7 EOS of classical neutron stars, the red ones are instead related to the 8 EOS of neutron stars having pions, hyperons and quarks. The blue dotted line is referred to the three quark stars (actually it is an overlap of the curves of these 3 quark stars).

In the second graph there is no more the compactness on the x-axis, but the mass expressed in solar masses. The Love number in this case depends only on K, the polytropic constant. This is why polytropic EOS are not shown. Nonetheless the legend is the same as the first graph.

What can we learn from these two graphs?

Considering k_2 as the ease with which the neutron star matter is deformed, we can see that, if compactness is not too small, the Love number, the ease of deformability, decreases with compactness because the biggest amount of mass would be concentrated around the center of the star and, because of a strong gravitational force, tidal deformation is not efficient and the star is stiff. The Love number is zero when M/R=0.5, when the compactness is that of a Schwarzschild black hole and this is true for any value of y in the k_2 formula. For higher compactness normal matter EOS are similar to polytropes in the behavior. But if compactness is small the softer crust becomes the biggest part of the star and gravitational force is able to condense it around the center of the star, making that less deformable.

Another interesting point deals with the polytropic index which is lower for higher Love numbers. In fact, if the index n is higher, the matter is softer (just think about the energy inside relativistic matter which is higher than the non-relativistic one and then less stiff). If the matter is softer it is easier for gravity to condense it making the star stiff. For n=0, density is constant, and the Love number has its highest value. We have analytic solutions just for the case n=0 and n=1. In order to get more details about these two situations, it is better to rewrite the equation (1.5.4), as it was done by Prakash and Lattimer [29] in more compact form as

(2.5.1) $ry'(r) + y(r)^2 + y(r)\, e^{\Lambda(r)}[1 + 4\pi\,(p(r) - \rho_e(r))] + r^2 Q(r) = 0$

where

(2.5.2) $y'(r) = rH'(r)/H(r)$

(2.5.3) $Q(r) = 4\pi e^{\Lambda(r)}\left[5\rho_e(r) + 9p(r) + \frac{\rho_e(r)+p(r)}{c_s^2(r)}\right] - \frac{6}{r^2}e^{\Lambda(r)} - \left(\nu(\dot{r})\right)^2$

where

(2.5.4) $c_s^2(r) = dP/d\rho_e$ is the speed of sound and

(2.5.5) $\nu'(r) = 2\, e^{\Lambda(r)}\,(m(r) + 4\pi p(r) r^3)\frac{1}{r}$

For n=0 we have an incompressible fluid with infinite speed of sound and y(r) =2 as solution for all the interior of the star, while in the other case we have this solution just in the center as boundary condition. For the surface the situation is different because we have a discontinuity which can be expressed as

(2.5.6) $y(r_d + \varepsilon) = y(r_d - \varepsilon) - \frac{\rho_e(r_d+\varepsilon) - \rho_e(r_d-\varepsilon)}{\frac{m(r_d)}{4\pi r_d^3}} = y(r_d - \varepsilon) - \frac{3\Delta p}{\rho_M}$

where $\Delta p = \rho(p_d + \epsilon) - \rho(p_d - \epsilon)$ and $\rho_M = \frac{1}{3}\frac{m(r_d)}{4\pi r_d^3}$ with ϵ -> 0.

In the case of n=0,

(2.5.7) $y(R) = y(r_-) - 4\pi R^3 \frac{\rho}{M} = y(r_-) - 3 = -1$

and $k_2 = 3/4$.

For n=1 the solution of the (1.6.16) is

(2.5.8) $y(r) = \frac{\pi r}{R}\frac{J_{3/2}(\frac{\pi r}{R})}{J_{5/2}(\frac{\pi r}{R})} - 3$

with $y(R) = (\pi^2 - 9)/3$, $k_2 = (15 - \pi^2)/ 2 \pi^2$ and J_l are the Bessel functions.

Dealing with quark stars, we can state that, for equal compactness and mass, deformability is bigger. Nonetheless, a difference like this one is very difficult to detect, and this means that it is difficult, evaluating just tidal deformation, to discriminate neutron stars and quark stars.

2.6 Breaking point of the crust in Horowitz's model

We have just mentioned the role of the crust in Neutron Stars to investigate their behavior. Now, we are dealing with a theoretical model elaborated by Horowitz [29] to explain how the crust of binary neutron stars is broken by tidal force. If we know the tidal deformability of the two neutron stars (λ_1 and λ_2), we can calculate a weighted average:

$$(2.6.1) \quad \lambda_M = \frac{1}{26} [(11m_2 + M) \frac{\lambda_1}{m_1} + (11m_1 + M) \frac{\lambda_2}{m_2}]$$

where $M= m_1 + m_2$.

If $m_1 = m_2$, $\lambda_M = \lambda_1 = \lambda_2$. If $m_2 =0.5\, m_1$, $\lambda_M \approx \frac{40}{26} \lambda_1$. Considering that it is very unlikely to have a NS mass bigger than 2 M_o, this last case is extreme.

In Horowitz's model the crust of the stars was assumed to be liquid in the evaluation of the Love number. This is true if we assume that the tidal stress is so big to make the crust liquid. In order to find out the breaking point of the crust, we have to consider the quadrupole moment $Q_{22} = \lambda\, \epsilon_{22} \approx (3/2)^{1/2} \lambda\, M/D^3$, where D is the distance between the stars and for sake of simplicity Horowitz put $m_1 = m_2$. Now, considering Kepler's third law, we can express $\omega^2 \approx M/ D^3$, where ω is the orbital angular velocity. Now, the frequency f of the gravitational waves produced by these stars in their inspiral movement is twice the orbital frequency:

$$(2.6.2)\ f= \frac{2\omega}{2\pi} \approx \frac{1}{\pi} (\frac{Q_{22}}{\lambda})^{1/2} (\frac{2}{3})^{1/4}$$

Thus, considering a strain coefficient which is $\sigma=0.01$, Horowitz estimated a quadrupole coefficient $Q_{22\,max} =10^{40}$ g cm^2. Considering this value and a value for $\lambda =2x10^{36}$ g cm^2 s^2. This value of λ is related to a star of mass 1 M_o, in the Postnikov–Prakash-Lattimer model [29].Therefore the break-point frequency is:

$$(2.6.3)\ f_{br} \approx (\frac{2}{3})^{1/4} \frac{1}{\pi} (\frac{10^{40} gcm^2}{2x10^{36} gcm^2 s^2})^{1/2} \approx 20 \text{ Hz}$$

Coming back to the Keplerian formula, we can state that 20 Hz of frequency mean that the distance between the NS is 400 km. Thus, if $D<D_{br}$ or $f> f_{br}$, the quadrupole moment is strong enough to make the crust liquid. The Horowitz's model could be considered as an assurance of the liquid state of the crust, knowing that frequencies that can be detected by Ligo are between 100Hz and 1000Hz. Now we are looking at a graph about Horowitz's model studied by Postnikov, Prakash and Lattimer.

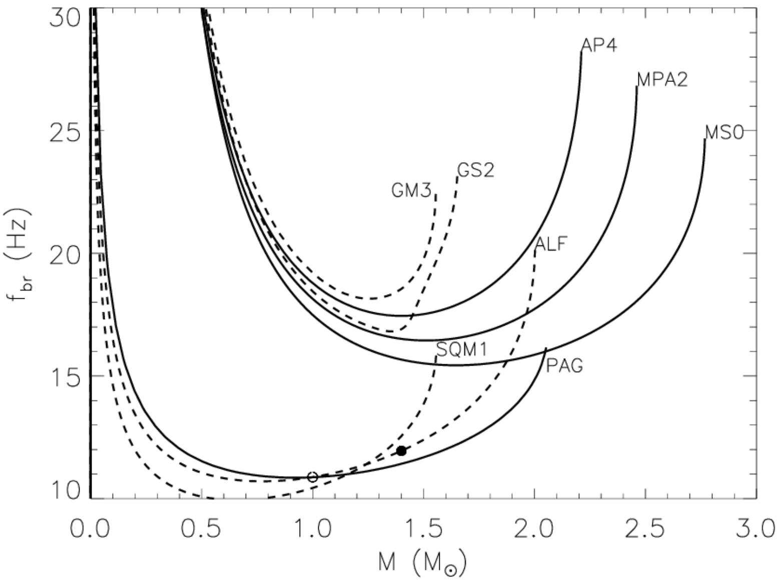

Figure 22: In this plot we have the relation between the breaking point frequency and the mass of the merger for different Eos (in the hypothesis of stars with equal masses). [29]

This graph shows the relation between the breaking point frequency and the mass for different stars models EOS (SQM1, ALF and PAG are related to quark stars, the others are related to classical neutron stars made of protons and neutrons).

2.7 Mass-Radius relation in Quark and Neutron Stars

For classical neutron stars, in order to obtain a relation between mass and radius, we have to solve TOV equation for pressure and the equation for mass distribution already seen before. Then, for each value of central pressure using a Table function, we obtain a graph which is:

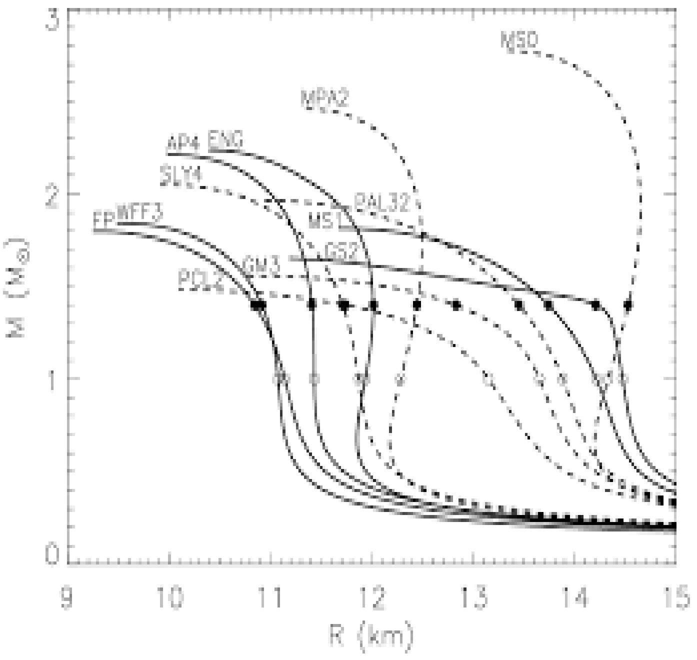

Figure 23: In this plot we have the relation between the mass of a neutron star (expressed in solar masses) and its radius (expressed in km) for different Eos. [29]

For quark stars, the subject has been already treated. But we can see a graph of the Mass-Radius relation for this type of Stars with different EOS.

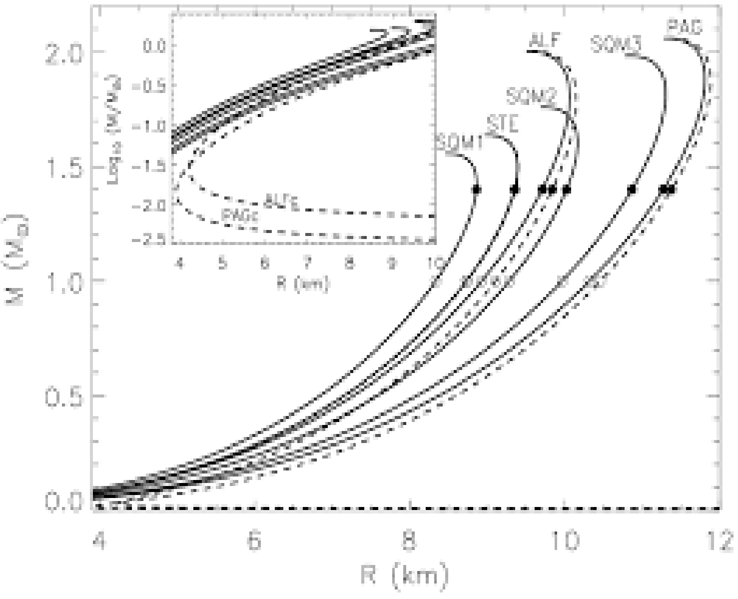

Figure 24: In this plot we have the relation between the mass of a quark star (expressed in solar masses) and its radius (expressed in km) for different Eos. [29]

As we can see, for a hadronic star mass drop with radius is due to the existence of a crust which, being soft, is condensed around the center by gravity reducing the radius of the star. For a quark star the situation is different, because there is no crust and matter, being made of bound states of quarks and so much more difficult to compress, is very hard and consequently bigger is the mass bigger is the radius.

CHAPTER 3

STUDY OF BINARY NEUTRON STARS SYSTEMS

SUB- CHAPTER 3A: Study of the stability of the merger from collapse to Black Hole for Binary Systems

3A.1 Study of the rotating remnant and its stability

In order to find out the threshold mass between black hole and the other outcomes of the merger, we will concentrate on Bauswein's work; Bauswein [30] elaborated a numerical simulation starting from this metric to describe differentially rotating neutron stars, neutron stars with a different angular speed for the envelope and the core:

(3A.1.1) $ds^2 = - e^{2v} dt^2 + e^{2\psi} (d\varphi - \omega dt)^2 + e^{2\mu} (dr^2 + r^2 d\theta^2)$

where μ, v, ψ depends only on r and θ.

In this metric we can define as the angular momentum of the system at the time of the merger in this way, considering the moderately stiff DD2 EOS.

(3A.1.2) $J_{MERGER} = (a M_{TOT} - b)$

with a=4.041 and b=4.658.

Stiffer neutron stars have larger radius and a larger J_{MERGER}, because stars merge earlier than more compact stars. Therefore, less angular momentum is lost during the inspiral phase. The positive aspect of this formula is that it depends slightly on the EOS: the angular momentum changes at most for the 5% of its value if the EOS changes. Now we can show the relation between mass and the maximum energy density of the neutron stars for different NS.

Bauswein and Stergioulas used the RNS code to elaborate differentially rotating equilibrium models to study this relation.

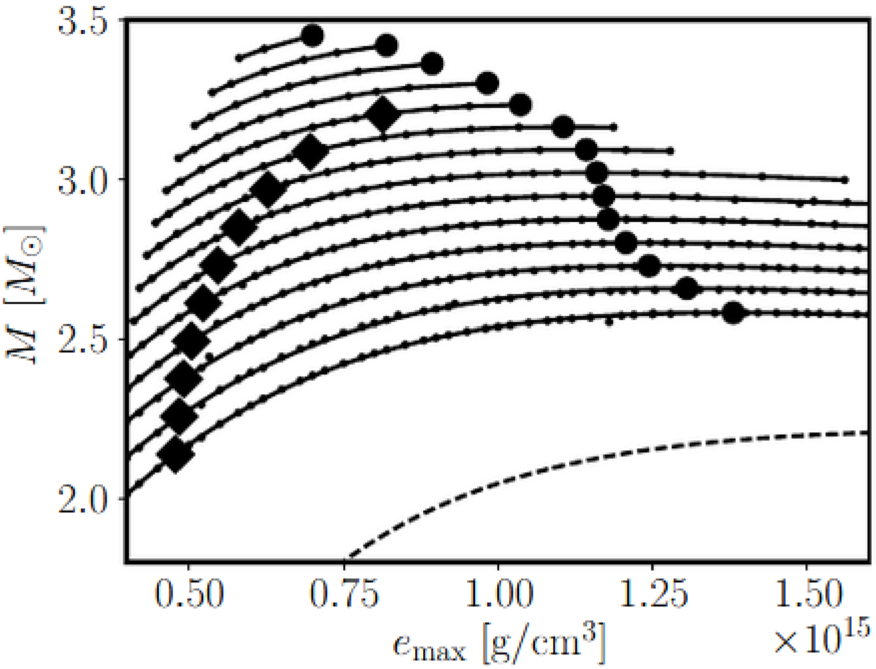

Figure 25: In this figure we have plotted the relation between the mass of the merger and its maximum angular momentum [30]

In figure 25, the dashed line below corresponds to the non- rotating limit, while the diamonds on the left correspond to the model for which the empirical formula of the angular momentum for the merger phase is valid. The solid lines represent the relation between mass and maximum energy density for J-values from J=4 to J=10.5 (J=4,4.5,5,5.5,…..,10.5) in geometrical units. The filled circles mark the turning point, the point of maximum value of the mass with the growth of the maximum energy density. After this point with the increasing maximum energy density, we are in an unstable region because the mass starts dropping. For values of J higher than 8.5, we have a stable configuration around the turning point. The situation gives us the possibility of considering the maximum mass of stability without caring too much of the exact value of the mass because of the slight slope, obviously just for low angular momentum values.

The importance of determining the mass threshold, as already mentioned, is to understand if the merger will or will not create a black hole.

Bauswein and Stergioulas [30] calculated for a TM1 EOS a threshold mass of 3.24 Mo.

The graph they obtain for the TM1 EOS, with a comparison between the total mass of the NS binary system and its angular momentum is this:

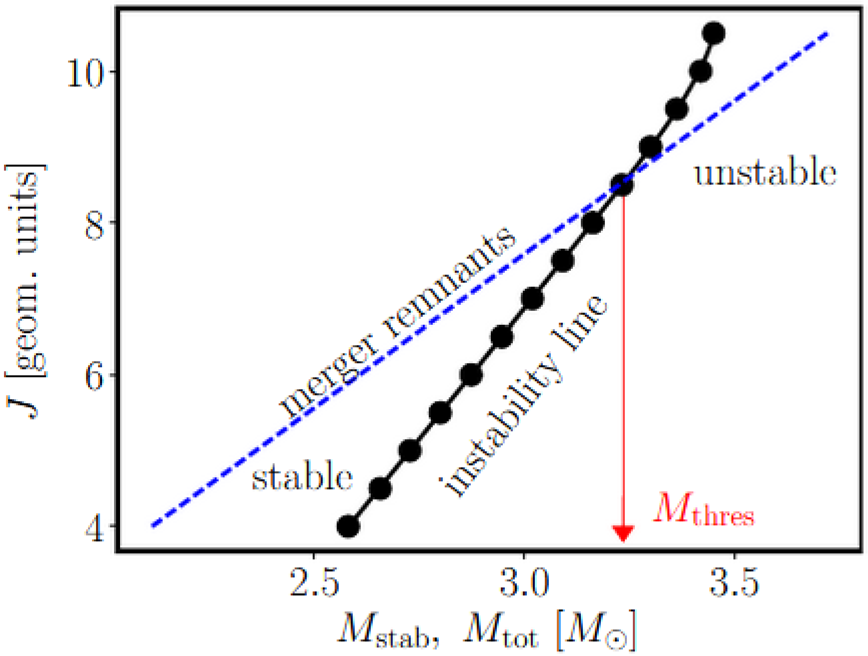

Figure 26: In this figure we have plotted the comparison between the angular momentum of the merger remnants J for differentially rotating NSs respect to the total mass (blue line) and the instability relation (black line) [30]

As we can see, if the total mass of the binary system of neutron stars is small, the merger remnants have an angular momentum which is higher than the one is needed to have stability. Conversely, if the total mass is high enough, the angular momentum of the remnants, which comes from the two neutron stars, is smaller than the one needed to have stability and the binary system collapses to a black hole. The point of intersections of the two lines represents the mass threshold.

3A.2 Other results of the merger

Beyond the case of black hole there are other possible results, if the remnant does not collapse immediately (it is considered an immediate collapse if the BH is formed in less than 1s after the merger): hypermassive star (a configuration which is stable only if there is differential rotation), supermassive star (a configuration which is stable only with rigid rotation present) and finally a star which is in the beginning differentially rotating, but stable even without rotation. In any of these three cases, during the ring-down phase, after the inspiral one, the remnant emits a very powerful GW signal which was studied by using numerical models. In order to understand the behavior of the merger is fundamental the relation between $M_{\rm MAX}$ (the maximum mass of non-rotating neutron stars) and $M_{\rm THRE}$ (the threshold binary mass for prompt collapse to BH). This was subject of study and numerical simulations for Bauswein, Blacker, Vijayan [31]. In the relation between these two masses a key role is played by the tidal deformability of the binary system. We can define the threshold deformability $\Lambda_{\rm THRE}$ as

(3A.2.1) $\Lambda_{\rm THRE} = \Lambda\,(M_{\rm THRE}/2)$

For q=1 where q=M_1 / M_2.

We can now show a tridimensional graph which represents very well the relation among M_{MAX}, M_{THRE} and Λ_{THRE}.

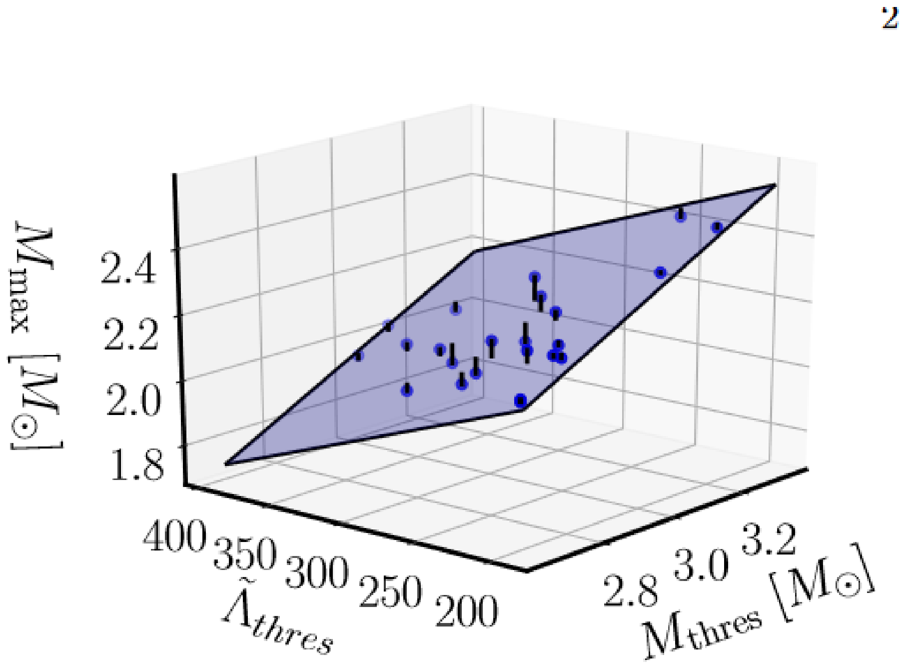

Figure 27: In this figure we see the blue panel which represents the fit among M_{MAX}, M_{THRE}, Λ_{THRE} for q=1. The masses are expressed as solar masses. The short black lines indicate the deviation of the data from the fit. [31]

The bilinear fit which approximates the data is this:

(3A.2.2) $M_{MAX} = a\, M_{THRE} + b\, \Lambda_{THRE} + c$

Where a=0.632 b=-0.002 M_o and c= 0.802 M_o.

This fit is very good because the maximum residual of this fit is just 0.067 M_o.

Another simulation was done with q=0.7. In this case the maximum residual of the fit was 0.078 M_o. The fit parameters were a=0.621, b=-0.001 M_o and c=0.582 M_o. The difference between M_{THRE} (q=1) and M_{THRE}(q=0.7) depends on the choice of the EOS.

Another very interesting result is the behavior of the hybrid stars (a situation between Neutron and Quark stars). In fact, it is possible to make a distinction between hadronic and hybrid stars considering Λ_{THRE} and M_{THRE}. We can see that the hadronic stars are all under the line expressed by the following fit (valid for q=1, but the behavior is similar for q=0.7):

(3A.2.3) $\Lambda_{THRE - HYBRID} = 488(M_{THRE}/ M_o) – 1050$

Above this line we have only hybrid stars. In order to understand better this question, let us look at this picture:

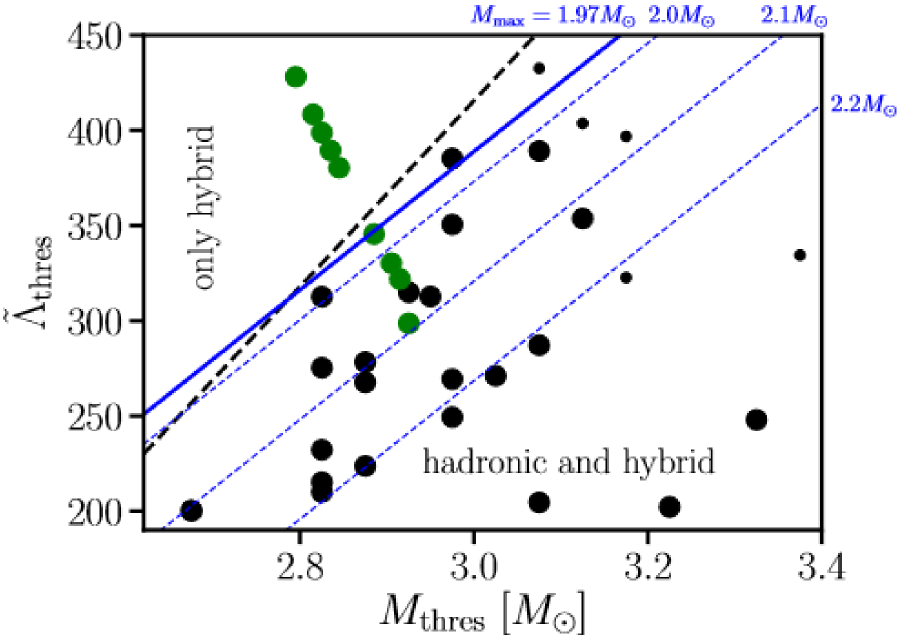

Figure 28: In this figure we have the threshold deformability on the y-axis and the threshold mass on the x-axis. The dashed line indicates the limit for the existence of the hadronic stars. The blue lines are curves of constant M_{MAX} by using the fit (3A.2.2). [31]

The strong phase transition which occurs in hybrid stars produces a softening of the EOS at higher densities, and this causes a destabilization of the merger product by decreasing M_{THRE}. This fact implies that the binary stars with $M_{TOT} = M_{THRE}$ are hadronic and light with a large Λ_{THRE}. From this figure we can also infer that there is a minimum mass below which purely hadronic models are not allowed. This mass is 1.97 M_o.

SUB-CHAPTER 3B: Study of BNS Merger signals and their implications on the destiny of the merger between the collapse to a BH and the formation of a Quark Star

3B.1 Short GRBs and EE signal

Now we are going to deal with the type of gravitational signal produced by binary compact objects. In fact, the process of the merger can be divided into three phases: the inspiral phase, the coalescence phase and the post-merger phase. During the beginning of the first phase is not bad the assumption of point-like stars, because the distance between stars is not very big compared to that of the radius which does not affect the GW signal [32]. When this approximation is no more valid, part of the potential energy is taken to deform the stars, so the inspiral motion increases its speed. After this phase there are different possible outcomes of the result of the merger.

One of this is the creation of a black hole. In this case the GW signal would rapidly disappear.

In order to find an inner engine able to produce a short gamma-ray burst signal, we have to face two issues: the first one is related to the presence of baryonic pollution which is needed to be reduced to have a clear jet, the second one is that not all the short GRBs are followed by EE (Extended Energy) emission [32] [33]. About the production of the EE, two mechanisms were supposed: the emission of the EE after the formation of a proto-magnetar, which would emit the EE signal as a pulsar [34], the other one is related to the formation of an accretion disk around a Black Hole. About the first mechanism the EE signal can be studied by using just two parameters: the magnetic field (10^{15} - 10^{16} G) and the rotation period which is of the order of milliseconds. The star resulted from the merger must collapse to a BH with a delay such that the EE signal is permitted. Nonetheless, we know that the majority of short GRB signals does not emit EE, and this could be related to the formation of a BH in less than a second, hence avoiding emitting EE by accretion disk formation. Now, if we consider the mechanism of EE production related to a proto-magnetar, there are two possibilities. The first one is the collapse of a SuperMassive Neutron Star (SMNS) to a BH. In this case the EE emission comes after the prompt emission due to the BH formation. The EE is produced by a mechanism called "time reversal" [32], because the EE signal is created before the collapse of the proto-magnetar to a BH, but it comes after the prompt signal which is created by the BH formation. The reason why the EE is produced before but comes after the prompt signal (from which the name of "time reversal mechanism") is the effort of the signal to escape from the shell which surrounds the proto-magnetar. The second mechanism of production of the EE signal is related to the formation of a Quark Star (QS) [35] instead of a BH. Luckily for us, it is possible to distinguish among the two cases. In the case of the collapse of the proto-magnetar to a BH the time separation between the moment of the merger, that could be detected via gravitational waves, and the emission of the prompt signal is of the order of 10^3 or 10^4 seconds, while in the case of a QS the time interval is roughly 10 seconds.

Dealing with the reduction of the baryonic pollution, there are two possible mechanisms. The first one is related to the creation of a black hole whose creation would not remove the baryonic material from the surface avoiding the presence of the baryonic material in the signal [36] [33]. The second one is instead related to the formation of a Quark Star, whose deconfinement for quarks would be able to avoid removing baryonic material [35]. The short GRBs lifetime is related to the lifetime of the disk around the BH in the Black hole case, while, in the case of a QS, the lifetime of the GRBs is connected to the process of deconfinement that, when it reaches the surface, stops the signal.

3B.2 The BH case

Now we are going to see in detail how the "time reversal mechanism" works, considering the study made by prof. Ciolfi [37] In this scenario a SMNS is assumed to be formed as result of the BNS merger. This Star has a mass above the Maximum Mass for the non-rotating configuration, but below the Maximum Mass for uniformly rotating configurations. This fact allows the Star to delay its collapse to BH [37]. This scenario can be explained by considering three phases:

a) In the first phase the SMNS is characterized by a strong differential rotation, magnetic field are increased via magnetic wind and the mass ejection is in the form of a baryon-loaded wind and it is highly isotropic. Other mechanisms such as the neutrino-induced outflows can contribute to mass ejection. In a time of roughly 1 second, the differential rotation regime is removed, baryonic pollution around the NS drops and the Star, resulted from the Merger, goes to a uniform rotation regime.

b) At this point the second phase starts and the Star starts emitting spin-down radiation as an ordinary pulsar, inflating a photon- pair plasma nebula behind the expanding optical thick ejecta. The high photon pressure produces a shock across the ejecta, which pushes all the ejecta into a thin shell where there is thermal and kinetic energy.

c) In the third phase the Star collapses to BH. The resulting BH-Torus system produces the condition for launching a relativistic jet able to cross the nebula and the thin ejecta shell, producing the SGRB signal. The energy emitted by the NS resulted from the merger during the second phase, under the form of X-rays, can be seen only after the SGRB (Short Gamma Ray Burst) signal, because it must cross both the nebula and the ejecta shell, whose optical depth is very high and it can slow down the emission.

The following picture can show better the situation.

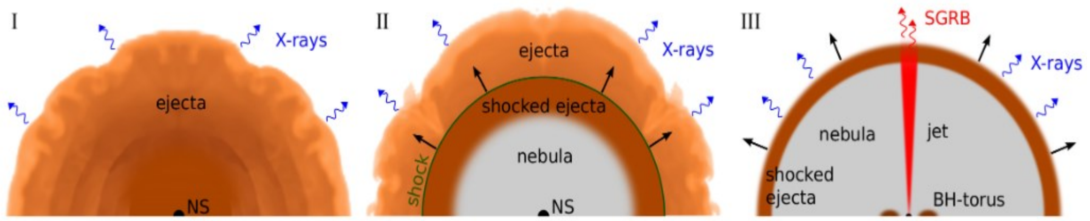

Figure 29: These are the three phases of the time reversal scenario described above. As we can see , while the spin-down radiation is isotropic, the SGRB is collimated [37].

This mechanism is very useful to exclude the EOS are not compatible with the existence of a SMNS. Beyond this, we can consider the time between the merger, inferred by the study of GWs, and the SGRB emission. This time reveals the lifetime of the SMNS. This information can be used to put constraints on the NS properties.

3B.3 The QS case

Now we are going to see the second mechanism of ablation of the baryonic pollution. Whereas the mechanism of reduction of baryonic pollution in the BH case is connected to the accretion disk, and the ablation of baryon is possible until the accretion disk is present, even in analyzing this case we have to distinguish between the “prompt” emission of short GRBs, which lasts for some tenths of a second, and the prolonged emission (EE) that comes after the SGRBs. In the beginning was thought that only a Black Hole could be able to emit SGRBs, then a new model started gaining popularity; in this model the SGRBs emission would be produced by a rapidly rotating proto-magnetar [32]. A signal like the SGRB is the result of the dissipation of a relativistic jet made of pairs of electrons and positrons, photons and a fraction of baryons. Using this model, we are able to fit the EE- signal with the luminosity related to the spin-down dipole (related to the star slow-down) for values of period of the order of milliseconds with great compatibility with the observed data.

Quark Stars are self-bound objects, and neutrinos, whose energies are of the order of tens of MeV, are not energetic enough to remove the baryonic presence from the surface, and this stops the prompt signal (this is why we can speak of short signal) [35]. The high tension of the surface, due to the deconfinement of quarks from the core to the whole star, makes the ablation no more possible. When there is the inner conversion to quark matter, there is a process of a slower burning which lasts for tens of seconds; the star becomes a QS only when this process reaches the surface of the star. About the time the Quark deconfinement needs to reach the surface of the Star, there are uncertainties because, considering the high spin of the Star, if its EOS is very soft, the Star is deformed into an ellipsoid with an equatorial radius longer than the polar one. Thus, the time for quark deconfinement in the polar direction is of roughly 10 or 20 seconds, while on the equatorial direction is 1.2-1.4 the time on polar direction [35].

3B.3.1 The Quark deconfinement

It interesting to see how quark deconfinement works in three different configurations: HS-HS, QS-QS and HS-QS, by considering the analysis of A. Drago and R. De Pietri [38], where HS means Hadronic Star. This distinction is very important because it allow us to understand in which case the GW170817 event can be pigeonholed.

a) The HS-HS case

In this case there is no quark matter in the system before the merger. The process of the formation of quarks from hadronic matter must preserve the flavor composition making the quarks nucleation impossible if hyperons and kaons are not already present. Kaons are mesons (particles made of a quark and antiquark) with a strange quark or antiquark. Hyperons are baryons (particles made of three light quarks) with one strange quark. If we define Y_i is the fraction of baryons as a function of n_b, where n_b is the baryons number density. If n_b increases, we have a bigger production of hyperons and hence a higher probability of a conversion of matter to strange quarks state. In order to have this conversion, the average distance between strange quarks must be smaller than that between two nucleons. Once the strange quarks density reaches high enough values, the quark deconfinement begins. It happens immediately after the merger, because in this case the temperature increases, and we have the formation of the hyperons in the center of the remnant. In the beginning the deconfinement process is very fast (the bulk of the star is converted into deconfined quarks in a few milliseconds) because of the hydrodynamical instabilities [35]. After that, the instabilities tend to switch off and the process becomes much slower (roughly ten seconds for the conversion to quarks of the outer layers of the star).

b) The HS-QS case

In this case, which is the most likely situation for the GW170817 event, the quark deconfined matter is already present and this fact makes the conversion possible, unlike the previous case, even without a hot and dense enough region of the hadronic star where the process of quarks deconfinement takes place (this is known as Coll’s condition) [38]. Furthermore, in this case the deconfinement should be faster because of a higher turbulent regime which makes the area of the mixing of quark and hadronic matter wider.

c) The QS-QS case

In this case we should have a “clean “environment for the fact that the baryonic ablation mechanism is stopped by the strength of quarks interaction in a deconfined quarks state, which is higher than the strength due to nuclear interaction. Even though the absolute absence of baryonic pollution is just an idealization, in this case we would expect a very low rate of detected baryons and, in order to study this case, no Coll’s condition must be taken into consideration.

The figure 30 could show all the three possible cases based on the minimum and the maximum mass of the hadronic and the quark mass, even if in this last case there is a high uncertainty.

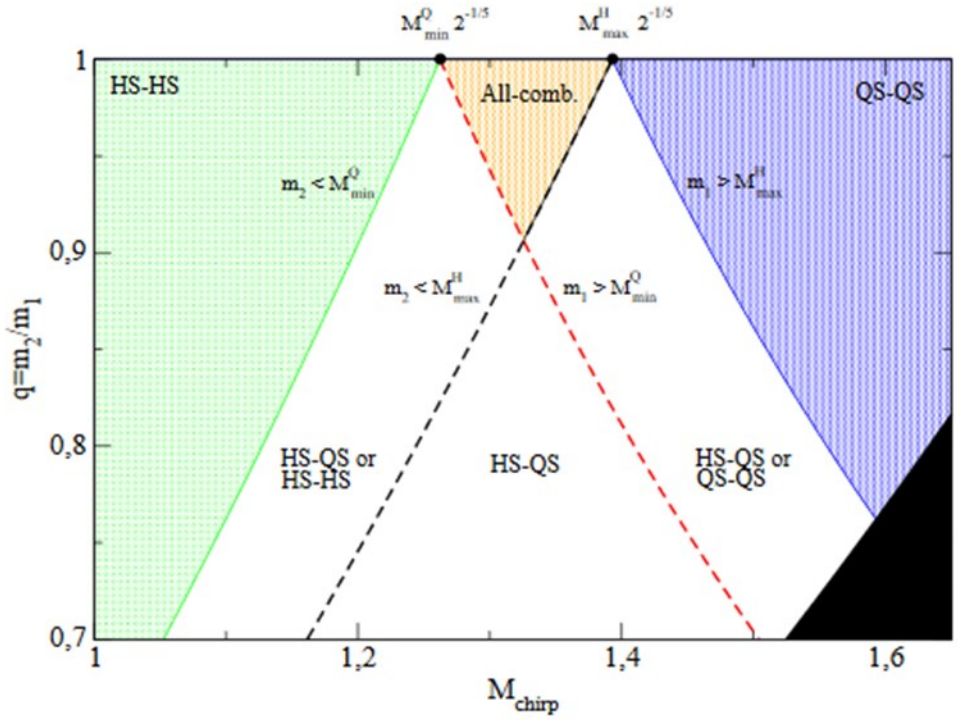

Figure 30: In this figure the maximum hadronic mass M^H_{max} was put equal to 1.6 M_o, while the Minimum one is put equal to 1 M_o about the QSs, the minimum mass is 1.45 M_o, while the maximum one is 2.1 M_o [38].

SUB-CHAPTER 3C: The ejected material from a BNS system(particularly the GW170817 case)

On the 17th of August in 2017 the coalescence of two compact objects with masses which were in the NS range was observed from the NGC 4993 galaxy at roughly 140 million of light years from us [39]. Advanced Ligo and Virgo in cooperation on that date detected a gravitational wave signal that can let us know the chirp mass as shown before. The interesting fact was the detection of a Gamma-Ray-Burst event by Fermi Gamma-Ray burst monitor with a delay that was roughly 1.7 s respect to the merger time [32]. After these two observations many other Electromagnetic observations were made in the γ and X and even optical spectrum. The observations of kilonova are very important in the study of stellar structure. In fact, kilonova spectra are an evidence of the r-process which is responsible of the synthesis of heavy nuclei.

3C.1 The kilonova signal for a BNS system (particularly the GW170817 event)

Till now we have stated that there is an EM signal related to the outflow of matter. But what is the nature of this signal in details?

Part of this signal is the kilonova [32]. The base of this signal are the r-processes which are able to synthetize heavy nuclei (heavier than the iron):

neutron captures, β-decays, photodisintegration and fission reactions. The typical luminosity of this signal is between 10^{41} - 10^{42} erg/s which is three order of magnitude bigger than the Eddington luminosity for a star with the mass of the Sun. These is way it is called kilonova.

In order to treat this topic, we must ask ourselves how many mechanisms of mass ejection are present. There are two kinds of process related to mass ejection: the dynamical ones, which start shortly before the merging process and lasts for few ms after it, and the ejection of some mass of the disk produced around the remnant. This last process lasts from roughly 10 ms after the merger to the collapse of the remnant to a Black Hole. The dynamical processes are in turn divided into two kinds: the one related to tidal deformability, about which I have already written, and the one related to the shock due to the collision of the stars surfaces which produces the expulsion of a part of the crust material [32].

The observation of kilonova signal for GW170817 gave us two kinds of signal: the Blue one which is dominant in early time (roughly 1 day after the merger) and the Red one, whose peaks are detectable roughly 1 week after the merger. The reason of their names is of course due to their spectra. The Blue spectrum with its 5 x 10^{41} erg/s is brighter than the Red one, whose luminosity is instead ten times weaker, and it is associated to low opacities which stays between 0.1 cm^2 /s and 1 cm^2 /s, while the Red one is associated to opacity between 3 and 10 cm^2 /s. The values of opacity for Blue signal are typical of iron or light r-process nuclei. The mass atomic number A for this signal is in general lower than 140 [32]. We know from the data that the rate of the ejected mass related to the Blue signal is of the order of 0.01 solar masses, and the speed is roughly one third of the speed of light. The Red signal instead is related to Lanthanides, heavy nuclei with A>140. The ejected mass for this signal is 4 times bigger and the speed is half than the Blue signal case. At this point the question is on what the opacity depends. An important parameter on which the opacity depends is the electron fraction Y_e. If Y_e is low the ejected matter is richer in neutrons and via β-decays, we have the transformation of some neutrons into protons producing Lanthanides which have a high opacity. For Red kilonova signal Y_e is roughly 0.1 or at most 0.2, for Blue kilonova signal is instead bigger than 0.25. The matter related to the emission of the Blue kilonova signal is dynamically ejected by the shock generated at the contact sources of the two Stars [40] [41] [42] [43]. The tidal ejected mass is characterized by low values of Y_e (roughly 0.1) because the matter which is ejected comes especially from equatorial plane where there is low neutrinos emission and consequently less neutrons and therefore less protons produced by β-decay of the neutrons and this means Red kilonova signal. For diffusion angle θ>30°, the ejected material is less influenced by the neutrino flux, maintaining an electron fraction $Y_e \approx 0.25 - 0.3$. [44] [45] [46]. In order to understand better what it means, this is the reaction which should take place:

$n + v^-_e \to p + e^-$, where n means neutron, v^-_e means antineutrino, p means proton and e^- means electron.

Several simulations have proven that NSs mergers are a likely source for the r- process: [47] [48] [49] [50] [51].

We have to say that other sources for the r-process were considered, such as the supernova. In fact, till a decade ago astrophysicists have taken into consideration the possibility that core-collapse supernova could provide the conditions for the formation of the heaviest neutron-rich nuclei. Nonetheless, several simulations have proven the opposite so far: [52] [53] [54] [55] [56] [57] [58] [47].

3C.2 Mass ejection in details for the GW170817 case

Now we are going to analyze three kinds of ejecta components: the dynamic, the wind and the secular, which are common in any BNS mergers, but they can also use to study the GW170817 case. A classification of the components of the ejecta was made by Hotokezaka and Piran in 2015 [59].

Dynamic: the dynamical ejection is due to two different physical mechanisms. The first one is due to the tidal deformation of the NS, a consequence of the gravitational field which is not axisymmetric. The material gains a high enough angular momentum and the ejection, which is dominant on the equatorial plane, starts before the collision and ends roughly 10 ms after the merger [60] [32]. This material has a very low electron fraction $Y_e<0.1$ [40] [32]. The second mechanism is due to the shock that is formed at the NSs interface, which spreads the crust material [32]. This part of ejection for the GW170817 case has been investigated by prof. Radice [61] by using general- relativistic- hydro-dynamical (GRHD) simulations. In this simulation were plot the relation between the electron fraction and the polar angle and the relation between the mass fraction and the polar angle both in the case of heating and cooling neutrinos. The following two images are related to this model:

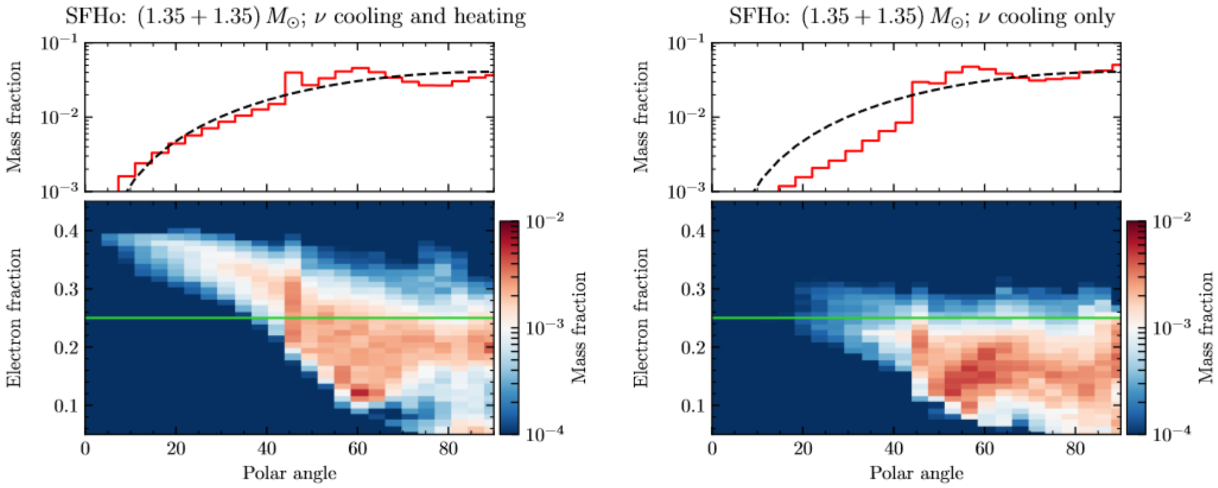

Figure 31: The first image is connected to both heating and cooling neutrinos, the second one is instead related to only cooling neutrinos. In both case we have an EOS of Binary Neutron Stars with equal mass. The total mass of the system is $2.7\ M_o$. In this model the ejection happens to all latitudes, but especially along the equatorial plane. [61]

By taking into account the neutrinos heating process, the angular distribution is well approximated by $F(\theta) = \sin^2 \theta$. An interesting fact related to this model by Radice [61] is that the geometry of the ejection does not depend on the EOS. The ejected mass goes from 10^{-4} to 10^{-2} M_o with a speed which is almost one third of the speed of light. If there is no collapse to BH we have a disk with mass between 10^{-2} and 10^{-1} M_o.

Wind: About the wind Radice [61] obtained, by his model, a uniform distribution, $F(\theta) \approx$ constant, for a polar angle with a maximum of $\pi/3$, and we also have a motion which is slower than that of dynamic, at most roundly 0.08 c. The ejected mass of the disk is just one twentieth made of wind.

Secular: Radice [61] investigated the secular ejection of the GW170817 event, for which we have an electron fraction which stays between 0.1 and 0.4, if we have a collapse of the Massive Neutron Star to a Black Hole. If instead The MNS is extremely long-lived, we have $0.25<Y(\theta)<0.5$.

The mass ejection processes are different in the merger and in the Post-merger phases.

In the first 10 ms of the merger phase ejection proceeds, as already written, on the equatorial plane and it is mostly made of the dynamic component. This ejecta mass depends of course on the stiffness of the EOS, on the total mass and on the ratio of the masses of the two stars. Considering the total mass of 2.7 M_o, we have a dynamical ejection of roughly 0.002 M_o.

In the Post-merger phase the MNS is surrounded by a Torus and, in this case, we have a viscosity and a neutrino - mechanism which produce ejection [62]. During the merger there is a growth of the magnetic field due to the Kelvin-Helmholtz mechanism. This fact induces a MHD turbulence which is responsible of the viscosity mechanism of ejection. After the merger there are two possible destinies of the remnant, depending, also in this case, on the total mass of the system and on the stiffness of the EOS. For stiffer EOS and for small total mass, the MNS survives for seconds or longer. In the opposite case, it collapses to a Black Hole. The following scheme (Figure 32) is able to represent the situation in a better way.

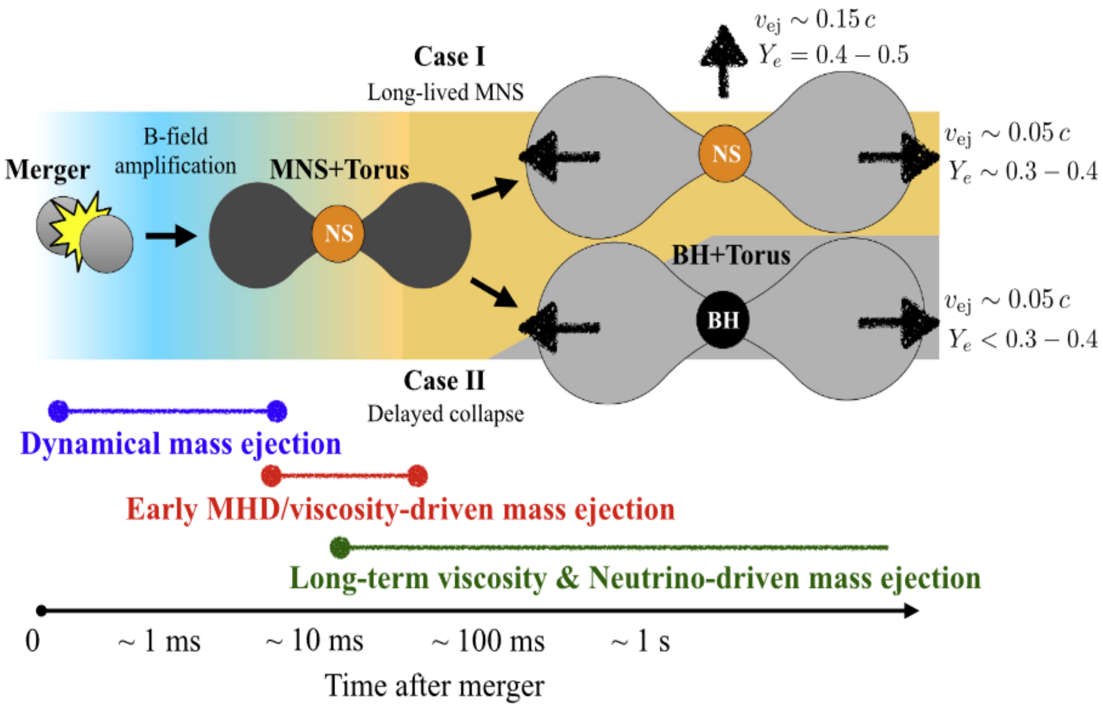

Figure 32: In this image we see the evolution of a binary neutron star merger and its two possible destinies: BH or MNS. [62]

3C.3 The detailed approach to investigate ejecta

In order to investigate ejecta, the approach adopted by Prof. Radice [61] was to split the polar angles into 12 equal intervals and to give each ejected mass (dynamic, wind and secular ejecta) m_{ej} a radial speed v_{rms}. For each mass was expressed in terms of the angular distribution F(θ) in this way:

(3C.3.1) $$m_{ej} = \sum_{k=1,\dots,12} m_{ej,k} = \sum_{k=1,\dots,12} 2\pi \int_{\theta_k-\Delta\theta/2}^{\theta_k+\Delta\theta/2} F(\theta)\sin\theta \, d\theta$$

In this model the $v_{rms}(\theta) \approx$ constant. Another important parameter used in this model is the opacity k which is related to Y(θ). $Y(\theta)>0.25$ for $\theta<\theta_{limit}$ and conversely for $\theta>\theta_{limit}$. Then, was set $k(\theta>\theta_{limit}) = k_{max} > 10$ cm^2 g^{-1} and $k(\theta<\theta_{limit}) = k_{min} < 1$ cm^2 g^{-1}. Then, Prof. Radice calculated by an analytic formula the nuclear heating rate:

(3C.3.2) $$\epsilon_{nuc}(t) = \epsilon_0\, \epsilon_Y(t)\, \frac{\varepsilon_{th}}{0.5}\left[\frac{1}{2} - \frac{1}{\pi}\arctan\left(\frac{t-t_0}{\sigma}\right)\right]$$

where $\sigma=0.11$ s, $t_0 = 1.3$ s, $\epsilon_0 = 1.2 \times 10^{18}$ erg g^{-1} s^{-1}, while ϵ_{th} is the thermalization efficiency.

Now we are going to see an image which shows better the ejecta components with their opacity and distribution.

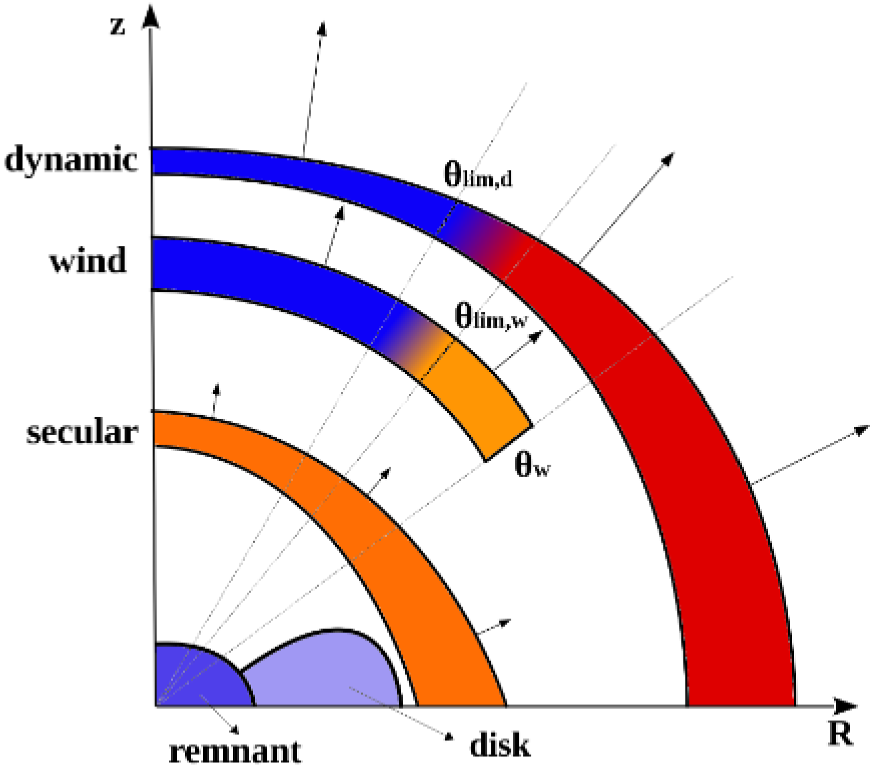

Figure 33: In this image we see the location (z, R) of the three kind of ejecta: secular, wind and dynamic and their spectra. [61]

In this figure we see the three components of ejection within their polar angles of distribution. We see that the wind component is not present for any angle (it is not emitted on the equatorial plane) and its spectrum is mostly in the UV part. The dynamic part is instead present in the whole spectrum with the IR part dominant on the equatorial plane. Another fact which is important is the moment of the peak of the Blue and the Red components of the spectra. Although the wind component has just the Blue part of the spectrum, it is fundamental to give power to the first phase of the Red component. The secular component emits completely in the Red component even if not IR.

3C.3 The comparison between this model and the detected signal AT2017gfo (the Kilonova signal)

In making this comparison different filters were used, exactly 9 filters [61]. The agreement between the model and the observations is expressed in terms of the χ- value which can be expressed as

$$\text{(3C.3.1)} \qquad X^2 = \sum_{n=1}^{Nfts} \left(\sum_{k=1}^{Npts(n)} \left(\frac{m(k,n)obs - m(k,n)the}{\sigma(k,n)obs} \right)^2 \right)$$

Where Nfts is the number of filters, Npts(n) is the number of points in the curve, m(k,n)the is the theorical magnitude of the model, m(k,n)obs is the observed magnitude with σ(k,n)obs its associated error.

There were made three kind of fits for this model [61]. In the first fit, called BF, no constrain to our parameters was imposed and the result was a $X^2 = 759$, not a very high value. The downside was the production of a very small wind component of the ejected matter and an opacity for secular ejecta which is very much lower than that of the dynamic ejecta and as a value which is comparable with that of the maximum opacity of the wind component. This would produce a lower rate for heavy r-process which would be compensated by a slower expansion in order to obtain a non-negligible Red component of the signal. This is the reason why another fit was made. Therefore, in order to produce lanthanides, some constrains about the opacity and the electron fraction of the secular component were put: $k_s \geq 5$ cm^2/g, $0.1< Y_{e,s} <0.4$. The results were a disk mass $M_{DISK} \geq 0.2$ M_o and $m_{ej,\ dyn} \geq 2x10^{-2}$ M_o, which were in contrast with the GRHD simulations. Thus, other two constraints about the mass of the disk and the mass of the dynamic ejecta were put: $M_{DISK} \leq 0.12$ M_o and $m_{ej,\ dyn} \leq 0.01 M_o$. After the introduction of these new constraints, the price to pay was a worse quality of the new fit, called BF $_c$, $\chi^2 = 1263$ [61]. However, in the model with these constraints, the wind component of the ejecta is not negligible anymore and its opacity is comparable with that of the dynamic part. Nevertheless, the issue of these two fits, BF and BF_c, was the observed brightness which would require a heating rate which is in contrast with one related to nuclear mass model, even if we include uncertainties. Therefore, another constraint was necessary. Thus, a constraint on nuclear energy rate was put ($\epsilon_0 = 1.2x10^{19}$ erg g^{-1} s^{-1}) in order to make it compatible with nuclear mass theory. This reduction of the nuclear energy rate produces a bigger amount of the disk ejecta as secular or wind component. Nonetheless, even in this fit, $BF_{c\ e}$, there was a price to pay: a growth of χ^2 of roughly the 15%, compared to BF $_c$ fit [61]. Now, we are going to see a table where there are the parameters range of our values and what was obtained by the three fits.

	Parameter range	BF	$\mathrm{BF_c}$	$\mathrm{BF_{c,\epsilon}}$
χ^2	-	759	1263	1448
M_{disk} $[\mathrm{M}_\odot]$	$\{0.01; 0.08; 0.1; 0.12; 0.15; 0.2\}$	0.08	0.1	0.12
$m_{\mathrm{ej,d}}$ $[10^{-2}\mathrm{M}_\odot]$	$\{0.05; 0.5; 1.0; 2.0; 5.0\}$	1.0	0.5	0.5
ξ_{w}	$\{0.001; 0.05; 0.1; 0.15; 0.2\}$	0.001	0.15	0.2
ξ_{s}	$\{0.001; 0.1; 0.2; 0.3; 0.4\}$	0.4	0.2	0.4
$\theta_{\mathrm{lim,d}}$	$\{\pi/6; \pi/4\}$	$\pi/4$	$\pi/6$	$\pi/6$
$\theta_{\mathrm{lim,w}}$	$\{\pi/6; \pi/4\}$	$\pi/6$	$\pi/6$	$\pi/4$
$v_{\mathrm{rms,d}}$ $[c]$	$\{0.1; 0.13; 0.17; 0.2; 0.23\}$	0.2	0.23	0.2
$v_{\mathrm{rms,w}}$ $[c]$	$\{0.033; 0.05; 0.067\}$	0.067	0.067	0.067
$v_{\mathrm{rms,s}}$ $[c]$	$\{0.017; 0.027; 0.033; 0.04\}$	0.027	0.04	0.04
κ_{d} $[\mathrm{cm\,g^{-1}}]$	$\{(0.5, 30); (1, 30)\}$	(1,30)	(1,30)	(1,30)
κ_{w} $[\mathrm{cm\,g^{-1}}]$	$\{(0.5, 5); (0.1, 1)\}$	(0.1,1)	(0.5,5)	(0.5,5)
κ_{s} $[\mathrm{cm\,g^{-1}}]$	$\{1; 5; 10; 30\}$	1	5	5
θ_{obs}	$n\,\pi/36$ for $n = 0 \ldots 11$	$\pi/12$	$5\pi/36$	$7\pi/36$
$\epsilon_o[10^{18}\mathrm{erg\,g^{-1}\,s^{-1}}]$	$\{2; 6; 12; 16; 20\}$	16	20	12

Table 2: This table shows the parameters of the fit for the AT2017gfo. [61]

In this table ξ_{w} and ξ_{s} are the ratios of the mass of the ejecta (wind and secular component respectively) and the mass of the disk. θ_{obs} is the observation angle for an observer which is very far from the system, like us. A distance of 40 Mpc was considered (1 pc=3.21 l.y.).

It is also interesting to see the plot of light curves respect to time in the three fits of the spectra both in the visible and in the IR band, using different filters, obtaining in both cases a drop of the magnitude.

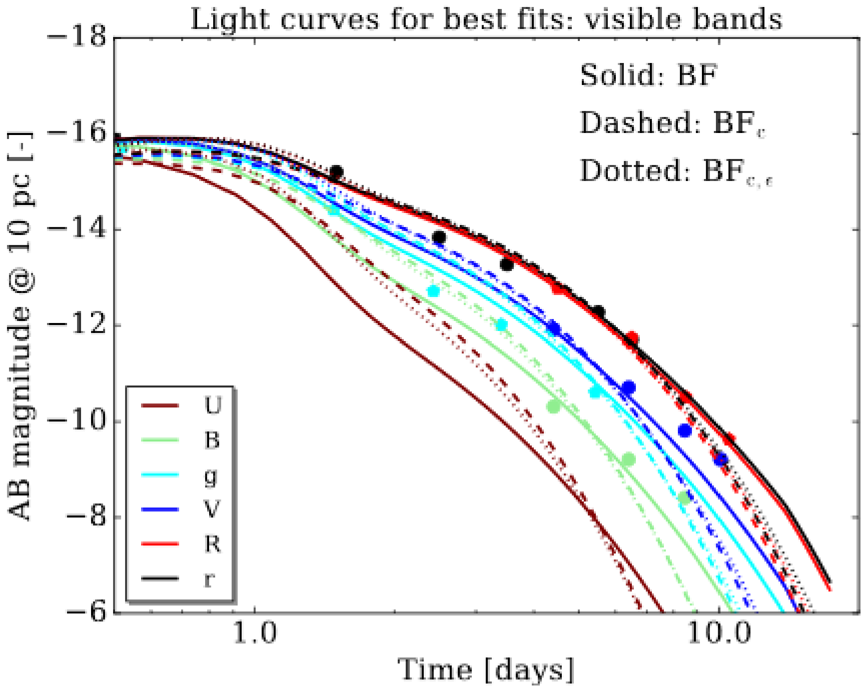

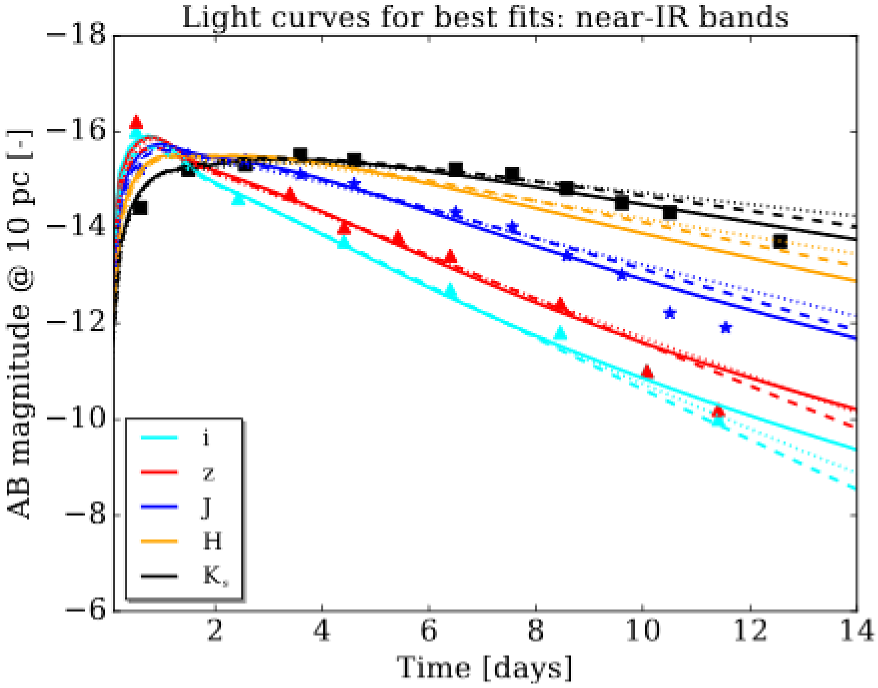

Figure 34: Plot of the magnitude of the light curves in visible spectrum (above) and in the IR (below) [61]

Another interesting thing to see is the sensitivity of our model when a single parameter is modified respect to the set of BF $_c$ fit (even in this case the values of the parameter is respect to time).

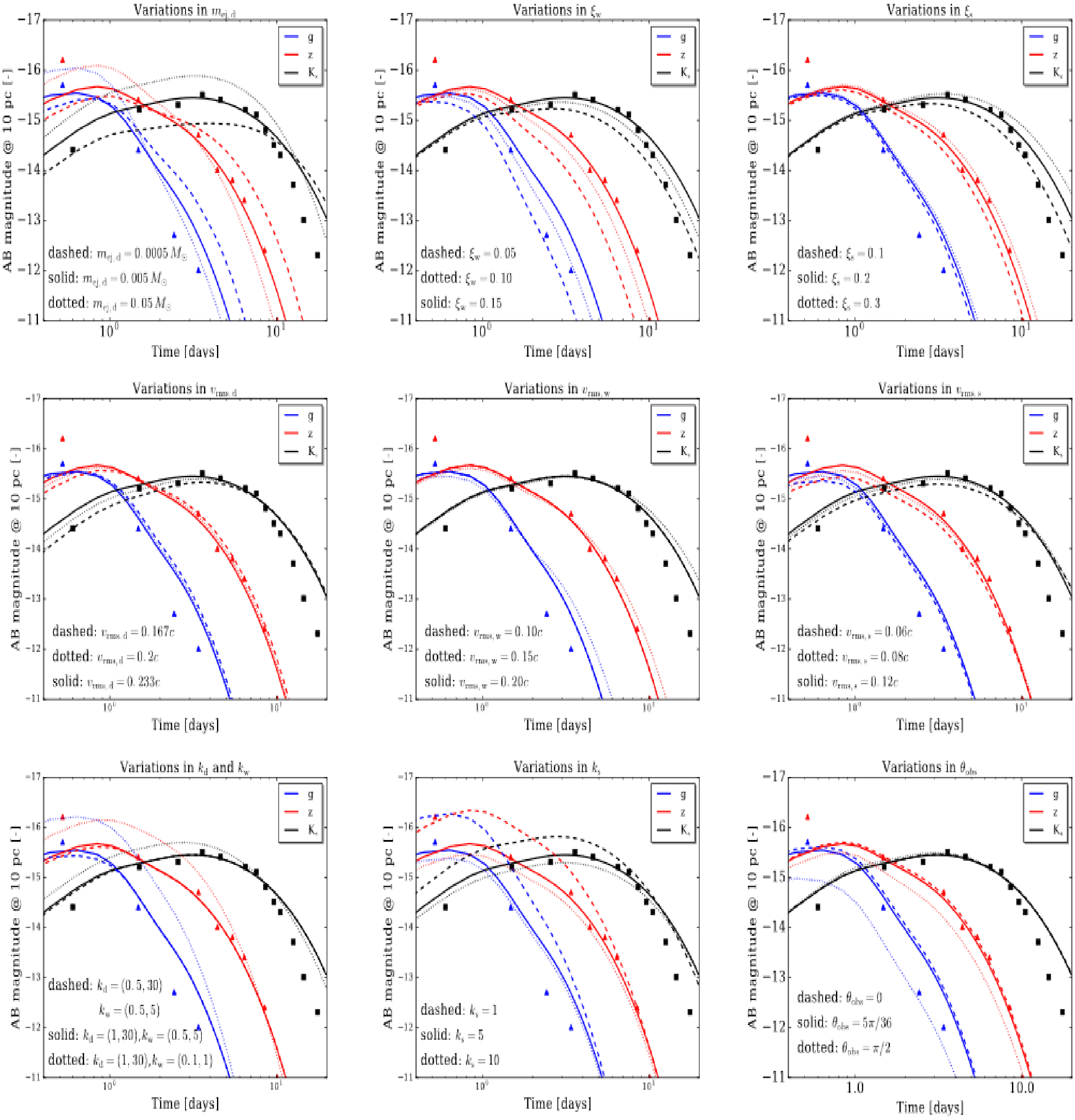

Figure 35: Images of the magnitude of the light curves by modifying each parameter per time using the filters (g, z, k). [61]

3C.4 What can we learn from the kilonova signal of the GW170817 about the structure of the Binary Stars?

From the GWs signal we know that the total mass of the binary systems is 2.74 M_o and this puts a bound of the tidal deformability parameter $\lambda_M < 800$. [32] We also know from the mass of the disk that the stars must be extremely stiff (more massive is the disk, stiffer is the EOS). Different hypothesis was made about the structural nature of this system. The hypothesis of two hadronic stars was refused because in this case the EOS would be soft and to equal radius would correspond less mass. In order to have a bigger amount of mass with the same radius, we need Quark Stars.

The GW170817 event suggests us that the merger of two hadronic stars, since it has a prompt collapse for a mass which is smaller than 2.7 Mo and hence smaller than the mass detected by studying GW170817, cannot be our situation [32] [38]. The other possibility is a system with two QS, but also this one is not realistic, because in this case we would not be able to explain the kilonova signal which, being related to r-process nuclei, is not possible with the ejecta from a Quark Star. The most plausible hypothesis is the HS-QS binary system. In fact, in this case the prompt collapse is avoided and there is no direct creation of a BH, but the formation of a Hybrid Hypermassive configuration. This Hypermassive hadronic configuration is bound to produce a BH once the differential rotation is dissipated, considering the Bauswein's model which, as already seen, finds a relation between mass and angular momentum [63].

3C.5 The GRB170817A signal

A very interesting topic to study is the GRB170817A which is the Gamma-Ray-Bursts. It is interesting because, even though we know that the result of the merger is not an immediate Black Hole, the GRBs seems not to be followed by the EE and this is consistent with a BH created in the first second of the merger, that does not give any chance to the EE to be emitted. Nonetheless, we already know that the creation of a BH cannot be immediate, otherwise we would not have received the kilonova signal in the amount we did. The kilonova signal suggests us the presence of a disk around the merger with a not too short lifetime. Hence, there are two possible reasons behind the fact we did not detect a weaker SGRB signal: the luminosity of the SGRB could be too low or the SGRB was observed off-axis [64] [65] [32] [66]. Considering the study of the GRB170817A made by Ore Gottlieb [66], the SGRB has a very peculiar feature. In fact, even if its fluence $(2.8 \pm 0.2) \times 10^{-7} erg\ cm^{-2}$, and its duration $2 \pm 0.5\ s$,are similar to other observed SGRB signals, when we consider its distance, 40 Mpc, its total isotropic equivalent energy, E_{ISO}=$(5.35 \pm 1.26) \times 10^{46} erg$ is weaker by three orders of magnitude than the weakest SGRB seen before.

3C.6 The viscous effect in the mass ejection

In this chapter we investigate radiation-viscous hydrodynamics simulations for a remnant of a binary neutron star merger, then we perform a radiation hydrodynamics simulation in numerical relativity for a merger of binary neutron stars of equal mass. After that, we evolve the neutron star merger surrounded by a torus by using radiation viscous hydrodynamics simulations in axisymmetric numerical simulations. The assumption of axisymmetry is justified for the fact that after roughly tens of milliseconds the central part of a massive neutron star merger (MNS) reaches that state. Beyond that, this assumption makes the computer simulations shorter [62].

3C.6.1 The description of the simulation method

In analyzing this method, we must decompose neutrinos into two components: the streaming and the trapped one. Then, we write in energy-momentum tensor of the matter in this way:

(3C.6.1) $T^{\alpha\beta}{}_{(tot)} = T^{\alpha\beta} + \sum_i T^{\alpha\beta}(v_i, s)$

Where $T^{\alpha\beta} = T^{\alpha\beta}{}_{(fluid)} + \sum_i T^{\alpha\beta}(v_i t)$ is the sum of the energy-momentum tensor of the fluid and the one of the trapped neutrinos. $T^{\alpha\beta}{}_{(vi,S)}$ is the Energy-Momentum tensor of the streaming neutrinos. The Energy-Momentum tensor follows the following two equations:

(3C.6.2)

$$\nabla_\beta T^{\alpha\beta} = -Q^\alpha_{(\text{leak})} = -\sum_i Q^\alpha_{(\text{leak})\nu_i},$$

$$\nabla_\beta T^{\alpha\beta}_{(\nu_i,\mathrm{S})} = Q^\alpha_{(\text{leak})\nu_i},$$

Where $Q^\alpha{}_{(leak)\,vi}$ indicates the escape rate of the ith species of neutrinos.

Now we can write the explicitly the Energy-Momentum tensor of the viscous fluid with trapped neutrinos:

(3C.6.3) $T_{\alpha\beta} = \rho h u_\alpha u_\beta + P g_{\alpha\beta} - \rho h v \tau^0{}_{\alpha\beta}$

where ρ is the baryon rest- mass density, h=1+ϵ+P/ρ is the specific enthalpy, ϵ is the specific internal energy, u^α is the fluid four velocity, P is the pressure, v is the viscosity coefficient, $\tau^0{}_{\alpha\beta}$ is the viscous stress tensor which satisfies this relation $\tau^0{}_{\alpha\beta} u^\alpha = 0$ [62].

The viscous stress tensor satisfies this relation:

(3C.6.4)

$$\mathcal{L}_u \tau^0{}_{\alpha\beta} = -\zeta(\tau^0{}_{\alpha\beta} - \sigma_{\alpha\beta}),$$

where $\sigma_{\alpha\beta}$ is the shear tensor, that in GR could be thought as the tendency of the initial sphere to be distorted into an ellipsoidal shape, that could be write explicitly in this way:

(3C.6.5)

$$\sigma_{\alpha\beta} = h_\alpha{}^\mu h_\beta{}^\nu (\nabla_\mu u_\nu + \nabla_\nu u_\mu) = \mathcal{L}_u h_{\alpha\beta},$$

In this last equation $h_{\alpha\beta} = g_{\alpha\beta} + u_\alpha u_\beta$, ζ is a number with an inverse proportionality with time. In the used simulation the solutions of the equations of trapped and streaming neutrinos Energy-Momentum tensors [62].

A very interesting topic of the model is the viscosity coefficient v which can be expressed as

$v = \alpha c_s H_{tur}$, where α is a viscosity constant, $c_s = \sqrt{dP/d\rho}$ is the speed of sound, H_{tur} is the largest scale for the eddies when we have a turbulence regime. In our case $H_{tur} = 10$ km which is the same size of the MNS. In our model $\zeta = 3\text{x}10^{-4}$ s. The ζ value must be short enough to make $\tau^0_{\alpha\beta}$ approach $\sigma_{\alpha\beta}$. Now, by knowing the value of v, we can deal with the timescales evolution of the MNS-Torus system. In fact, the viscous effect has a key role in the first 20 ms after the merger [62]. The MNS has a differentially velocity profile in the beginning and by viscosity the angular momentum decreases in the region where it is higher and increases in the ones where it is lower, making the angular momentum speed practically the same in the whole MNS. We are able to make an estimate of the timescales for this process:

(3C.6.6) $$\frac{R_{eq}^2}{v} \approx 10\, ms \left(\frac{\alpha}{0.02}\right)^{-1} \left(\frac{c_S}{c/3}\right)^{-1} \left(\frac{R_{eq}}{15\, Km}\right)^{2} \left(\frac{H_{tur}}{10\, KM}\right)^{-1}$$

In this formula R_{eq} indicates the equatorial radius of the MNS. α was posed as 0.01,0.02 and 0.04 (one simulation per value) because this value is satisfactory in the MHD simulations for binary neutron stars merger. Even if this is true just for the more external regions of the MNS, for simplicity these values were also adopted for internal regions. Furthermore, if we consider longer timescales, we can determine the evolution of the Torus. In making it, the standard accretion theory of the Torus was used [62]. By adopting this theory, we can write down the viscous timescale for the accretion disk:

(3C.6.7) $$t_{VIS} \approx \alpha^{-1} \left[\frac{R_{TORUS}^3}{GM_{MNS}}\right]^{1/2} \left[\frac{H}{R_{TORUS}}\right]^{-2}$$

where M_{MNS} is the mass of the MNS, R_{TORUS} is the typical radius of the Torus, and H is the height. Once we get t_{VIS} [62], we can have the accretion rate by the formula:

(3C.6.8) $$\dot{M}_{MNS} \approx \frac{M_{TORUS}}{t_{VIS}}$$

If we put $M_{MNS} = 2.5\ M_o$, $M_{TORUS} = 0.2\ M_o$, α=0.01, $R_{TORUS} = 50$ Km, $H/R_{TORUS} = 1/3$, we obtain $\dot{M}_{MNS} \approx 0.36\ M_o$ / s. Actually, M_{TORUS} and R_{TORUS} change with time, so this expression based on constant values or Radius and Mass for the Torus is just an approximation.

By using this viscous simulation, we can know how the angular velocity on the equatorial plane changes with time and radius in the first 10 ms, after which the angular velocity is the same in the MNS along its all radius. We can show that in figure 36.

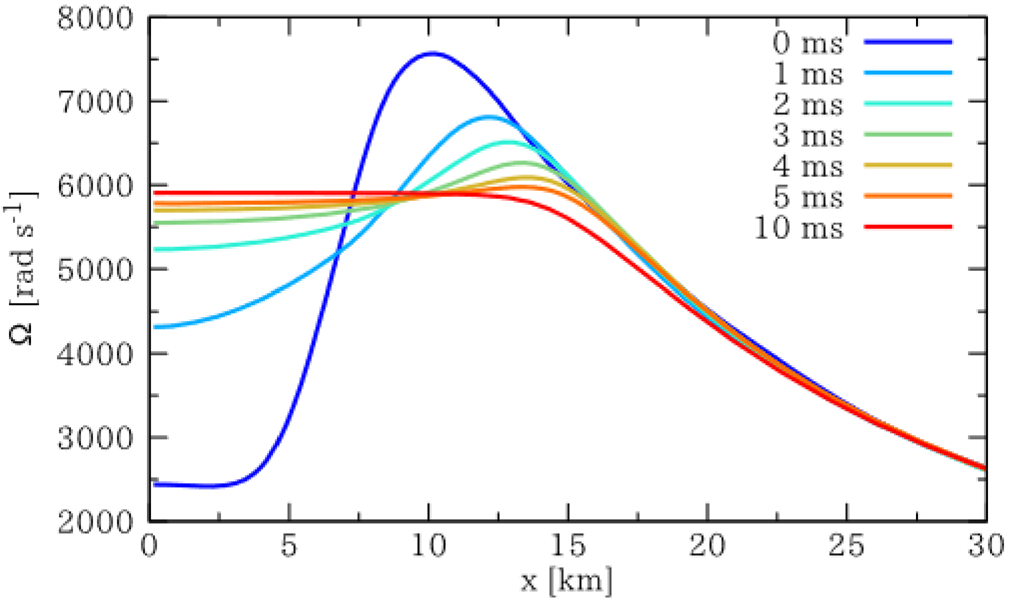

Figure 36: In this figure we can see the angular velocity at the various radii respect to time. [62]

The variation of angular velocity causes a variation of the MNS density profile which produces a sound wave that becomes stronger for high value of α, because the variation of the rotational kinetic energy due to the viscosity is redistributed in the internal region of the MNS in a timescale which goes as α^{-1}. During its propagation, the sound wave drags the material which surrounds the Torus, causing a mass ejection in the first 50 ms, as we can see from these two panels.

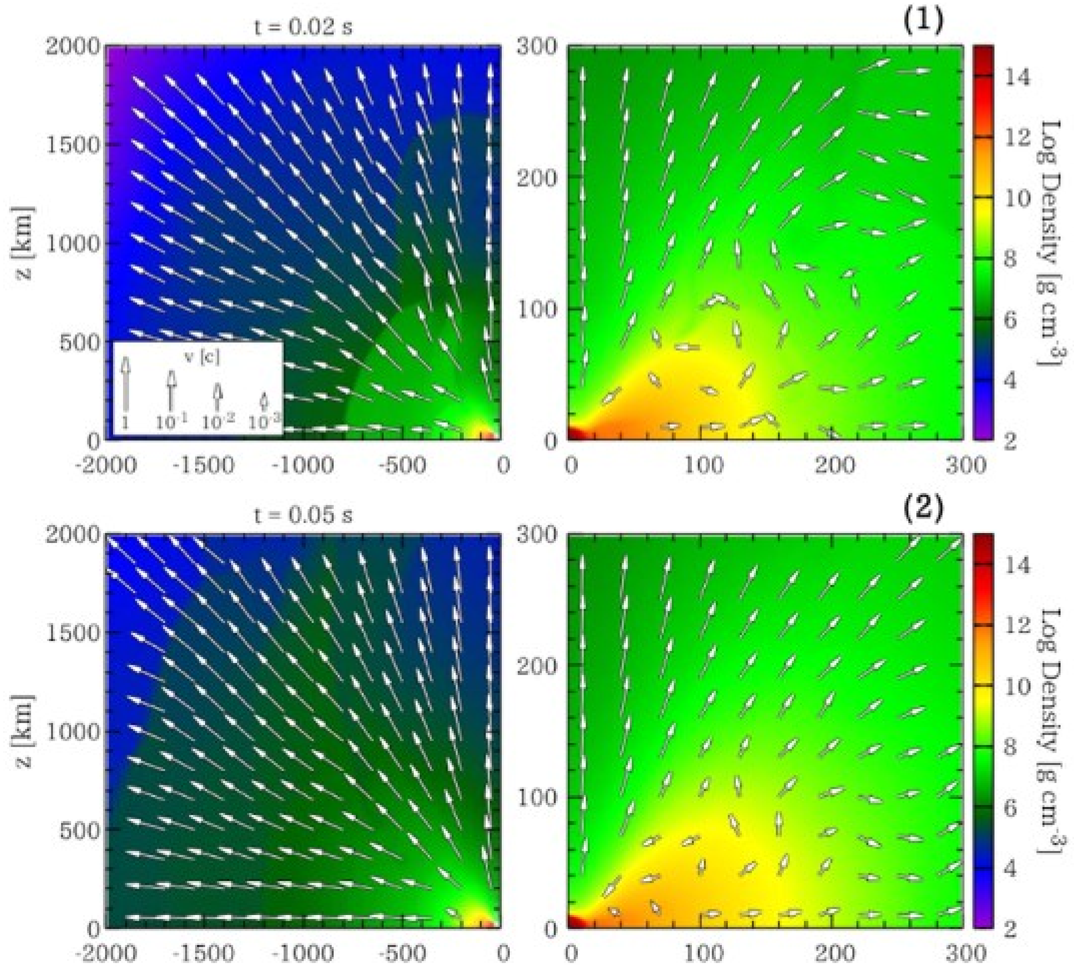

Figure 37: This image shows the density of ejecta along the vertical axis(z) and on the axis(x) a section of the equatorial plane. The same thing is valid for figure 23 below [62].

If the distance from the MNS is smaller than 500 km, the material is still gravitationally bound during the expansion phase for 0.1 ms, after which it turns over and fall again as we can see in these two other panels, whose the first one represents the expansion while the second one the fall.

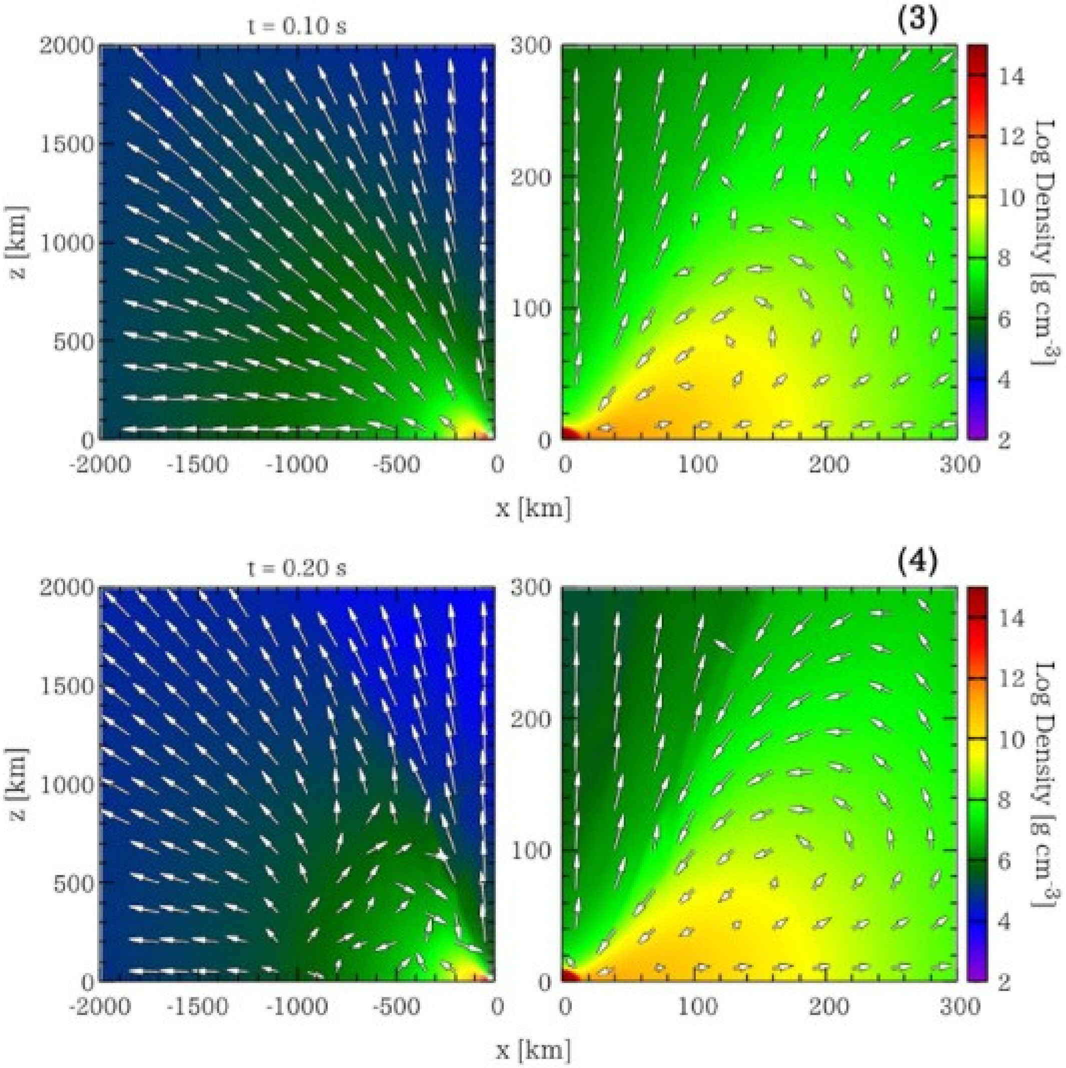

Figure 38: [62]

After the first 50 ms and before 0.2 s both neutrinos’ pair annihilation and viscosity mechanism are roughly equally responsible of heat production. After that, due to a lower neutrino luminosity, viscosity mechanism becomes more influent. The turbulent state does not last forever because the viscosity mechanism of redistribution turns the regime of the flow into a laminal one. After the relaxation in a laminal state the Torus does not emit material in any direction anymore, but on the equatorial plane it emits outward, while on the surface it emits towards the MNS. About this, we can show a plot of the material density on the equatorial plane of the plot with the streaming of the time.

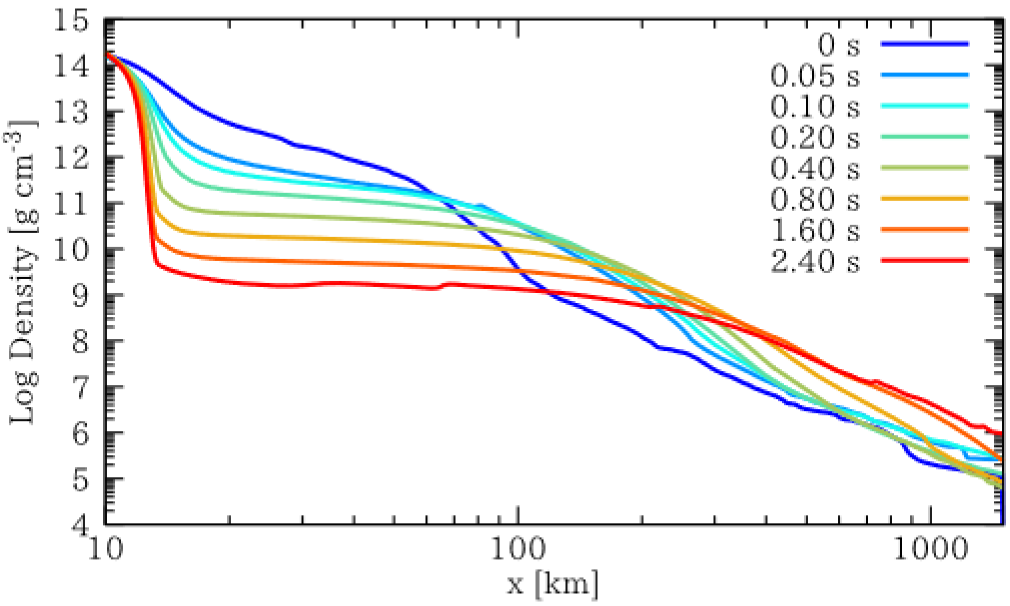

Figure 39: This is the image of the evolution of the Log of density of the Torus between 10 km and 100 km in 2.4 s. [62]

As we can see from this image the expansion of the Torus changes its density by reducing it where it is higher and by increasing it where it is lower towards a state of more homogeneity.

Moreover, it is possible to obtain a relation between the mass of the Torus and time, angular momentum of the Torus and time, radius of the Torus and time. Looking at the image below, we can see that, even though there is no viscosity, the mass and the angular momentum of the Torus decreases with time. Vice versa, the radius of the Torus, which is defined as

(3C.6.9) $$R_{TORUS} = \frac{J^2_{TORUS}}{GM_{TORUS}M_{MNS}}$$

(with J $_{\text{TORUS}}$ is the angular momentum and the mass of the MNS is fixed at 2.6 M_o in this model)

increases with time if there is viscosity, otherwise it remains constant. Figure 43 is the plot of the three quantities respect to time for different values of the viscosity parameter α.

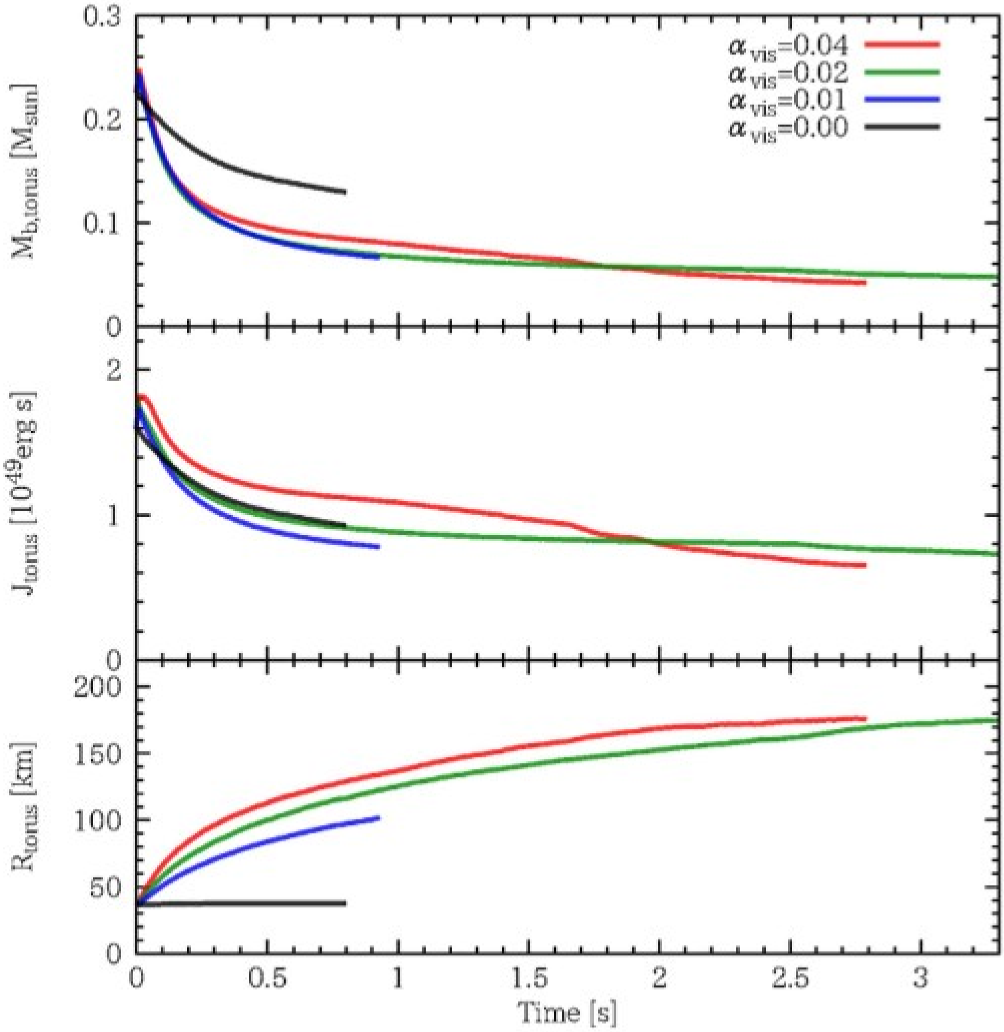

Figure 40: This image shows the evolution of the baryonic mass, the angular momentum J and the radius of the Torus respect to time for three different values of the viscosity parameter α. [62]

CHAPTER 4

ELECTROMAGNETIC SIGNALS FROM BHNS SYSTEMS

4.1 Study of the S190426c case

Now we are dealing with the analysis of what could be thought as the first signal, by gravitational waves, of the coalescence of a neutron star and a black hole, by using the model made by J. Lattimer [67]. In fact, on the 26th of April in 2019 a signal of this kind was detected by Ligo-Virgo Consortium. For this system of coalescence, the S190426c, were estimated the probabilities about the nature of these two compact objects: p_{BNS}=15%, p_{BHNS}=60%, p_{GAP}=25%, p_{BBH}<1%, with the assumption of the cosmic origin of the source.

Moreover, Lattimer, in the elaboration of this model, obtained the relation between $\ln(q-1)$ and $\mathcal{M}$ by fixing four different values of σ_q (1.00,2.00,3.00,4.00). These are the plots:

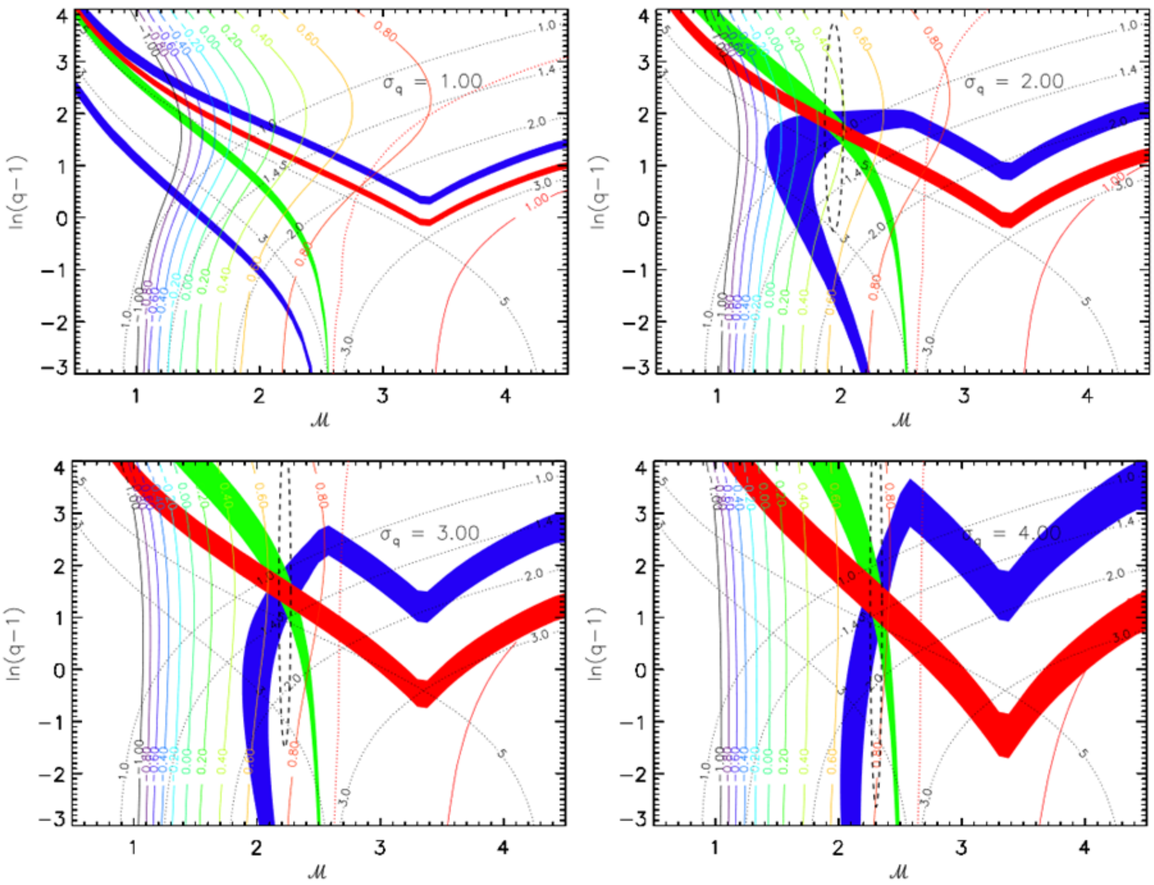

Figure 41: In This figure are shown the probability regions related to the event S190426c. The blue lines are referred to the $p_{GAP} = 0.25\pm0.025$*, the green ones to* $p_{NS} = 0.15\pm0.025$ *and the red ones to* $p_{BHNS} = 0.6\pm0.025$*. The labelled solid contours are referred to the spin parameter* χ*. The dashed ellipsoid represents the inferred 1σ confidence ellipse consistent with all three probabilities. [67]*

Now, for the fact that we have large values of σ_q, uncertainties about the individual masses of the binary systems are quite large. Nonetheless, the mean value of the Black Hole mass is around 6 M_o and it does not depend on σ_q. Dealing with the Neutron Star, we know, following this model, that its mass increases with σ_q until it reaches a maximum value of roughly 1.4 M_o. This model predicts the existence of a very light neutron star. In fact, we can obtain a meaningful solution only for high levels of σ_q. For example, if we take $\sigma_q \approx 1.25$, we obtain neutron stars with 0.25 M_o which is too low to permit its existence, because the minimum neutron stars mass for core-collapse event is around 1.1 M_o. In order to have an estimate of this mass, we must consider the system as symmetric as the binary systems. Therefore, the probability for the lower mass component to have mass M_2 is proportional to $M_2 - M_{MIN}$, with $M_{MIN} < M_2 < M_{TOT}/2$. Only for $\sigma_q \approx 2$, we obtain a value of neutron star mass consistent with the theory of BNS systems. Another reason which supports the choice of neglecting too low values of σ_q, is the fact that for $\sigma_q < 1.5$, the χ value could be lower than -1, which is unphysical because the Black hole would have a naked singularity which is forbidden by Penrose censorship. Figure 10 could show better the relation between the chirp mass, the Black Hole mass, the neutron star mass and the χ value respect to σ_q.

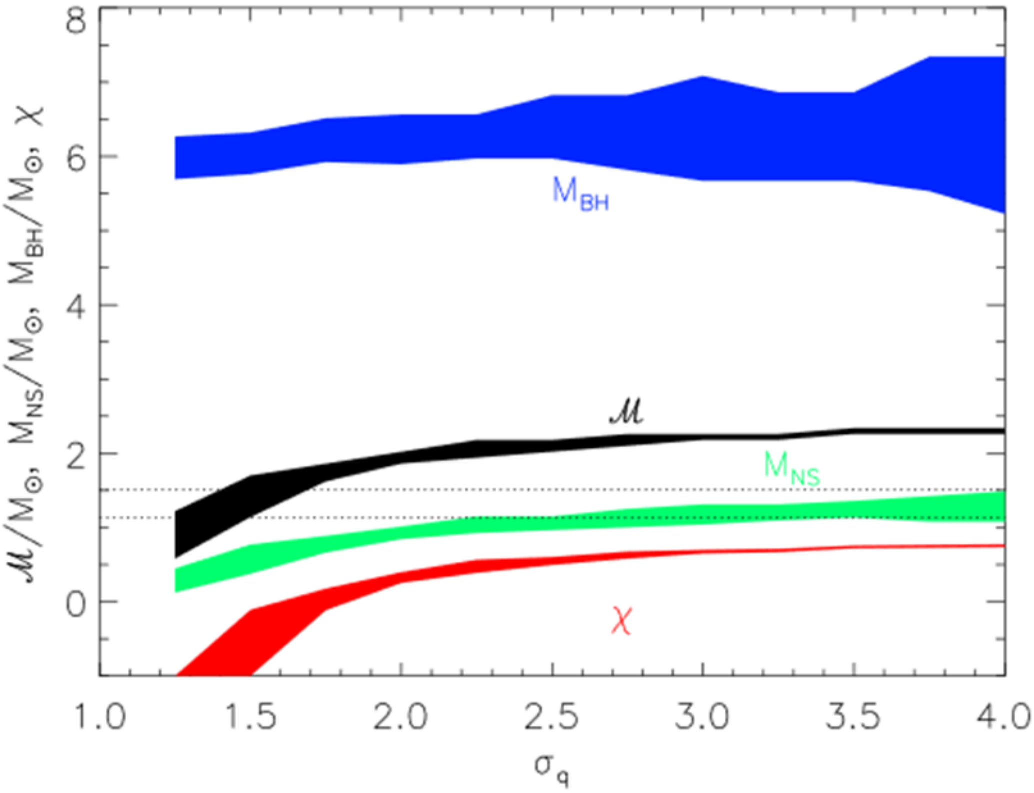

Figure 42:in this plot we see on the x-axis the q-value and on the y-axis $\mathcal{M}/M_{NS}$, M_{BH} expressed in solar masses and the χ value. The dotted lines indicate the 95% of Confidence Level range using the approach of symmetric BNS system. [67]

4.2 Deformability and ejection relation for BHNS systems

So far, we have seen the electromagnetic signals from the GW170817 event, but it is also interesting to see in detail the EM signals from a hypothetical BHNS merger which was studied by Barbieri, Salafia, Perego and Volpi [68] . In this model the Black Hole is described by using two parameters: its mass, M_{BH}, and its spin χ which, as we will see in the next paragraph, is fundamental to determine the radius of the innermost stable circular orbit. Because of gravity the NS approaches, and closer to the BH it becomes, higher is the tidal force. When its distance becomes $d_{TIDAL} = (M_{BH} / M_{NS})^{1/3} R_{NS}$, where R_{NS} is the NS radius, the gradient of gravity due to the BH on the NS is equal to the gravity on the NS induced by itself, and for smaller distances there is a partial disruption of the NS material. Now, if $d_{TIDAL} < R_{ISCO}$, where R_{ISCO} is the radius of the innermost stable circular orbit (co-rotating) of the BH, it is impossible to the disrupted material to escape from the BH and there is no chance to see any EM signal. In the opposite case, $d_{TIDAL} > R_{ISCO}$, the disrupted material is detectable and we can have EM signals. The best situation to have a high amount of detectable disrupted material of the NS is to have a low mass ratio $q = M_{BH} / M_{NS}$ and high BH spin. If M_{NS} is very big the star is more compact and d_{TIDAL} is very short, because, being the star more compact, it is more difficult to tidal forces to produce disrupted material, and only if the BH has a very high spin R_{ISCO} is longer than d_{TIDAL}, otherwise, especially if the BH is very massive, R_{ISCO} is big (4.3.8). The tidal deformability of the NS can be expressed as

(4.2.1) $\Lambda_{NS} = \frac{2}{3} k_2 C_{NS}^{-5}$

where k_2 is the Love number and C_{NS} the NS compactness defined in an explicit way as

(4.2.2) $C_{NS} = \frac{GM_{NS}}{R_{NS}c^2}$

We can see the relation of the tidal deformability with the NS mass in figure 43 for different EOS:

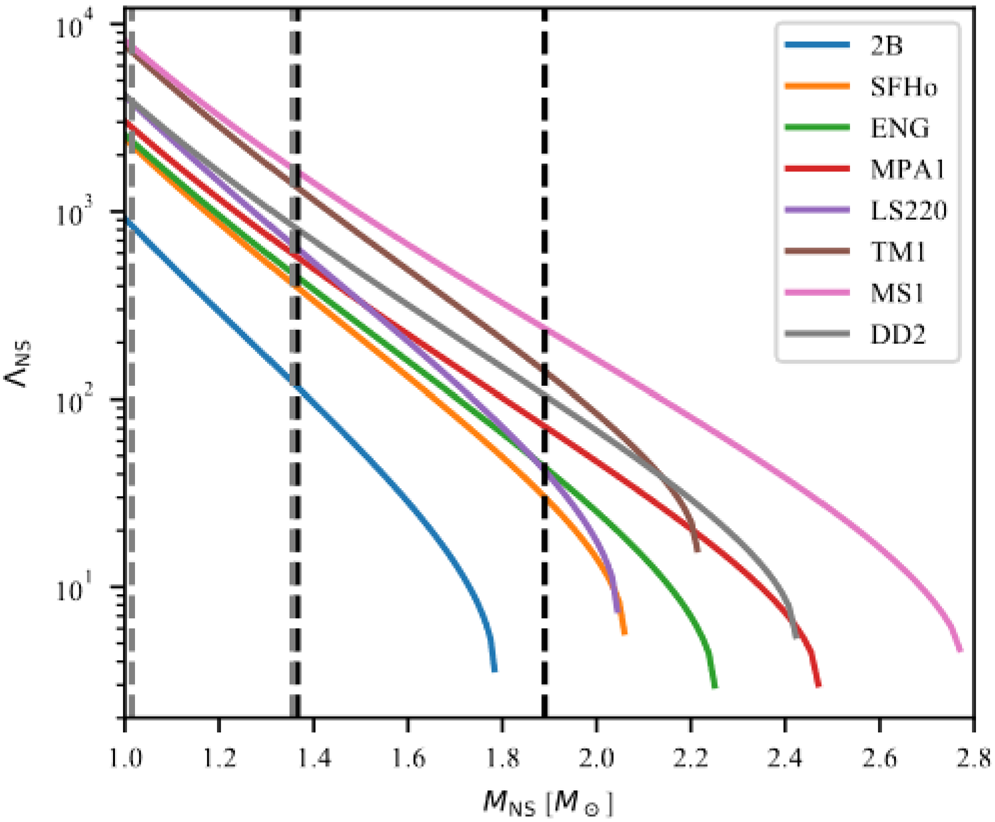

Figure 43: This figure shows the relation between the tidal deformability of the NS and its mass expressed in solar masses (higher is the mass, lower is deformability). The different colors indicate different EOS for the NS from the softest one (blue line) to the stiffest one (pink line) [68].

For the BHNS case we have both dynamical and accretion disk ejecta. The former is related to the unbound material, while the latter to that gravitationally bound. If we study the dynamical ejecta, we discover that for a given pair of M $_{NS}$ and Λ $_{NS}$ we obtain a bigger amount of dynamic ejecta is related to lower BH masses or higher BH spin values or both. And this is also true for the disk accretion mass. This figure 44 will show better this feature where were put M $_{NS}$ = 1.4 M$_o$ and Λ $_{NS}$ =330. (corresponding to SFHo EOS).

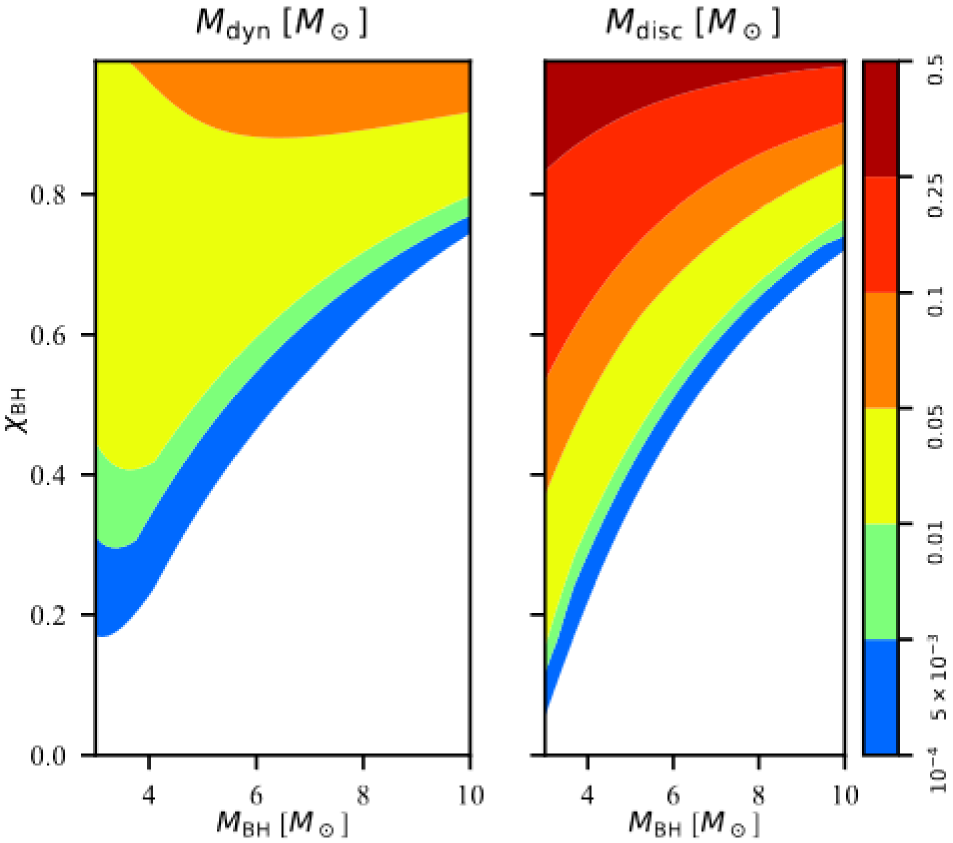

Figure 44: In this plot we see the mass amount of the dynamic part and the disk part of ejection respectively in relation with the BH spin values χ $_{BH}$ and the BH mass M $_{BH}$. Each color represents the mass fraction of dynamic part or the accretion disk part of the ejection. The white color indicates absence of mass. [68]

It is a very interesting fact that whatever value of M $_{NS}$ or Λ $_{NS}$ we take, there is no total disruption of the neutron star mass, but at most the 42% of it. For example, if we consider the MS1 EOS, which is the stiffest one, dynamic + accretion disk ejecta does not overcome the 40% of the total mass of the neutron star. We have already seen the amount of ejecta with the variations of the BH mass and spin by keeping constant the NS mass and its tidal deformability. Now we are going to see the amount of ejecta by keeping constant the BH mass and its spin and by varying the NS mass and its deformability.

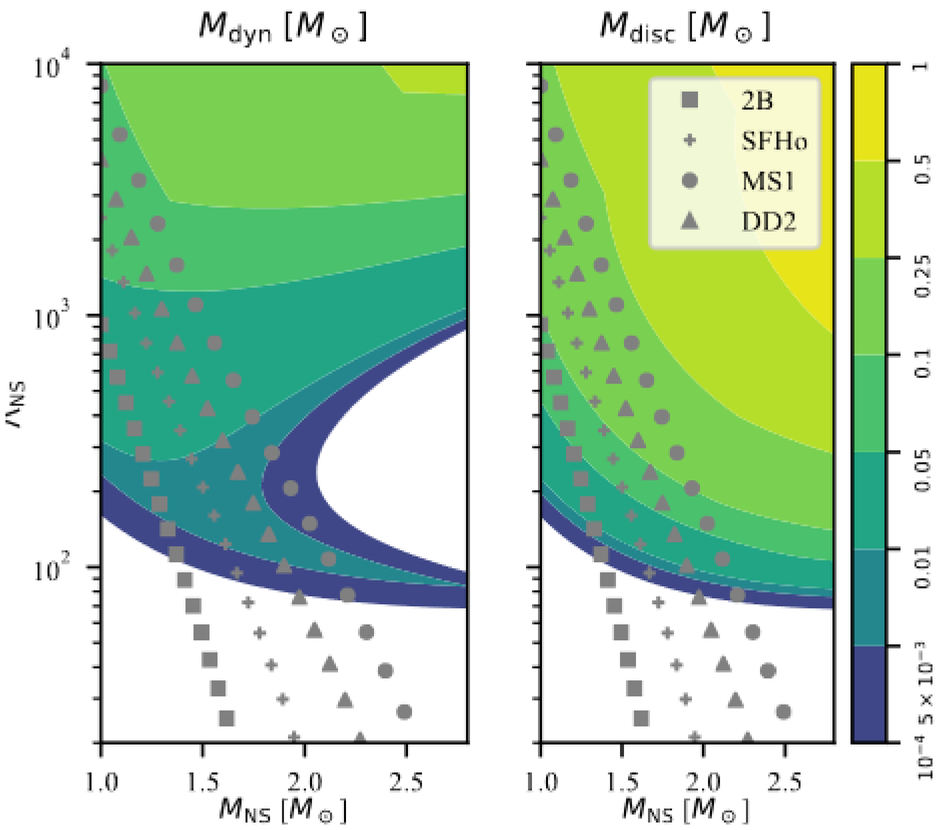
$M_{\rm dyn}$ [$M_\odot$]
$M_{\rm disc}$ [$M_\odot$]
$\Lambda_{\rm NS}$
10^4
10^3
10^2
1.0
1.5
2.0
2.5
$M_{\rm NS}$ [$M_\odot$]
2B
SFHo
MS1
DD2
1
0.5
0.25
0.1
0.05
0.01
5×10^{-3}
10^{-4}

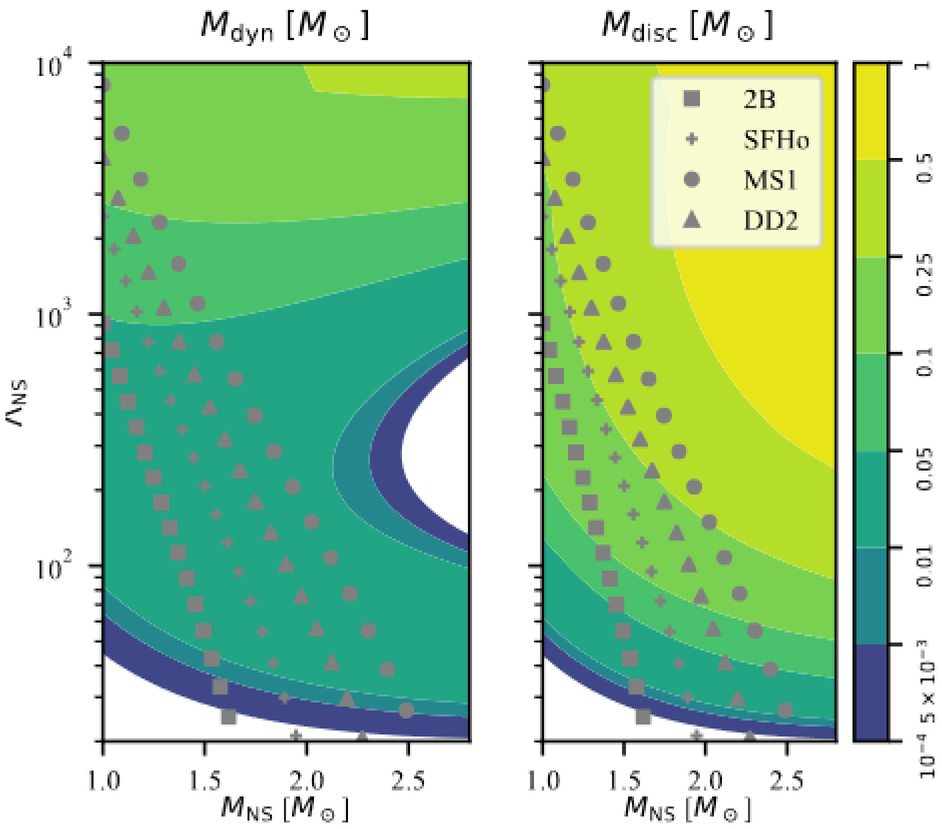
$M_{\rm dyn}$ [$M_\odot$]
$M_{\rm disc}$ [$M_\odot$]
$\Lambda_{\rm NS}$
10^4
10^3
10^2
1.0
1.5
2.0
2.5
$M_{\rm NS}$ [$M_\odot$]
2B
SFHo
MS1
DD2
1
0.5
0.25
0.1
0.05
0.01
5×10^{-3}
10^{-4}

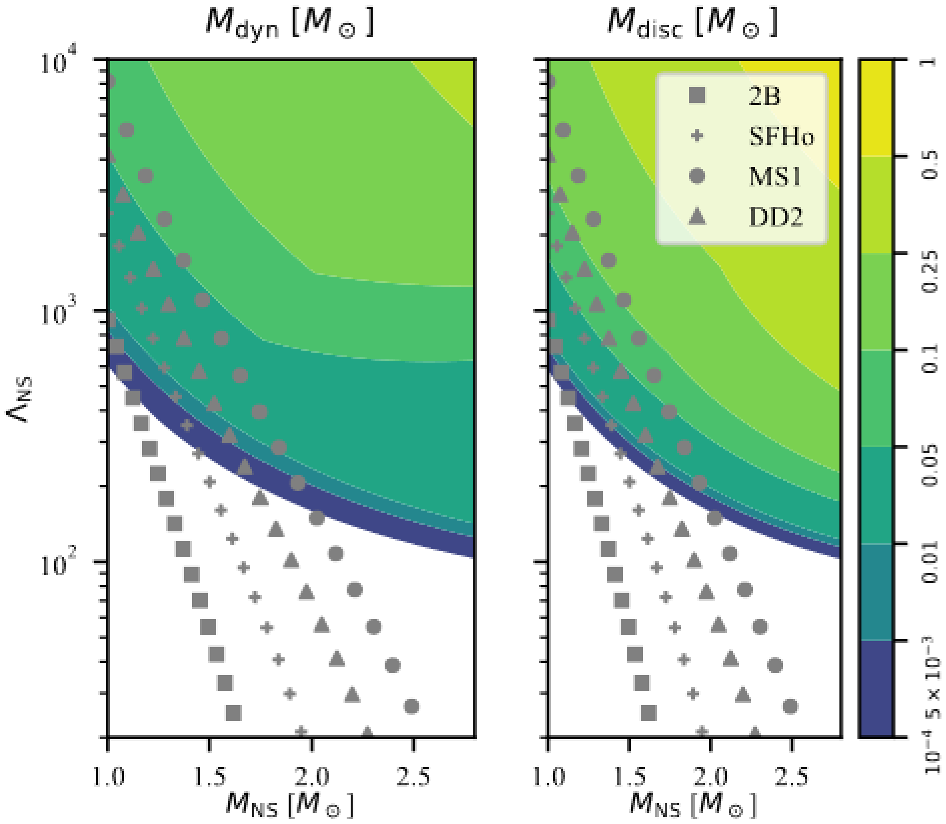
$M_{\rm dyn}$ [$M_\odot$]
$M_{\rm disc}$ [$M_\odot$]
$\Lambda_{\rm NS}$
10^4
10^3
10^2
1.0
1.5
2.0
2.5
$M_{\rm NS}$ [$M_\odot$]
2B
SFHo
MS1
DD2
1
0.5
0.25
0.1
0.05
0.01
5×10^{-3}
10^{-4}

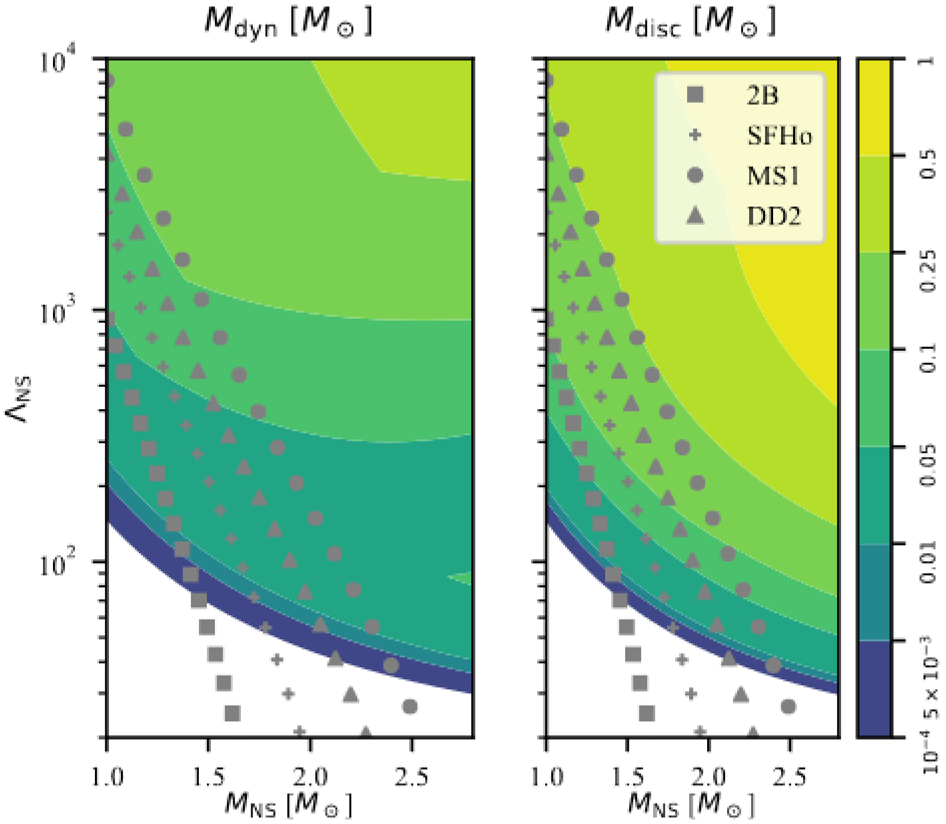

Figure 45: In these four images is shown the amount of dynamic ejecta on the left and the amount of disk accretion ejecta on the right based on the relation between M_{NS} and Λ_{NS} for four kind of EOS. In the first image were taken $M_{BH} = 3\ M_o$ and $\chi_{BH} = 0.5$, in the second image $M_{BH} = 3\ M_o$ and $\chi_{BH} = 0.8$, In the third image $M_{BH} = 6\ M_o$ and $\chi_{BH} = 0.5$, and in the fourth one $M_{BH} = 6\ M_o$ and $\chi_{BH} = 0.8$. [68].

4.3 A digression: the Kerr metric and the innermost stable circular orbit

We have already spoken of R_{ISCO} as the radius of the innermost stable circular orbit. We will not discuss the Kerr metric as a whole here, just what we need to face the way by which we can obtain R_{ISCO}.

Now we are writing down the Kerr metric tensor in the Boyer-Lindquist's coordinates [69]:

(4.3.1) $$ds^2 = \frac{\Delta - a^2 \sin^2\theta}{\rho^2} c^2 dt^2 + \frac{4\mu a r \sin^2\theta}{\rho^2} c dt\, d\varphi - \frac{\rho^2}{\Delta} dr^2 - \rho^2 d\theta^2 - \frac{\Sigma^2 \sin^2\theta}{\rho^2} d\varphi^2$$

where a=J/Mc and is the spin parameter, J is the spin momentum, M the mass of the spinning black hole, c is the speed of light in the vacuum. We have $\rho^2 = r^2 + a^2 \cos^2\theta$, where r is the radial coordinate, θ is the vertical angle for which $\pi \geq \theta \geq 0$. We can write $x = (r^2 + a^2)^{1/2} \sin\theta \cos\varphi$, $y = (r^2 + a^2)^{1/2} \sin\theta \sin\varphi$, $z = r\cos\theta$, where φ, for which $2\pi \geq \varphi \geq 0$, is the horizontal angle.

Δ can be expressed as $\Delta = r^2 - 2\mu r + a^2$, where $\mu = GM/c^2$ with G gravitation constant. Σ can be expressed as $\Sigma^2 = (r^2 + a^2)^2 - a^2 \Delta \sin^2 \theta$.

In order to get the radius of the innermost stable circular orbit, we must rewrite the metric by putting $\theta = \pi/2$, considering only trajectories on the equatorial plane. The metric tensor becomes:

(4.3.2) $ds^2 = (1 - \frac{2\mu}{r})\, c^2 dt^2 + \frac{4\mu a}{r} c\, dt\, d\varphi - \frac{r^2}{\Delta}\, dr^2 - (r^2 + a^2 + \frac{2\mu a^2}{r})\, d\varphi^2$

Now, considering the Lagrangian $L = g_{\mu\nu}\, dx^\mu/d\tau\, dx^\nu/d\tau$ and the fact that $p^\mu = dx^\mu/d\tau$, where τ is the proper time. Thus, we can write down p_t and p_φ in this way:

(4.3.3) $p_t = g_{tt} \frac{dt}{d\tau} + g_{t\varphi} \frac{d\varphi}{d\tau} = (1 - \frac{2\mu}{r})\, c^2 \frac{dt}{d\tau} + \frac{2\mu a c}{r} \frac{d\varphi}{d\tau} = k\, c^2$

(4.3.4) $p_\varphi = g_{\varphi t} \frac{dt}{d\tau} + g_{\varphi\varphi} \frac{d\varphi}{d\tau} = \frac{2\mu a c}{r} \frac{dt}{d\tau} - (r^2 + a^2 + \frac{2\mu a^2}{r}) \frac{d\varphi}{d\tau} = - h$

where $k = E/(m_0 c^2)$, with m_0 is the rest mass and h is the angular momentum of the particle.

The energy could be expressed as $g^{\mu\nu} p_\mu p_\nu = e^2$, where $e^2 = c^2$, for a massive particle, and $e^2 = 0$ for massless particles like photons. Since $p_\theta = 0$, we have

(4.3.5) $g^{tt} (p_t)^2 + 2\, g^{t\varphi} p_t\, p_\varphi + g^{\varphi\varphi} (p_\varphi)^2 + g^{rr} (p_r)^2 = e^2$

Now $p_r = g_{rr}\, dr/d\tau$ and $g^{rr} = 1/g_{rr}$. Now, we consider the matrix G= $\begin{pmatrix} gtt & g\, t\varphi \\ g\, t\varphi & g\, \varphi\varphi \end{pmatrix}$. In order to obtain g^{tt}, $g^{t\varphi}$, $g^{\varphi\varphi}$, we must take the inverse matrix G^{-1} = (1/|DET G|) $\begin{pmatrix} g\, \varphi\varphi & -g\, t\varphi \\ -g\, t\varphi & gtt \end{pmatrix}$. At this point we get $g^{tt} = g_{\varphi\varphi}$/|DET G|, $g^{t\varphi} = - g_{\varphi t}$/ |DET G|, $g^{\varphi\varphi} = g_{tt}$/|DET G|. After the right substitutions, we can write:

(4.3.6) $(\frac{dr}{d\tau})^2 = c^2k^2 - e^2 + (2\, e^2 \frac{\mu}{r}) + [a^2 (c^2k^2 - e^2) - h^2] \frac{1}{r^2} + 2\mu\, (h - ack)^2\, \frac{1}{r^3}$

We can write the above equation in this form:

(4.3.7) $\frac{1}{2} (\frac{dr}{d\tau})^2 + V\,(r;\, h,\, k) = \frac{1}{2}\, c^2 (k^2 - 1)$

For equatorial circular motion particles $dr/d\tau = 0$ and $dV/dr = 0$ if $r = r_c$, where r_c is the radius of the orbit we are looking for. In order to have stability, another condition is required: $d^2V/dr^2 = 0$ for $r = r_c$. In this way we get this equation:

(4.3.8) $r^2 - 6\mu r - 3a^2 - 8a(\mu r)^{1/2} = 0$ and $r^2 - 6\mu r - 3a^2 + 8a(\mu r)^{1/2} = 0$

The first one is valid for counter-rotating orbits, the second one for co-rotating orbits. When a=0, there is no spin, r=6μ, we recover Schwarzschild case. In the extreme Kerr limit, a=μ, we find that r=9μ is the innermost stable counter-rotating circular orbit, and that r=μ is the innermost stable co-rotating circular orbit. χ, the spin parameter used by Lattimer [67], can be expressed in terms of R_{ISCO} as

(4.3.9) $$\chi = \frac{{R^*_{ISCO}}^{1/2}}{3}\left[4-\left(3R^*_{ISCO}-2\right)^{1/2}\right]$$

Where $R_{ISCO}^* = R_{ISCO}\, c^2/(GM_{BH})$, where M_{BH} is the mass of the Black Hole.

4.4The kilonova emission in the BHNS case

In this case, like in the case of GW170817 case, the neutron-rich material produced by the disruption of the NS due to tidal forces, follows a decay process in which it releases a kilonova signal.
There are three different mechanisms of ejection even in this case: the dynamical ejection produced by tidal interactions, the wind ejection produced by the accretion disk during the cooling phase of neutrinos, and the viscous mechanism produced by magnetically viscous processes related to nuclear recombination [68].

a) Wind and secular emission

Wind ejecta are produced on a timescale of tens of milliseconds by the accretion disc during the initial neutrino cooling phase [70] through neutrino matter interaction and neutrino pressure [71] [72].In order to treat this topic, like in the GW170817 case, we consider the system as symmetric respect to the total angular momentum direction, and using this symmetry we divide the polar angle into 30 equal parts and for each part there is its velocity in the radial direction v_{ej} and its mass of the ejected material m_{ej} and its opacity k_{ej}. We know by numerical simulations that there is this relation between mass of wind and secular ejecta and their speed [68]:

(4.4.1) $$\frac{dm}{dv} \propto \left[1-\left(\frac{v}{v_{MAX}}\right)^2\right]^3$$

where v_{MAX} is the maximum velocity of ejecta.

Considering the opacity k, we can write the optical depth which can be defined as

(4.4.2) $\tau = k\, \rho_M\, \Delta r$,

where τ is the optical depth, ρ_M is the average density of ejecta and Δr is the distance travelled by radiation emission. In this model there is the assumption that the emission is that of a blackbody. Based on this factor τ, we can consider the radiating shell between τ= c/v and τ=2/3, between the diffusion surface and the photosphere above which thermalization is no more efficient. When $\tau<c/v$ we have diffusion and the time when the diffusion surface corresponds to the radiating shell at the speed v is given by

(4.4.3) $t=\left(\frac{km_{>v}}{4\pi vc}\right)^{1/2}$

where

(4.4.4) $m_{>v}=m_{ej}\left[1+F\left(\frac{v}{v_{MAX}}\right)\right]$

with

(4.4.5) $F(x)=\frac{5}{16}x^7-\frac{21}{16}x^5+\frac{35}{16}x^3-\frac{35}{16}x$

Is the mass beyond the velocity v.

The time at which the photosphere corresponds to the radiating shell at velocity v is [68]:

(4.4.6) $t=\left(\frac{3km_{>v}}{8\pi v^2}\right)^{1/2}$

The opacity changes considering that we have ionization for the Lanthanides and then their recombination with a huge increase in opacity. After the recombination the photosphere re-enters keeping its temperature at the moment of recombination. The photosphere radius before recombination is:

(4.4.7) $R_{PHOT}=v_{PHOT}\,t$

while, after the recombination the photosphere radius can be expressed as

(4.4.8) $R_{PHOT}=\left(\frac{L_{BOL}}{\Omega\sigma_{SB}T_{La}^4}\right)^{1/2}$

where L_{BOL} is the bolometric luminosity which can be expressed as

(4.4.9) $L_{BOL}=\dot{\epsilon}_{NUC}\ m_{RAD}$

where

(4.4.10) $\dot{\epsilon}_{NUC}=\varepsilon_0\frac{\varepsilon_{th}}{0.5}\left[\frac{1}{2}-\frac{1}{\pi}arctan\left(\frac{t-t_0}{\sigma}\right)\right]$

is the evolution of the efficiency of nuclear reaction with the streaming of the time and:

(4.4.11) $m_{RAD} = m_{>v\,DIFF} - m_{>v\,PHOT}$

Ω is the subtended solid angle and σ_{SB} is the Stefan-Boltzmann constant.

b) Dynamical emission

They are produced on timescales of milliseconds by tidal interactions [73] . About the dynamical ejecta we consider the angle θ from the equatorial plane. The distribution in longitudinal direction is between $-\theta_{DYN} < \theta < \theta_{DYN}$. [68] For sake of simplicity, we will deal with just the positive angles ($\theta > 0$). The diffusion time in latitudinal direction can be obtained by this equation:

(4.4.12) $t_{DIF\text{-}LAT} \approx \frac{(\theta_{DYN}-\theta)^2}{\theta_{DYN}\,\varphi_{DYN}} \frac{k_{DYN}}{ct} \frac{dm}{dv}$

where φ_{DYN} is the maximum angle of emission in the latitudinal direction. k_{DYN} is the opacity of the dynamic ejecta. The time of the radial diffusion can be obtained by this equation:

(4.4.13) $t_{DIF\text{-}RAD} \approx \frac{k_{DYN}\, m_{DYN>V}\,(v_{MAX}-v)}{c\,\theta_{DYN}\varphi_{DYN} v^2\, t}$

We can also compute the angle above which the time of diffusion in the longitudinal direction is shorter than that in the radial direction. This angle is:

(4.4.14) $\theta_{LAT}(v) = \theta_{DYN} - \min\left\{\theta_{DYN}, \left[\frac{m_{DYN>v}\,(v_{MAX}-v)}{v^2 \frac{dm}{dv}}\right]^{1/2}\right\}$

In order to understand better the situation, we must see the following figure.

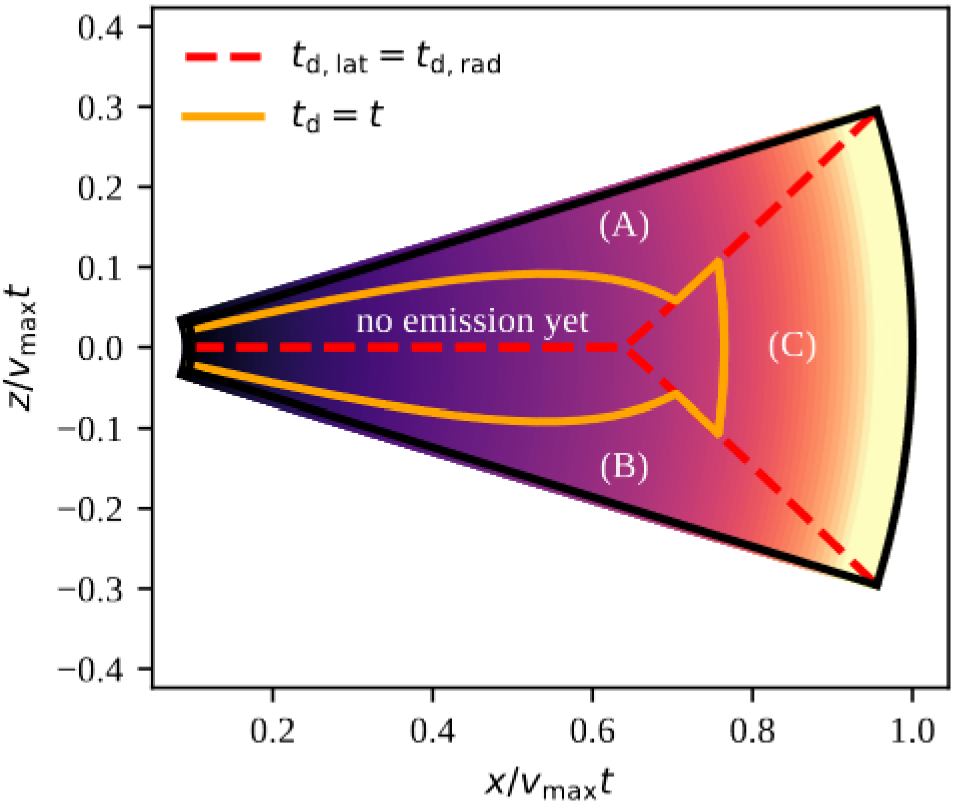

Figure 46: In this image we see three regions delimited by the red-dashed line, extended in the latitudinal ($x/v_{MAX}t$) and the longitudinal direction ($z/v_{MAX}t$). Regions A and B are the ones where we have latitudinal emission, above and below the equatorial plane respectively. The region C is the one where we have radial emission. The red-dashed line, which distinguishes the three regions, is based on the shortest time of emission which determines the kind of emission (longitudinal or radial). If the shortest time is the radial one, we have radial emission or else, if the shortest time is the longitudinal one, we have longitudinal emission. The color from purple to light yellow is related to the ejecta density from high to low. The orange line distinguishes the emission zone from that where there is no emission of the ejecta to the surface. [68].

4.4.1 What are the differences between the ejected components of the GW170817 event and those of a BHNS system?

The main difference between the two systems is the lack of neutrino-flux in the case of BHNS merger. While in the case of NSNS or a system like the GW170817, probably a QSHS system, there is a flux of neutrinos which contrasts the r-process and which reduces the opacity of the dynamical ejecta, in the BHNS system there is not this flux and the dynamical ejecta are completely opaque ($k = 15\ cm^2\ g^{-1}$).

a) The relativistic jet launch

A part of the disrupted material of the NS forms a disc around the BH. The accretion disc, which is produced, induces the launch of a relativistic jet through the Blandford-Znajek mechanism [68]. The luminosity produced by this mechanism can be expressed through a proportionality law which is:

(4.4.15) $L_{BZ} \propto \frac{G^2 M_{BH}^2 B^2 \Omega_H^2 f(\Omega_H)}{c^3}$

Where B is magnetic field on the outer horizon, Ω_H is the dimensionless angular velocity at this horizon:

(4.4.16) $\Omega_H = \frac{\chi_{BH}}{2\left[1+\left(1-\chi_{BH}^2\right)^{1/2}\right]}$

with χ_{BH} spin parameter of the BH.

(4.4.17) $f(\Omega_H) = 1+1.38\ \Omega_H{}^2 - 9.2\ \Omega_H{}^4$

is the correction factor for high-spin values.

We can also obtain a proportionality law between the magnetic field and the accretion mass of the disc, in the assumption of the presence of the Kelvin-Helmholtz instability. This law is:

(4.4.18) $B^2 \propto c^5 \dot{M}\ M_{BH}{}^{-2} / G^3$

where $\dot{M}$ is the accretion rate of mass on the remnant of the BH.

The jet produced by the accretion disc does not interact with the ejecta because the jet is launched orthogonal respect to the disc and the dynamical ejecta are concentrated in an angular space which is: $-22° < \theta_{DYN} < 22°$,where $\theta_{DYN} = 0$ on the equatorial plane [68]. The presence of the dynamical ejecta in the polar region is hence negligible. This is another difference between the NSNS and the BHNS system. In the NSNS system, or in a system like the GW170817, we surely have dynamical component of the ejection in the polar region (component which emits its spectrum as Blue kilonova for the presence of the wind component made of neutrinos). The ejection in the polar region is possible if we have a crust. This obviously is not present if the companion of the disrupted NS is a BH. The jet of a BHNS system is for this reason "cleaner" than that of the NSNS system.

b) The kilonova signal

In order to study the kilonova signal, the tidal deformability of the NS and its mass are crucial. Keeping the mass of NS constant, higher is the Λ_{NS} brighter is the signal, because higher is the amount of the ejected mass. If instead the tidal deformability is kept constant, higher is the mass brighter is the kilonova signal. In general, stiffer is the EOS brighter is the Kilonova signal, but there are exceptions. In fact, if we see the following figure 47, we see that if $M_{NS} = 1.6\ M_o$ or $1.8\ M_o$ the signal is not always dimmer than that with $M_{NS} = 2\ M_o$.

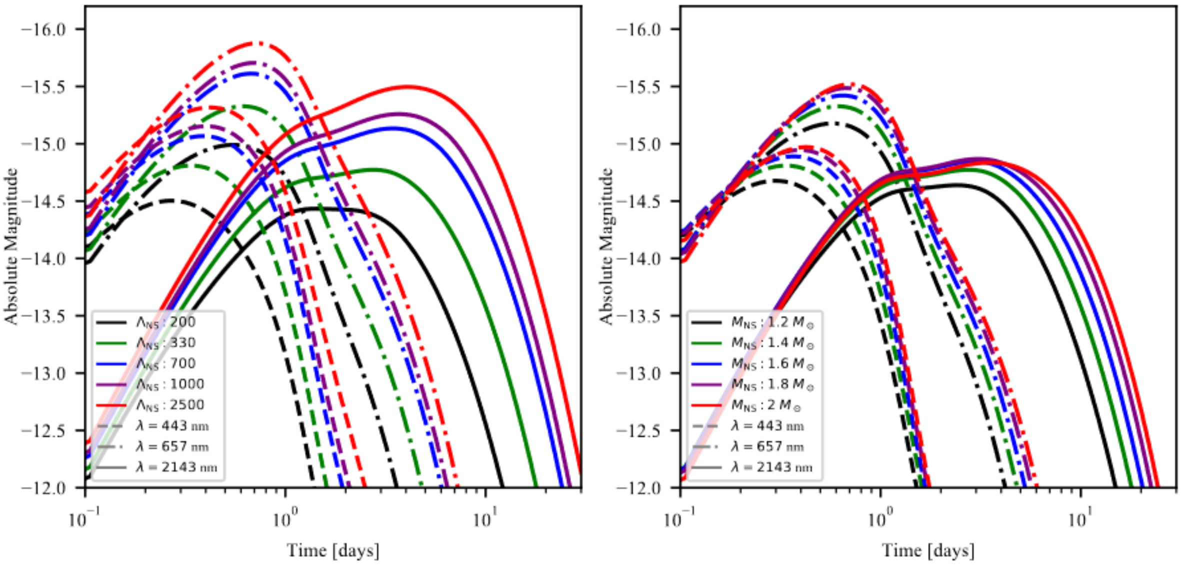

Figure 47: In the left panel we have the relation between the absolute magnitude of the kilonova signal and time, keeping the NS mass constant M_{NS} =1.4 M_o, the BH mass constant M_{BH} =3 M_o and the spin parameter constant χ_{BH} =0.5, and by changing the tidal deformability factor. In the right panel the situation is the same with keeping the tidal deformability factor constant Λ_{NS} =330, the BH mass and the BH spin parameter as before and by changing the NS mass. [68]

c) The GRB afterglow

After the prompt signal related to the jet, the jet spreads in the interstellar medium and starts its deceleration which produces a strong forward shock [68]. Near the shock there is electrons acceleration, and this produces a synchrotron radiation which is our GRB afterglow. If we wanted to study the dynamics of this signal, we should consider two angles θ, the latitudinal angle, and φ, the azimuthal one. Then, we should consider the mass of interstellar medium swept by the jet per unit of solid angle Ω:

$$(4.4.19)\ \mu(R) = \frac{n m_p R^3}{3}$$

where m_p is the proton mass and n is the number of protons (this is an idealization, but we are considering the interstellar medium as made uniquely by hydrogen) and R is the distance from the jet's launch site.

Now we could write down the Lorentz factor of the material as

$$(4.4.20)\ \Gamma(R,\theta) = \frac{\mu_0}{2\mu}\left\{\left[1+\left(\frac{4\mu}{\mu_0^2}\right)\left(\mu+\mu_0+\frac{dE}{d\Omega}c^{-2}\right)\right]^{1/2}-1\right\}$$

where

(4.4.21) $\mu_0(\theta) = \frac{\frac{dE}{d\Omega(\theta)}}{\Gamma(0,\theta)c^2}$

with dE/dΩ is the derivative of the energy respect to the solid angle and Γ (0, θ) is the Lorentz factor at the jet's launch site. We have a forward shock which is faster than the shocked material and we can calculate its Lorentz factor.

(4.4.22) $\Gamma_S = [\gamma_a(\Gamma - 1) + 1]\left\{\frac{\Gamma+1}{\gamma_a(2-\gamma_a)(\Gamma-1)+2}\right\}^{1/2}$

where γ_a is the post-shock adiabatic index.

This index is a very important parameter to evaluate the thickness of the emitting region in the assumption of uniform density distribution of material and by imposing the conservation of the electron number. This thickness can be expressed as

(4.4.23) $\Delta R = \frac{R(\gamma_a-1)}{3(\gamma_a\Gamma+1)\Gamma}$

while the electron number density in the shock region can be expressed as

(4.4.24) $n_s = n\frac{\gamma_a\Gamma+1}{\gamma_a-1}$

Now we have all the ingredients to calculate the arrival time of the signal, its brightness and its flux.

The arrival time of the signal, in the assumption of small thickness of the emitting region (ΔR<<R) [68], is:

(4.4.25) $t = (1+z)\int_0^R \frac{1-\beta_s cos\alpha}{\beta_s c}\,dR$

where z is the redshift, $\beta_S = (1-\Gamma_S^{-2})^{1/2}$ is the shock velocity in units c, α is the angle between the line of sight of the observer and the versor which is perpendicular to the surface element:

(4.4.26) $\cos\alpha = \cos\theta \cos\theta_V + \sin\theta \sin\varphi \sin\theta_V$

where θ_V is the angle between the observer's line of sight and the axis of the jet.

The shock brightness can be computed as

(4.4.27) $I_\nu = \Delta R' j_\nu \delta^3$

where $\Delta R' = \Gamma(R, \theta)\,\Delta R$, j_ν is the synchrotron emissivity and δ is the Doppler factor of the shocked material, which is expressed as

(4.4.28) $\delta = \frac{1}{\Gamma(R,\theta)[1-\beta(R,\theta)cos\alpha]}$

The shock brightness could be expressed as

(4.4.29) $I_\nu = \Delta R' j_{\nu\,MAX} S(\nu')\,\delta^3$

where $S(\nu')$ is the normalized spectrum shape with $\nu' = \nu/\delta$

and $j_{\nu\,MAX}$ is the biggest synchrotron emissivity which can be expressed as

(4.4.30) $j_{\nu\,MAX} \approx 0.66\left[\frac{q_e^3}{m_e^2 c^4}\right][(p-2)(3p-1)]\frac{B\varepsilon_e e}{\gamma_m}$

where $q_e = 1.6\text{x}10^{-19}$ is the electric charge of electron, $m_e = 9{,}1\text{x}10^{-31}$ Kg is the electron mass, B is the magnetic field which is amplified by instability in the small scales before the shock. ϵ_e is the fraction of the total energy due to the electrons, while e is the total energy. p (which is taken bigger than 2) is a parameter related to the expression of the electron number density in the shock region. This expression is $dn_S/d\gamma \propto \gamma^{-p}$ [68]:

where γ is the Lorentz factor of the electrons. The minimum value γ_m of this factor can be expressed as

(4.4.31) $\gamma_m = \max\left[1, \frac{p-2}{p-1}\frac{m_p}{m_e}(\Gamma-1)\right]$

We can consider γ_m the only Lorentz factor for the electrons, because the distribution of their number density is decreasing and almost all the electrons have a Lorentz factor $\gamma = \gamma_m$.

Now we can write the flux of the signal which is:

(4.4.32) $F(\nu, t) = 2\frac{1+z}{d_L^2}\int_0^1 dcos\theta \int_{-\pi/2}^{+\pi/2} d\varphi\, I_\nu(\nu(1+z), R)\, R^2$

where the factor 2 is due to the fact that there are actually 2 jets which go towards opposite direction. The treatment is identical if we exclude that we have to add π to θ_V. Beyond that, in this integral is calculated only for half of the surface. For the other half, the treatment is analogous. Another fact to underline is the use in this integral of the luminosity distance d_L which is not the physical distance in an expanding universe, because of the z factor related to the redshift.

We can see now, as done for the kilonova signal before, the relation between signal and time by fixing the NS mass in one case and the tidal deformability in the other one, by keeping the BH mass and spin fixed as previously (figure 48). The new is the fixed angle of observation which, in this case, is $\theta_v = 30$ °.

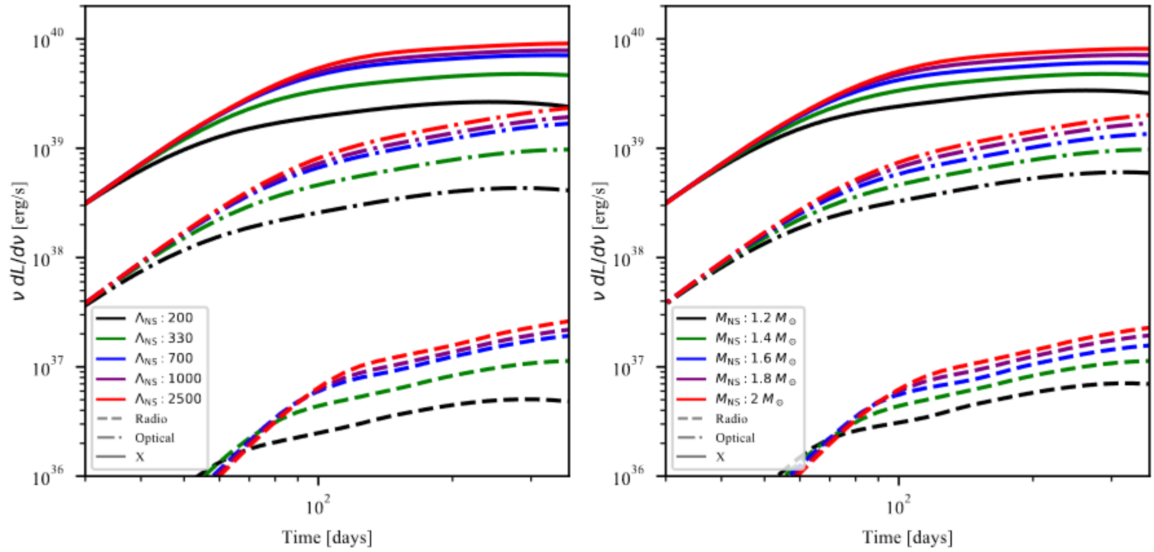

Figure 48: In this plot we see the relation between vdL/dv (the derivative of the luminosity respect to the signal frequency multiplied by the frequency itself) and time. [68]

4.5 The GRB200522A and GRB160821B signals

Beyond the GRB signal from the S1090426c BHNS system, there is another interesting one to treat, which is very new (it was detected in August 2020): the GRB200522A studied by Fong, which is the results of the merger of two Neutron Stars [74]. This signal is interesting, because it has an unusual broad-band counterpart which cannot be easily explained by a single emission component. We can interpret the radio, NIR (Near InfraRed) and X-observations of the GRB200522A as related to Synchrotron emission from a forward shock produced by the interaction between the GRB jet and the environment around it. The synchrotron spectrum, which is possible for the magnetic field produced by a Magnetar, the result of the merger of the two Neutron Stars, for the GRB200522A is characterized by three frequencies: the synchrotron self-absorption frequency, the characteristic synchrotron frequency, and the cooling frequency. The NIR counterpart observed 2.3 days after the emission has a luminosity of (1.3-1.7 x 10^{42} erg s^{-1}) [74]. It is lower than on-axis short GRB afterglow detections, but it is 8-17 times more luminous than the kilonova signal from the GW170817. The problem about the NIR arises from the fact that, even in the most optimistic case, we obtain a NIR frequency flux which is 10 times fainter the observed one: $F_v \approx 0.049$ µJy (microjoule per year) is the theoretical value and $F_v \approx 0.55$ µJy is what we observed. Hence, we have an excess of NIR flux that we must explain. It can be explained if we consider the effect of a reverse shock. The higher luminosity compared to that of any other known kilonova signal. If we just considered the r-process radioactive decay, this would imply a higher mass ejection, or it would be heated at higher heating rate (erg s^{-1} g^{-1}) or both. The r-process which is responsible of the kilonova signal can be split into two types of process: the heavy r-process and the light r-process. The former, which produces heavy elements, such as lanthanides and actinides, generates a kilonova signal in the band of NIR, a redder signal, while the latter, which occurs when there are less neutrons, does not produce heavy elements and the related kilonova signal is bluer. The GRB200522A signal is bluer than the GW170817 kilonova signal. The brighter kilonova signal could be explain by the formation of an indefinitely stable to BH- collapse magnetar obtained through the BNS merger. This magnetar would be characterized by a very strong magnetic field and a very high spin momentum. This situation provides energy that could not be produced in a prompt collapse to a BH. In fact, this energy, which feeds an expanding nebula, is thermalized at optical and NIR wavelengths. Nonetheless, a BNS system which ends to a stable magnetar is a very rare event. However, if this supposition is true, a late-time synchrotron emission should be observable with a peak at 1-10 years after the emission. Future radio observations could offer a concrete possibility of testing the correctness of our hypothesis of kilonova signals from a magnetar.

Another important event of kilonova, from which we can learn something new, is that related to GRB160821B studied by Troja, detected in 2016 [75]. Thanks to its low redshift and a rich multi-wave dataset, it is an important testbed for kilonova study. An interesting fact is the color evolution of the GRB160821B, which is atypical for a GRB afterglow, but it is compatible with a kilonova peak in the optical roughly one day after the burst. Then, there was a shift to longer wavelengths. The IR emission started fading a few days after the burst like in the AT2017gfo case. Beyond this, we have an X-ray afterglow which has a bright and rapidly fading light curve. The X-ray flux decreases from 2×10^{-10} erg cm^{-2} s^{-1} at t=250 s after the burst to 2×10^{-12} erg cm^{-2} s^{-1} at t=400 s after the burst. To understand better this, we can show a plot where we see a comparison between GRB160821B and GRB090515. (For the AT2017gfo we do not see a relevant presence of an X-ray component). This X-ray afterglow shows evidence of long-lasted engine activity. The X-ray emission could be interpreted as due to the formation of a proto-magnetar. The sudden decay of the X-ray emission could be associated to the collapse to Black Hole. We observed a Plateau of $L_X \approx 5\times10^{47}$ erg s^{-1} which lasted for roughly 200 seconds, where L_X represents the X-ray luminosity. This fact could be useful for us to study magnetar properties.

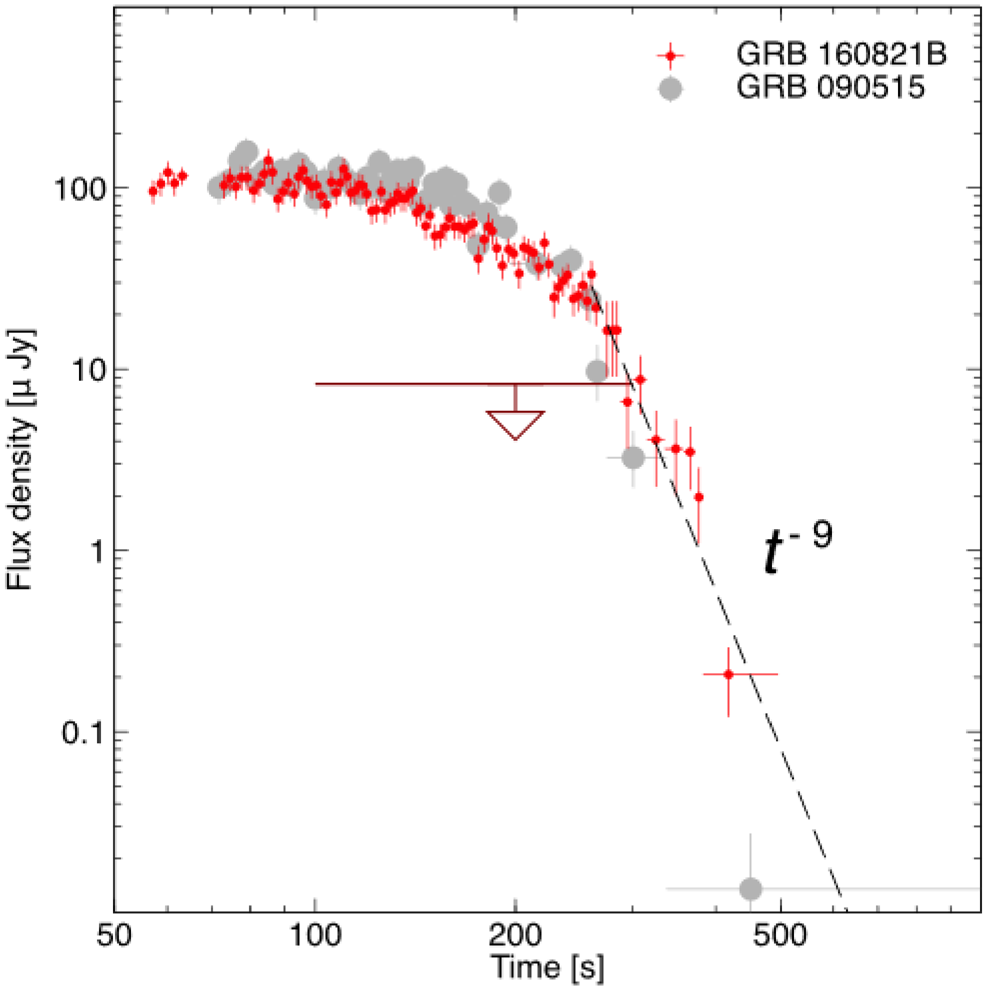

Figure 49: In this figure we see how the density of the X-ray flux decays with time. Red points indicate the GRB160821B while the grey ones are referred to the GRB090515. After roughly 400 seconds, we see a decay function which is proportional to t^{-9}. [75]

We see that the color evolution for GRB160821B is similar to that of the AT2017gfo, but it is less luminous of a factor between 2 and 5. The observed NIR luminosity of roughly $2x10^{39}$ erg s^{-1} and its timescale, which is roughly three days for the peak, imply a low ejecta mass $M_{ej} < 0.006\ M_o$ and high velocity v_{ej}>0.05 c with an opacity k≈10 g cm^{-3}. The ejecta mass is quite lower than for other GRB kilonovae. We also have an early blue excess, even if with big uncertainties. The timescale and the luminosity for this blue component are compatible with the AT2017gfo. The blue color and its onset would require a mass for the ejecta of lanthanide-poor material of roughly 0.01 M_o.

CONCLUSIONS

We conclude by considering a summary of what we have learned from the study of the topics of this thesis.

a) We understand how to link the gravitational waves signal to the probability of having a particular type of merger among Black Hole-Black Hole (BBH), Binary Neutron Stars (BNS) and Neutron Star-Black Hole (BHNS), by considering the GW frequency, the Chirp Mass and the Post-Newtonian expansion.

b) We investigated the most likely environment for having Black Hole-Neutron Star mergers by studying Hoang's work on the topic. The Galactic Nuclei are the locations where there is the highest probability of BHNS mergers through single- single GWs capture, where we have only one Neutron Star which interacts with only one Black Hole.

c) We consider the tidal deformability of Neutron Stars through the work made by Hinderer for Binary Neutron Star systems. Hinderer used the spherical harmonics with l=2 and m=0 modes in the metric tensor of the spacetime deformed by BNS in interaction. This is a good method even if it is valid just in the early phase of the interaction. Then, we consider the tidal deformability of the neutron stars in BHNS by taking in consideration the work made by Lackey who studied the tidal deformability in this situation by using the Effective-One-Body (EOB) model introduced by Buonanno and Damour.

d) We considered the possibility that the very high pressure and density inside the core of the star is able to produce a new kind of matter made of free quarks. We also study the Witten's hypothesis of the existence of pure Quark Stars with free quark matter produced at zero pressure. Even if this possibility is theoretically valid, to be observed a time much longer than the age of the universe would be required. Then, we made a comparison between Neutron and Quark Stars and we saw that Neutron Stars have a radius that drops if the mass increases, while for Quark Stars we have the opposite.

e) We studied the Electromagnetic emission of the GW170817 event, considering the GRB (Gamma Ray Burst) signal, whose origin is still unclear, and the Red and the Blue kilonova signals. The kilonova signals are the result of the process of the formation of heavy nuclei (heavier than iron), with the Red part related to heavier nuclei and the Blue part related to lighter nuclei. The Blue emission occurs around the axis of the merger and there the nuclei are lighter, because of the neutrino flux. Then, we compared this result with the case of a BHNS merger, and we found out that no Blue signals for BHNS systems are expected.

f) We consider the possibility of having a Quark Star as result of a Binary Neutron Star merger by considering the amplitude and the duration of the kilonova signals and the study made by Bauswein about the relation between mass of the merger and its spin, considering also the GW170817 case. The result is that, even though it is not the only possibility, the existence of Quark Star for this event cannot be excluded.

   This is of course a field of research that is still developing, and future discoveries about Binary Compact Object mergers will be crucial to check the validity of our hypothesis about the existence of Quark Stars and about the origin of the GRB signals for Binary Compact Object mergers. The improvement of the GW detection systems, like LISA, ET and DECIGO projects will give us some new information about this topic.

APPENDIX

We have already encountered the kilonova signal and how it is related to the nuclear r-process which determines its spectrum. Now, we are going to study it in detailed way.

The r-process

Studying the abundance of elements is very important both in astrophysics and cosmology in order to discover the composition of matter of the early universe. About that, it is useful to see this picture about the rate of distribution of the elements relative to the silicon respect to the mass number.

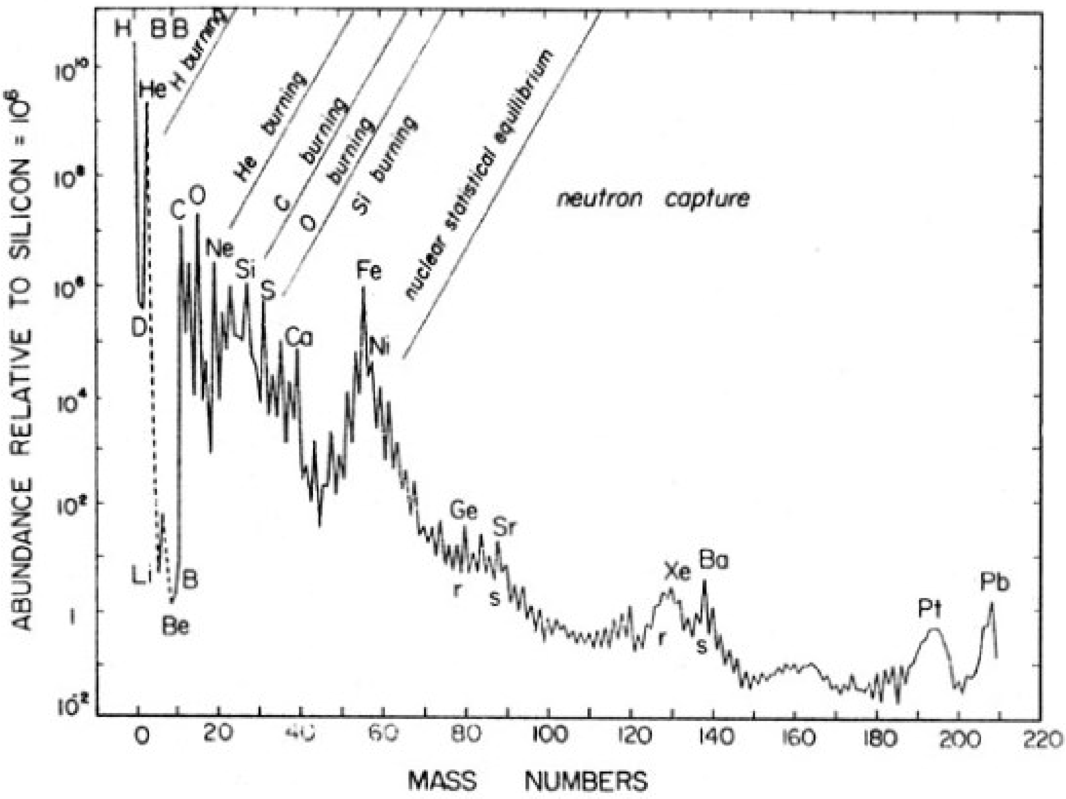

Figure 50: In this image we see the abundances of the elements in function of their mass numbers. The letter r and s states for rapid and slow process. [76]

From the figure 50, we can infer that the Hydrogen and the Helium are the most abundant elements in our universe. In fact, they are the primordial elements in our universe, the others till the iron are produced by nuclear reactions inside the stars. The elements which are heavier than iron cannot be produced by nuclear reactions because the iron is the most stable element and a nuclear fusion process to produce these elements would require energy instead of releasing it. In order to produce these elements, the r-process is required. This process is based on the β-decay and neutron capture. Actually, there are two kinds of processes which combine β-decay and neutron capture: s-process and r-process. Their distinction is based on the speed of the neutron capture respect to the β-decay. The neutron capture process transforms a (Z, A)- nucleus into a heavier isotope (Z, A + 1). Then, if the nucleus is stable, the process goes on and we obtain (Z, A + 2). Otherwise, the β-decay occurs, and one neutron of the nucleus becomes proton before it manages to capture another neutron. If average time of β-decay is smaller than that of neutron capture we have s-process and we do not have heavy nuclei. In the opposite case for the fact that, via neutron capture, heavy rich in neutrons nuclei are formed before the β-decay which, when it happens, by turning neutrons into protons, creates elements heavier than iron.

Bibliography

[1] M.P.Hobson, General relativity: an introduction for physicists., Cambridge University Press, 2006, pp. 471-472.

[2] Abbott.B, «Prospects for observing and localizing gravitational-wave transients with Advanced LIGO, Advanced Virgo and KAGRA,» *Living Review in Relativity.101007/s41114-020-00026-9,* vol. 23, n. 1, pp. 1-5, 2020.

[3] P. J. Sutton, «A Rule of Thumb for the Detectability of Gravitational-Wave Bursts. arXiv:1304.0210,» *arXiv e-prints,* 2013.

[4] P. Collaboration, «Planck 2015 results. XIII. Cosmological parameters.arXiv:1502.01589,» *Astronomy and Astrophysics,* vol. 594, 2016.

[5] T. E. T. p. website, 2008.

[6] S.Hild, «Pushing towards the ET sensitivity using "conventional" technology.arxiv:0810.0604,» *arXiv e-prints,* pp. 1-4, 2008 .

[7] M. Jay, «The Gravitational Wave International Committee Roadmap: The future of gravitational wave astronomy,» *arXiv:1111.5825,* pp. 49-50 ,77-81, 2011.

[8] F. C., «LIGO/Virgo S190910d: Upper limits from Fermi-GBM Observations,» *GRB Coordinates Network.arXiv:https://ui.adsabs.harvard.edu/abs/2019GCN.25699....1F,* vol. 25699, 2019.

[9] R. H. a. IceCube, «LIGO/Virgo S190910d: Upper limits from IceCube neutrino searches,» *GCN Circular,* 19/09/10.

[10] H. Collaboration, «LIGO/Virgo S190923y: No counterpart candidates in HAWC observations,» *GRB Coordinates Network:https://ui.adsabs.harvard.edu/abs/2019GCN.25813....1H,* vol. 25813, 2019.

[11] R. H. a. IceCube, «LIGO/Virgo S190923y: Upper limits from IceCube neutrino searches,» *GCN CIRCULAR,* 19/09/23.

[12] {. S. C. a. {. Collaboration}, «LIGO/Virgo S190930t: Identification of a GW compact binary merger candidate,» *GRB Coordinates Network.https://ui.adsabs.harvard.edu/abs/2019GCN.25876....1L,* vol. 25876, 2019.

[13] R. H. a. IceCube, «LIGO/Virgo S190930t: Upper limits from IceCube neutrino searches,» *GCN CIRCULAR,* 19/09/30.

[14] F. C., «LIGO/Virgo S191205ah: Upper limits from Fermi-GBM Observations,» *GRB Coordinates Network.https://ui.adsabs.harvard.edu/abs/2019GCN.26359....1F,* vol. 26359, 2019.

[15] B. M. Hoang, «Neutron Star-Black Hole Mergers from Gravitational-wave Captures,» *The Astrophysical Journal. arXiv:2007.08531,* vol. 903, n. 1, 2020.

[16] S. I., The Lidov-Kozai effect – applications in exoplanet research and dynamical astronomy, Astrophysics and Space Science Library, 2017.

[17] J.Lattimer, «The Properties of a Black Hole-Neutron Star Merger Candidate,» *arXiv e-prints. arXiv:1908.03622,* pp. 1-2, 2019.

[18] V.Tiwari, «Reconstruction of Chirp Mass in the searches for gravitational wave transients,» *Classical and Quantum gravity.arXiv:1510.02426,* vol. 33, n. 1, p. 1, 2018.

[19] C.Cutler, «Gravitational waves from merging compact binaries: How accurately can one extract the binaries parameters from the

inspiral waveforms?,» *Physical review D.arXiv:gr-qc/9402014,* vol. 49, n. 6, p. 1, 1994.

[20] C.Cutler, «The last three minutes: Issues in gravitational-wave measurements of coalescing compact binaries,» *Physical Review Letters.arXiv:astro-ph/9208005,* vol. 70, n. 20, p. 1, 1993.

[21] T.Hinderer, «Tidal deformability of neutron stars with realistic equation of State and their gravitational wave signature in binary inspiral,» *Physical Review D.arXiv:0911.3535,* vol. 81, n. 12, 2010.

[22] P.Kumar, «Measuring neutron star tidal deformability with Advanced LIGO: a Bayesian analysisof neutron star - black hole binary observations,» *Physical Review D.044039,* vol. 95, n. 4, pp. 1-7, 2017.

[23] A.Tarrachini, «Prototype effective-one-body model for nonprecessing spinning inspiral-merger-ringdown waveforms,» *Physical Review D.arXiv:1202.0790,* vol. 86, n. 2, pp. 1-3, 2012.

[24] M.Purrer, «Frequency domain reduced order model of aligned-spin effective-one-body waveforms with generic mass ratios and spins,» *Physica Review D.arXiv:1512.02248,* vol. 93, n. 6, pp. 1-2, 2016.

[25] V. Goncalves, «An introduction to strange stars,» *arXiv e-prints.arxiv:2006.02976,* 2020.

[26] N. Chamel, «Neutron drip transition in accreting and non accreting neutron stars crusts.arXiv:1504.04537,» *Physical Review C,* vol. 91, n. 5, p. 2, 2015.

[27] N. K. Glendenning, Compact Stars Nuclear Physics,Particle Physics and General Relativity, Astronomy and Astrophysics Library, 2000, pp. 342-345.

[28] P. Haensel, Neutron Stars 1: Equation of State and Structure, Astrophysics and Space Science Library, 2007, pp. 407-435.

[29] S.Postnikov, «Tidal Love numbers of neutron and self-bound quark stars,» *Physical Review D.arXiv:1004.5098,* vol. 82, n. 2, pp. 7-15, 2010.

[30] A.Bauswein, «Semi-analytic derivation of the threshold mass for prompt collapse in binary neutron-star mergers,» *Monthly Notices of the Royal Astronomical Society.arXiv:1702.02567,* vol. 471, n. 4, pp. 4-5, 2017.

[31] A.Bauswein, «Equation of state constraints from the threshold binary mass for prompt collapse of neutron star merger,» *Physical Review Letters.arXiv:2004.00846,* vol. 125, n. 14, 2020.

[32] A. Drago, «The Merger of Two Compact Stars: A Tool for Dense Matter Nuclear Physics,» *www.mdpi.com/journal/universe. doi:10.3390/universe4030050,* 2018.

[33] R. L., « A novel paradigm for short gamma-ray bursts with extended X-ray emission.arxiv:1410.8560,» *The Astrophysical Journal ,* vol. 802, n. 2, 2015.

[34] N.Lyons, «Can X-Ray Emission Powered by a Spinning-Down Magnetar Explain Some GRB Light Curve Features?,» *Monthly Notices of the Royal Astronomical Society.arxiv:0908.3798,* vol. 402, n. 2, 2010.

[35] B.D.Metzger, «Quark deconfinement and the duration of short gamma-ray bursts,» *Physical Review D.arxiv:1510.05581,* vol. 93 , n. 10, 2016.

[36] G. B., «The Missing Link: Merging Neutron Stars Naturally Produce Jet-like Structures and Can Power Short Gamma-ray Bursts,» *The Astrophysical Journal Letters.arxiv:1101.4298,* vol. 732, n. 1, 2011.

[37] R.Ciolfi, «Short gamma-ray bursts from binary neutron star mergers: the time-reversal scenario,» *eprint arxiv:1505.01420,* 2015.

[38] A. Drago, «Merger of compact stars in the two-families scenario,» *The Astrophysical Journal.arXiv:1904.01545,* vol. 881, n. 2, pp. 5-7, 2019.

[39] B.P.Abbott, «GW170817:Observation of Gravitational Waves from a Binary Neutron Star Inspiral,» *Physical Review Letters.arXiv:1710.05832,* vol. 119, n. 16, p. 2, 2017.

[40] C.Palenzuela, «Effects of the microphysical Equation of State in the mergers of magnetized Neutron Stars With Neutrino Cooling,» *Physical Review D.arxiv:1505.01607,* vol. 92, n. 4, 2015.

[41] S. Y., «Dynamical mass ejection from binary neutron star mergers:Radiation-hydrodynamics study in general relativity,» *Physical Review D.arxiv:1502.06660,* vol. 91, n. 6, 2015.

[42] G. S., « Impact of weak interactions of free nucleons on the r-process in dynamical ejecta from neutron-star mergers,» *Monthly Notices of the Royal Society.arxiv:1504.04377,* vol. 452, n. 4, 2015.

[43] A.Bauswein, « Systematics of dynamical mass ejection, nucleosynthesis, and radioactively powered electromagnetic signals from neutron-star merger,» *The Astrophysical Journal.arxiv:1302.6530,* vol. 773, n. 1, 2013.

[44] M.Tanaka, « Properties of Kilonovae from Dynamical and Post-Merger Ejecta of Neutron Star Mergers,» *The Astrophysical Journal.arxiv:1708.09101,* vol. 852, n. 2, 2018.

[45] R. S., «Neutrino-driven winds from neutron star merger remnants,» *Monthly Notices of the Royal Astronomical Society.arxiv:1405.6730,* vol. 443, n. 4, 2014.

[46] K. D., «Kilonova light curves from the disc wind outflows of compact object mergers,» *Monthly Notices of the Royal Astronomical Society.arxiv:1411.3726,* 2015.

[47] A.Bauswein, «SYSTEMATICS OF DYNAMICAL MASS EJECTION, NUCLEOSYNTHESIS, AND RADIOACTIVELY POWERED ELECTROMAGNETIC SIGNALS FROM NEUTRON-STAR MERGERS,» *The Astrophysical Journal. doi:10.1088/0004-637X/773/1/78,* vol. 773, n. 1, p. 2, 2013.

[48] C.Freiburghaus, «r-PROCESS IN NEUTRON STAR MERGERS,» *The Astrophysical Journal,* vol. 525, n. 2, 1999.

[49] B.D.Metzger, «Electromagnetic counterparts of compact object mergers powered by the radioactive decay of r-process

nuclei.https://doi.org/10.1111/j.1365-2966.2010.16864.x,» *The Monthly Notices of the Astronomical Society,* vol. 406, n. 4, 2010.

[50] O.Korobkin, «On the astrophysical robustness of the neutron star merger r-process.doi:10.1111/j.1365-2966.2012.21859.x,» *Monthly Notices of the Royal Astronomical Society,* 2012.

[51] G. S., «Further explorations of Skyrme-Hartree-Fock-Bogoliubov mass formulas. VII. Simultaneous fits to masses and fission barriers,» *Physical Review C.10.1103/PhysRevC.75.064312,* vol. 75, n. 6, 2007.

[52] A.Arcones, «Dynamical r-process studies within the neutrino-driven wind scenario and its sensitivity to the nuclear physics input,» *Physical Review C.arXiv:1008.3890,* vol. 83, n. 4, 2011.

[53] H.Janka, «Dynamics of shock propagation and nucleosynthesis conditions in O-Ne-Mg core supernovae,» *Astronomy and Astrophysics.https://doi.org/10.1051/0004-6361:20079334,* vol. 485, n. 1, 2008.

[54] A. Arcones, «Nucleosynthesis-relevant conditions in neutrino-driven supernova outflows. II. The reverse shock in two-dimensional simulations.arXiv:1008.0882,» *Astronomy and Astrophysics,* vol. 526, 2011.

[55] R. Hoffman, «Nucleosynthesis in O-Ne-Mg Supernovae.arXiv:0712.4257,» *The Astrophysical Journal Letters,* vol. 676, n. 2, 2008.

[56] L.Hudepohl, «Neutrino Signal of Electron-Capture Supernovae from Core Collapse to Cooling.arXiv:0912.0260,» *Physical Review Letters,* vol. 104, n. 25, 2010.

[57] S.Wanajo, «Electron-capture Supernovae as The Origin of Elements Beyond Iron.arXiv:1009.1000,» *The Astrophysical Journal Letters,* vol. 726, n. 2, 2011.

[58] T.Fischer, «Protoneutron star evolution and the neutrino-driven wind in general relativistic neutrino radiation hydrodynamics simulations,» *Astronomy and Astrophysics.arXiv:0908.1871,* vol. 517, 2010.

[59] K.Hotokezaka, « Mass ejection from neutron star mergers: different components and expected radio signals,» *Monthly Notices of the Royal Astronomical Society.arxiv:1501.01986,* vol. 450, n. 2, 2015.

[60] K.Kiuchi, «Mass ejection from the merger of binary neutron stars,» *Physical Review D.arxiv:1212.0905,* vol. 87, n. 2, 2013.

[61] A.Perego, «AT2017gfo: an anisotropic and three-component kilonova counterpart of GW170817,» *The Astrophysical Journal Letters.arXiv:1711.03982,* 2017.

[62] S.Fujibayashi, «Mass ejection from the remnant of a binary neutron star merger: viscous-radiation hydrodynamics study,» *The Astrophysical Journal.arXiv:1711.02093,* vol. 860, n. 1, pp. 1-13, 2018.

[63] A.Bauswein, « Exploring properties of high-density matter through remnants of neutron-star mergers,» *European Physical Journal A. arXiv:1508.05493,* vol. 52, 2015.

[64] D'Avanzo, «The evolution of the X-ray afterglow emission of GW 170817 / GRB 170817A in XMM-Newton observations.Arxiv::1801.06164,» *Astronomy and Astrophysics,* vol. 613, p. 2, 2018.

[65] R. Margutti, «THE BINARY NEUTRON STAR EVENT LIGO/VIRGO GW170817 A HUNDRED AND SIXTY DAYS AFTER MERGER:SYNCHROTRON EMISSION ACROSS THE ELECTROMAGNETIC SPECTRUM,» *The Astrophysical Journal.arXiv:1710.05938,* vol. 856, n. 1, 2018.

[66] O.Gottlieb, «A cocoon shock breakout as the origin of the γ-ray emission in GW170817,» *Monthly Notices of the Royal Astronomical Society.arxiv:1710.05896,* vol. 479, n. 1, 2018.

[67] J. Lattimer, «The properties of a Black Hole-Neutron Star merger candidate,» *arXiv e-prints.arXiv:1908.03622,* pp. 1-4, 2019.

[68] C. Barbieri, «Electromagnetic counterparts of black hole–neutron star mergers: dependence on the neutron star properties,» *The European Physical Journal.arXiv:1908.08822,* vol. 56, n. 1, 2020.

[69] M.P.Hobson, General relativity: an introduction for physicists, Cambridge University Press, 2006, p. 337.

[70] O.Just, «Comprehensive nucleosynthesis analysis for ejecta of compact binary mergers,» *Monthly Notices of the Royal Astronomical Society.arxiv:1406.2687,* vol. 448, n. 1, 2015.

[71] R.Fernandez, «Dynamics, nucleosynthesis, and kilonova signature of black hole—neutron star merger ejecta,» *Classical and Quantum Gravity.arxiv:1612.04829,* vol. 34, n. 15, 2017.

[72] L.Dessart, «Neutrino Signatures and the Neutrino-Driven Wind in Binary Neutron Star Mergers,» *The Astrophysical Journal.arxiv:0806.4380,* vol. 690, n. 2, 2009.

[73] D.Radice, «Binary Neutron Star Mergers: Mass Ejection, Electromagnetic Counterparts, and Nucleosynthesis,» *The Astrophysical Journal.arxiv:1809.11161,* vol. 869, n. 2, 2018.

[74] W.Fong, «The Broadband Counterpart of the Short GRB 200522A at z = 0.5536: A Luminous Kilonova or a Collimated Outflow with a Reverse Shock?,» *The Astrophysical Journal.arXiv:2008.08593,* vol. 906, n. 2, 2020.

[75] E.Troja, «The afterglow and kilonova of the short GRB 160821B,» *Monthly Notices of the Royal Astronomical Society.arXiv:1905.01290,* vol. 489, n. 2, 2019.

[76] C.Rolfs, Cauldrons in the Cosmos, The university of Chicago Press, 1988, pp. 461-469.